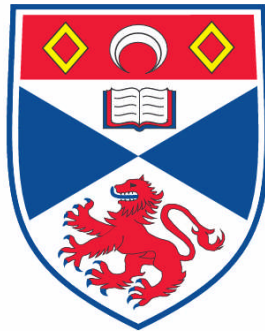


LONGITUDINAL OPTICAL BINDING

Nikolaus K. Metzger

**A Thesis Submitted for the Degree of PhD
at the
University of St. Andrews**



2008

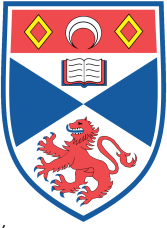
**Full metadata for this item is available in the St Andrews
Digital Research Repository
at:**

<https://research-repository.st-andrews.ac.uk/>

Please use this identifier to cite or link to this item:

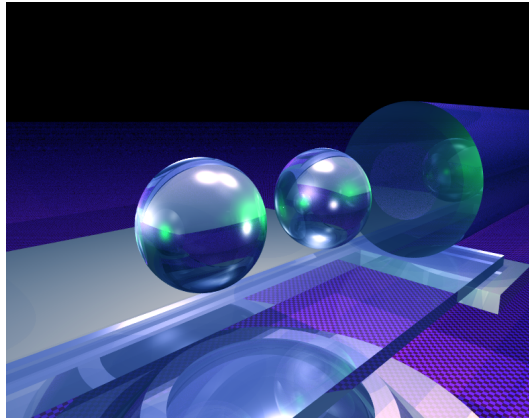
<http://hdl.handle.net/10023/519>

This item is protected by original copyright



UNIVERSITY OF ST ANDREWS
SCHOOL OF
PHYSICS & ASTRONOMY

LONGITUDINAL
OPTICAL BINDING



THESIS FOR THE DEGREE OF DOCTOR OF PHILOSOPHY

JULY 2004 - AUGUST 2007
NIKOLAUS K. METZGER

Declarations

I, Nikolaus Metzger, hereby certify that this thesis, which is approximately 30,000 words in length, has been written by me, that it is the record of work carried out by me and that it has not been submitted in any previous application for a higher degree.

date signature of candidate

I was admitted as a research student in July 2004 and as a candidate the degree of Doctor of Philosophy in July 2005; the higher study for which this is a record was carried out in the University of St Andrews between 2004 and 2007.

date signature of candidate

I hereby certify that the candidate has fulfilled the conditions of the Resolution and Regulations appropriate for the degree of Doctor of Philosophy in the University St Andrews and that the candidate is qualified to submit this thesis in application for that degree.

date signature of supervisor

In submitting this thesis to the University of St Andrews I understand that I am giving permission for it to be made available for use in accordance with the regulations of the University Library for the time being in force, subject to any copyright vested in the work not being affected thereby. I also understand that the title and abstract will be published, and that a copy of the work may be made and supplied to any bona fide library or research worker, that my thesis will be electronically accessible for personal or research use, and that the library has the right to migrate my thesis into new electronic forms as required to ensure continued access to the thesis. I have obtained any third-party copyright permissions that may be required in order to allow such access and migration.

date signature of candidate

Acknowledgements

Many helping hands brought my thesis to fruition, more than a big 'Thank you' goes out to...

Kishan for his excellent ideas and visions and endless support in making them happen.

Ewan for teaching me all that I know about beam propagation, the 24 hour online support service for the theory and his friendship. Furthermore his family who gave me always a warm welcome in Tucson.

Masud Mansuripur, for the fruitful discussions.

Michael for pitching in when mathematical help was needed most.

Erik Baigar, who ever since my thesis has been around to answer my numerous questions.

Gabe & Ryan, for their ongoing help with the particle tracking.

Sandra Murray for getting my money intime or sometimes ahead of time.

Phil my ultra mellow lab partner and fibre to fiber support.

Lynn and *Muriel* for the never ending help in extending my biology knowledge and the supply of CHO's.

Robert Maier from the Heriot-Watt University for sharing his knowledge and expertise in fiber optics as well as the equipment support.

Lorand Kelemen and *Pal Ormos* from the BRC in Hungary for the excellent collaboration within ATOM-3D.

Dave and *Tom* from the other side of the office wall cheers guys for all the bits and bobs ranging from electronics to website help.

David G for lots of interesting discussions.

Rob and *Steve Neal* for the fun with the PDMS and the cleanroom.

Valentin Blickle the Braunschweigebewegung connection in Stuttgart.

Steve all the late night discussions.

David Mcfarlane for the IR-camera.

David for opening up a wealth of 'bastell' opportunities through his ideas.

My correction readers *Maria*, *Valentin*, *Peter* and *Michael*. The support service from the machine shop and the secretarial staff. And last but not least my parents for their ongoing support.

Abstract

Longitudinal optical binding refers to the light induced self organisation of micro particles in one dimension. In this thesis I will present experimental and theoretical studies of the separation between two dielectric spheres in a counter-propagating (CP) geometry. I will explore the bistable nature of the bound sphere separation and its dependency on the refractive index mismatch between the spheres and the host medium, with an emphasis on the fibre separation.

The physical underpinning principle of longitudinal optical binding in the Mie regime is the refocusing effect of the light field from one sphere to its nearest neighbour. In a second set of experiments I developed means to visualise the field intensity distribution responsible for optical binding using two-photon fluorescence imaging from fluorescein added to the host medium. The experimental intensity distributions are compared to theoretical predictions and provide an *in situ* method to observe the binding process in real time.

This coupling via the refocused light fields between the spheres is in detailed investigated experimentally and theoretically, in particular I present data and analysis on the correlated behaviour of the micro spheres in the presence of noise. The measurement of the decay times of the correlation functions of the modes of the optically bound array provides a methodology for determining the optical restoring forces acting in optical binding.

Interestingly micro devices can be initiated by means of the light-matter interaction. Light induced forces and torques are exerted on such micro-objects that are then driven by the optical gradient or scattering force. I have experimentally investigate how the driving light interacts with and diffracts from the motor, utilising two-photon imaging. The micromotor rotation rate dependence on the light field parameters is explored and theoretically modelled. The results presented will show that the model can be used to optimise the system geometry and the micromotor.

Contents

1	Introduction	1
1.1	Optical forces	1
1.2	Rayleigh regime	2
1.3	Ray optics regime	4
1.4	Optically bound matter	5
1.5	Synopsis	9
2	Experiment	11
2.1	Optical fibre trap	12
2.2	Data analysis	15
2.3	Fibre trap design considerations	17
2.4	Investigated matter	20
2.4.1	Chinese Hamster Ovary cells	20
2.4.2	Microspheres	23
2.5	Conclusion	27
3	Optical binding of two dielectric spheres	29
3.1	Introduction	29
3.2	Linear array formation	32
3.3	Bistability in optical binding	33
3.4	Hysteresis	39
3.5	Experimental observation of hysteresis	41
3.6	Conclusion	45
4	Visualisation of the field distribution in optical binding	49
4.1	Theoretical model extension	49
4.2	Experimental setup	51
4.3	Dispersion	53

4.4	Two-photon excitation	54
4.5	Visualisation of the light redistribution in optical binding . . .	55
4.6	Refocusing by biological matter	58
4.7	Optically bound arrays	59
4.8	Optical bistability in bound matter	62
4.9	Conclusion	62
5	Restoring forces and correlation in optical binding	65
5.1	Integrated optical fibre trap	67
5.2	Theoretical model	70
5.2.1	Simulation and calculation of the restoring force on a single sphere	71
5.2.2	One sphere spring constant theoretical calculation . . .	72
5.2.3	Dynamic simulation of one sphere in a potential	73
5.2.4	Trap stiffness from Boltzmann statistics	75
5.2.5	Trap stiffness from the autocorrelation decay time . . .	77
5.2.6	Local viscosity probe	77
5.2.7	Temperature measurements and heating effects	79
5.2.8	Discussion	82
5.3	Investigation of an optically bound two sphere system via Brownian motion	85
5.3.1	Calculation of the restoring forces	85
5.3.2	Numerical calculation of the restoring forces	88
5.3.3	Equation of motion for a two sphere system	89
5.4	Experimental and theoretical results in the bistable regime . .	91
5.4.1	A) small sphere separation	93
5.4.2	B) large sphere separation	95
5.4.3	C) transition point	97
5.5	Discussion	98
5.6	Experimental and theoretical results in the linear regime . . .	98
5.7	Conclusion and discussion	99
6	Observation and simulation of an optically driven micromo- tor	103
6.1	Introduction	103
6.1.1	Actuating micromotors with light	105
6.1.2	Transfer of angular momentum	105
6.1.3	Gradient force	106

6.1.4	Scattering force	106
6.2	Theoretical model	107
6.3	Experimental micromotor fabrication and experimental setup .	111
6.4	Experimental and theoretical comparison	113
6.5	Optimisation of system and motor design	115
6.6	Conclusion	117
7	Conclusion	119
7.1	Outlook	121
7.2	List of Publications	122
A	Theoretical model	125
A.1	Introduction	125
A.2	Beam propagation	127
A.3	Gaussian beam solution of paraxial wave equation	132
A.4	Field propagation numerical model	132
A.4.1	A) propagation in homogeneous medium n_h	133
A.4.2	B) propagation in inhomogeneous medium $n(\vec{r}) = n_s + \Delta n$	135
A.5	Force calculation	137
A.5.1	One sphere one beam	139
A.5.2	Error evaluation	140
A.5.3	Two sphere array	141
A.6	Conclusion	142
	Bibliography	145

Chapter 1

Introduction

Radiation pressure of light is an intriguing concept in physics. Per definition [1] it is the pressure exerted on any surface exposed to electromagnetic radiation known as light. When absorbed this pressure equals the energy flux density over the speed of light, when the light is reflected the radiation pressure doubles [1]. Discovered theoretically by Maxwell in 1871 and experimentally proven by Lebedev in 1900 it has fuelled the imagination of many scientists. For example quite recently this concept lead to a proposed environmental friendly method of spacecraft propulsion via solar sails. Here the radiation pressure exerted by the sun would have been harnessed as means of exerting a force on the craft.

Terrestrial and microscopically, optical tweezers utilise the force exerted via light matter interaction to mechanically manipulate objects. Following the pioneering work of Ashkin and co workers over the last two decades, optical tweezers [2] have become a well established and important tool in the fields of biology, physical chemistry and soft condensed matter physics, where they offer a wealth of unique applications [3, 4].

1.1 Optical forces

Propagating light has an associated energy $h \times \nu$ and momentum $P = h \times \nu/c = h/\lambda$. If a photon of wavelength λ is incident on a mirror it undergoes reflection and a change in momentum will take place. As the momentum of the system must be conserved the mirror must experience a change in momentum as well, thus a force from the reflected photon is acting

on the mirror. The change in momentum of the reflected light is double as depicted in figure 1.1.

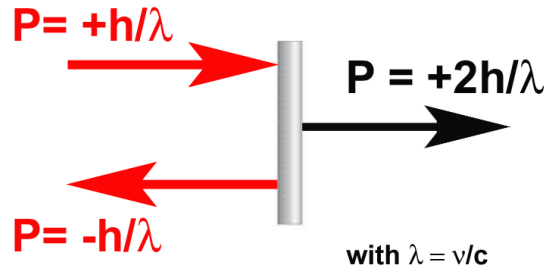


Figure 1.1: Momentum exchange between a mirror and an incident photon of a light beam. The picture shows the momentum (P) of the photon before and after reflection by the mirror.

As the magnitude of the force is only at the order of femtonewtons it has little impact on the mirror, in the microscopic regime it however enables to manipulate micron sized particles or spheres. Here microspheres (immersed in a host medium) encountering a propagating light field can¹ change the direction of the light field and thus alter its momentum. The force acting on the sphere can be calculated to $F = \frac{\partial P}{\partial t}$, where F is the acting force on the sphere and $P = m \times v$ (m = mass sphere and v its speed) its momentum and describes the underlying physical principle of optical tweezers.

Classically one can consider the forces in terms which depend on the sphere radius (r_{sphere}) with respect to the wavelength (λ), and are commonly separated into two different regimes:

- Rayleigh regime $\longrightarrow r_{sphere} \ll \lambda$
- Geometric or ray optics regime $\longrightarrow r_{sphere} \gg \lambda$

Both regimes will now be introduced respectively. Furthermore I will link them to known forms of optical binding.

1.2 Rayleigh regime

In the Rayleigh regime particles are much smaller than the wavelength of the incident field and can be considered as polarisable dipoles that respond

¹Provided that the sphere has got a different refractive index than the host medium

to an incident electromagnetic field. In this regime the field is approximated as uniform over the small scale of the sphere and only the small area over which the dipole interacts with the electric field is considered. The electric field will induce a polarisation in the atoms of the sphere and induce a dipole moment $\vec{p} = \alpha\vec{E}$ in the particle. Where \vec{E} is the electric field strength and α is the atomic polarisability dependent on the sphere radius and the relative refractive index $n = n_{sphere}/n_{hostmedium}$ to $\alpha = r_{sphere} \frac{n^2-1}{n^2+2}$. The force \vec{F} acting on the dipole is obtained from the interaction energy between the dipole and the field and can be written as [5]:

$$\vec{F} = -\nabla U = \alpha\vec{E} \times \nabla\vec{E} = \alpha\nabla E(\vec{r})^2 \quad (1.1)$$

where \vec{r} donates the position vector. Thus the induced dipole causes the particle to be drawn to the point in the field of highest intensity (provided that the sphere refractive index is higher than the surrounding media and therefore α positive), to minimise the free energy. Thus the electric field confines the sphere in a potential energy trap U to attain the lowest possible energy state. In the Rayleigh regime this force, which is dependent on the field gradient, which is also termed gradient force, is countered by the scattering force which tends to push the sphere along the beam propagation direction. The scattering force is attributed to the constant absorption and reemission of the incident light by the dipole induced in the sphere, shown in figure 1.2. Both forces can be calculated from the Lorentz force to [6]:

$$\begin{aligned} \vec{F}_{grad}(\vec{r}) &= 2\pi n_{host}^2 \epsilon_0 r_{sphere}^2 \alpha \nabla |\vec{E}^2(\vec{r})| \quad (1.2) \\ \vec{F}_{scatt}(\vec{r}) &= \hat{z} \frac{128 n_{host}^2 \epsilon_0 c \pi^5 r_{sphere}^4}{6c\lambda^4} \alpha^2 |\vec{E}^2(\vec{r})| \end{aligned}$$

where \vec{r} is the position vector of the beam, ϵ_0 is the dielectric constant, \hat{z} is the unit vector along the axis of propagation, c the speed of light and the field $\vec{E}(\vec{r})$ is given in time averaged form. For the particle to be stable trapped the gradient force must exceed the scattering force (commonly given as the ratio $\frac{F_{grad}}{F_{scatt}} > 1$).

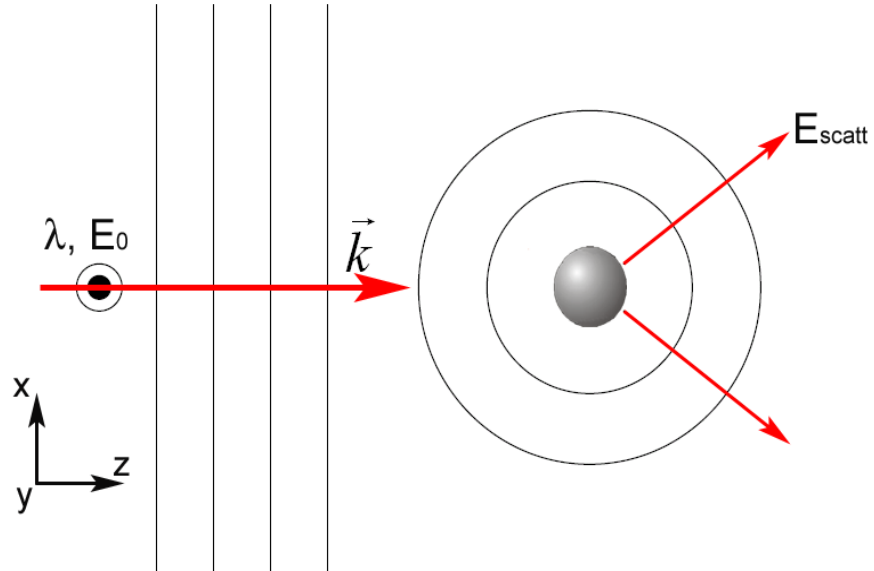


Figure 1.2: The picture shows a plane wave E_0 of wavelength λ , with wave vector k being incident on a Rayleigh sphere. Scattering is the dominant process when the field encounters the sphere and pushes the sphere along the z -axis (axis of field propagation), a strong optical gradient is necessary to confine the sphere in xyz .

1.3 Ray optics regime

In the ray optics regime the light matter interaction can be simplified with a geometric or ray optics approach. Here the light refraction through the particle induces the gradient force and reflection from the surface gives rise to the scattering force. The sphere can be viewed as a focusing element refracting the ray passing through it. The inherent transfer of momentum due to the change in direction results in a force which is oppositely directed to the change of the propagation direction of the ray. The magnitude of the force scales with the associated intensity of the light ray, see figure 1.3 A), drawing the sphere to the region of highest intensity.

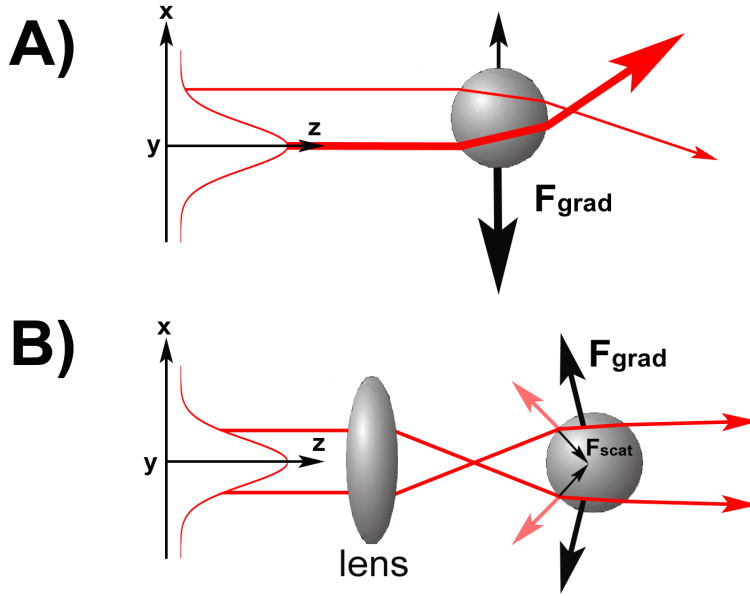


Figure 1.3: Representation of the forces acting on a sphere in the ray optics regime. A) In a Gaussian beam, the sphere acts as a high intensity seeker and gets drawn to the core of the beam. B) In a strongly focused Gaussian beam, which provides a strong enough gradient force to counter balance the scattering force. In the picture the sphere is drawn against the beam propagation direction to the focus of the beam, seeking a position where the acting forces equal each other out.

Partially reflected rays give rise to the scattering force that pushes the sphere along the propagation direction (z-axis) and confinement is only achieved in the xy plane due to the Gaussian shape of the beam.

When an additional focusing element (lens, depicted in figure 1.3 B)) is introduced, that provides a strong enough focusing of the light rays hence a strong intensity gradient, then the sphere experiences a gradient also in the propagation direction. This gradient force can yield to counteract the scattering force and the sphere finds an equilibrium position in 3 dimensions (xyz) where the net force is zero. Thus an optical tweezers is created and the sphere is confined in three dimensions.

1.4 Optically bound matter

In the experimental and theoretical work presented in this thesis, I will focus on a trapping regime where the wavelength is at the order or smaller

than the sphere diameter, this intermediate regime is classically termed Mie regime and more thorough calculations need to be employed (see for example Appendix A)). Here however the ray optics picture can intuit the underlying trapping concept.

A conventional single beam optical trap or optical tweezers relies on the strong intensity gradient from a focused beam to confine an object in three dimensions, see figure 1.4 A).

This is contrary to the trap realised in this project, which consists of two counter-propagating (CP) Gaussian beams. This counter-propagating geometry is necessary to achieve confinement in three dimensions as the net scattering force of one single divergent beam would propel the object in the beam propagation direction², as depicted in figure 1.4 B). Such microscopic counter-propagating traps (shown in figure 1.4 C)) can be realised either with weakly focused free space beams [2], by integrating two diode lasers in a flow cell [7] or using optical fibers [8]. Optical fibre traps have advanced rapidly in the last years especially in the realm of biophotonics [9, 10].

Intriguingly, if more than one object is confined within a counter-propagating beam trap, an optically bound array can be formed where the interplay between light and matter creates an self organised system of the objects [11]. Here the physical key to understand this form of optical trapping is the light redistribution by the trapped object itself in the beam propagation direction. This was first studied in a different geometry by Burns *et al* [12], who placed two microspheres in a line optical tweezers and found both spheres positions to be at discrete spacing at the order of the trapping wavelength. Here the underlying physical principle is the scattering of the spheres lateral to the beam axis, which creates a trapping potential for its nearest neighbour. This phenomena was coined optical binding and later on investigated theoretically [13, 14] and experimentally [15]. The same binding principle was also used to extend the trapped structure to multiple spheres in two dimensions [16] in an weakly focused Gaussian beam producing a large spotsizes. Here an optical crystal is formed on the surface of a dielectric surface to counteract the radiation pressure from the beam.

²Optical guiding where the object is only confined in the plane perpendicular to the propagation of the beam [2].

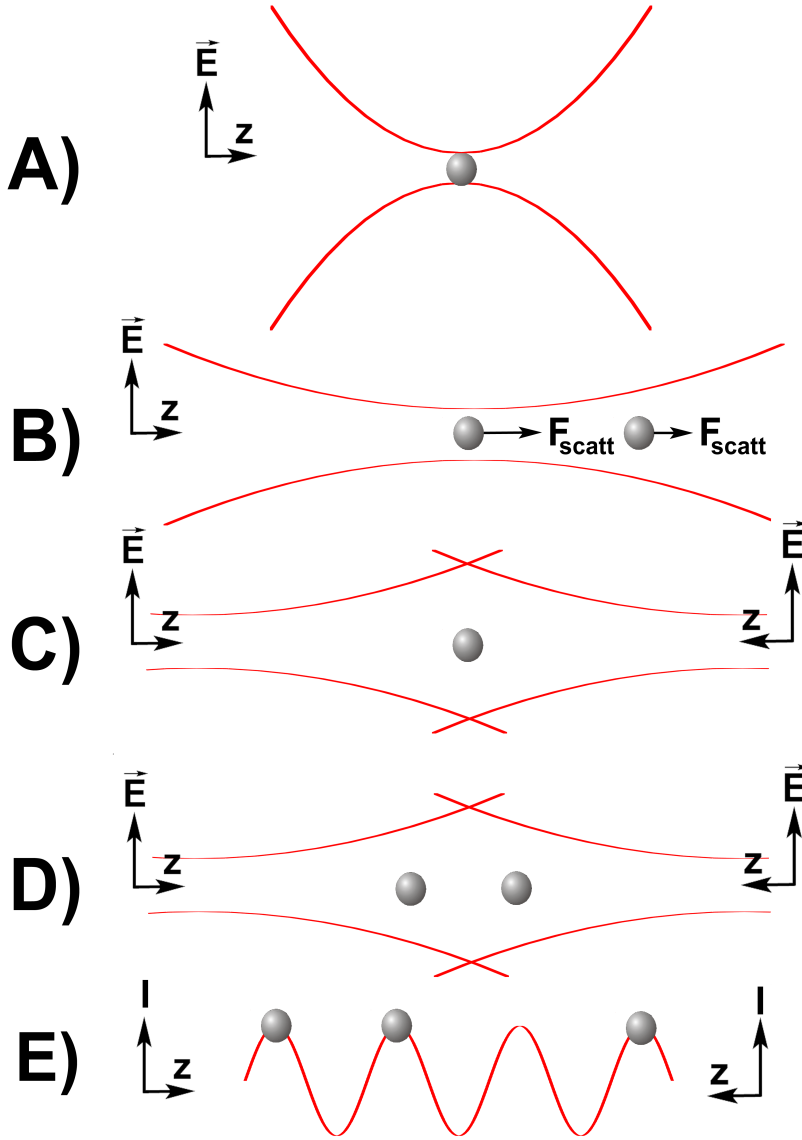


Figure 1.4: Different longitudinal trapping geometries: A) Single beam trap where a strong focused beam (emanating from the left hand side) creates a trapping potential U for a sphere at the beam focus. B) A weakly divergent beam cannot provide a strong enough gradient to counterbalance the scattering force or radiation pressure of the propagating field. The spheres only encounter a confining potential in the xy -plane and are getting propelled along the beam propagation direction z (optical guiding). C) Analogous to B) but with a second counter-propagating beam emanating from the right hand side. Here the two beams counter balance the acting scattering force and for equal field parameters a stable trapping potential is formed between the beam waists. D) Longitudinal optically bound array of two spheres the redistributed field past each sphere acts now to counter balance the scattering force from each counter-propagating beam. D) Standing wave trap, if both counter propagating fields are interfering with each other an interference pattern with multiple trap sites, spaced by $\lambda/2$ is formed. As shown in the picture not all trapping sites need to be occupied for the array to form.

Optical organisation through interactions of optical scattering in the beam propagation direction have been recently seen and allow interactions between micro particles separated by distances and order of magnitude larger than their individual diameters using a free space geometry [17, 18] and in a fibre trap [11]. Furthermore optical binding was observed with counter-propagating beams in interference fringes [19, 20] of droplets trapped in air. Such binding is not limited to a counter-propagating geometry but has also been observed in a horizontal geometry utilizing Bessel light beams [21, 22] where extended structures of up to 50 particles were reported, mediated by light matter interaction and gravity. Due to the direction of the trapping beams with respect to the orientation of the structure, this phenomenon is called longitudinal optical binding.

One might obviously argue that arranging and sculpting light fields to form multiple traps is nothing new. Optical binding however, is radically different to other extended structures in optical traps where there is a predefined optical trapping site. Here spatially localised high intensity regions (multiple optical traps) are created to organise and manipulate up to several hundreds of objects in up-to three dimensions. Such large scale trapping can for example be generated by time sharing of a single beam [23], holographic methods [24], the phase contrast technique [25], the use of nonzero order light modes [26], optical landscapes for particle sorting [27], evanescent light fields [28] as well as shaping of the phase front of a beam [29] can be used to design multiple trap sites. Interestingly trapping in the anti nodes of a standing wave [30] has been successfully used to create organised matter in a longitudinal geometry. Where the spacing between the trapped matter is, contrary to longitudinal optical binding, preset by the wavelength of the interfering fields, see figure 1.4 D).

All these methods are examples for predefined local trap sites or a shaped optical potential where the matter is located. In such geometries one typically ignores the light propagation past the trapped sphere which itself can lead to interesting interference effects [31], and can also be utilised for two dimensional trapping [32]. In longitudinal optical binding this very redistribution of the field is the physical key mechanism as it does not rely on shaped potential nor can the regular arrangement be attributed to interference effects of the trapping light. In principle this redistribution effect could allow for large scale self-organised system, as long as the forward scattered light is strong enough to maintain the array, as depicted in figure 1.5.

Such many body colloidal systems are likely to have impact across the bio-

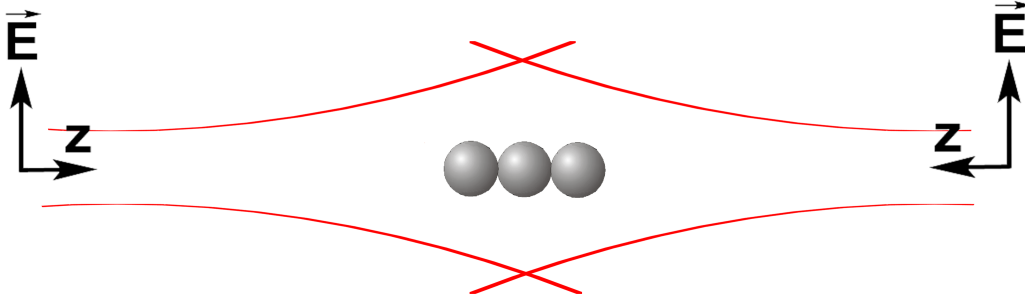


Figure 1.5: A collapsed array between two counter-propagating (CP) fields is shown. When the forces acting in the propagation direction of the redistributed fields between the spheres cannot provide a balancing force equal or greater than the radiation pressure on the outer spheres, then the array collapses and a chain of spheres is formed.

logical and colloidal sciences and indeed may lend themselves to be a very powerful future method for creating self assembled crystals in up to three dimensions.

The sensitivity of the macroscopic parameters of the arranged structures (distance between the bound objects) to the internal properties of the bound objects (particles, cells) as well as the parameters of the surrounding medium (refractive index) could provide a sensitive measurement method for those pertinent parameters itself or to minute changes of them.

In the work at hand I will touch a new aspect of optical binding from a experimental and theoretical point of view. During the course of my PhD it turned out that especially the understanding of this phenomenon is not trivial and needs a in depth analysis of even the simplest case of optical binding in one dimension with two bound objects. Therefore I will focus in more detail and more carefully on this pivotal 1D binding that is presently still not fully understood.

1.5 Synopsis

The thesis is structured in three main parts; the theoretical model section, the optical binding section and an micromotor section.

A detailed description of the underlying theoretical model is given in the appendix section as it was not developed by myself. Over the course of my

PhD, I used and later rewrote the theoretical model. In my thesis it is used throughout to predict and in some instances governs the conducted experiment.

The first chapter introduces the experimental rig used with modifications in all subsequent chapters.

During initial experiments I discovered that two optically bound spheres can exhibit bistability due to the coupling between spheres and light field. This nonlinear phenomenon is described in detail in the second chapter.

In the third chapter I utilised two-photon fluorescence to visualise the light field in optical binding and explain qualitatively the light redistribution within an array.

The coupling between the two spheres via the light fields lead on to the investigation in the fourth chapter, where Brownian noise is used to probe the coupled response of the bound spheres. Also an *in situ* method is developed to determine the spring constants acting in an array.

The fifth chapter rounds off my thesis, here I applied the knowledge acquired in optical binding to investigate the light matter interaction of an optically driven micromotor, specifically I develop a novel method to predict and enhance the efficiency of a light motor system.

Chapter 2

Experiment

This chapter will introduce the experimental setup utilised throughout my thesis.

The setup to investigate longitudinal optical binding is a counter-propagating geometry [17, 11] based on a dual beam fibre trap [8]. The trapping principle of the fibre trap relies on the balancing of the acting scattering force in the propagation direction with a second counter-propagating (CP) beam and was first demonstrated by Ashkin [2] and Roosen *et al* [33, 34], with two weakly focused Gaussian beams in a free space geometry. This longitudinal trapping geometry was later revisited by Constable [8] who used CP beams emitted by two opposing optical fibres. Realising such a longitudinal trap with fibers has several key advantages:

The optical fibre trap does not need a large amount of optics for its construction, as it is only required to couple the light into the fibres. If a fibre coupled laser is used, these coupling optics are rendered unnecessary.

Furthermore the trapping volume is superior over conventional single beam tweezers [10] and can be easily extended by increasing the separation between the fibres. This importantly allows in the domain of longitudinal optical binding for another parameter to be studied and I shall present experiments hereunto in a later section.

The output beam profile of a single mode fibre is of Gaussian shape and independent of the beam quality of the trapping laser.

Such fibres can with relative ease be aligned counter-propagating under a microscope and are clearly superior over a free-space geometry where there is no point of reference (fibre front surface and cladding of the fibre) to aid CP alignment of the fields.

Furthermore beam parameters can be determined with relative ease: For example the mode field diameter $2 * w_0$ (waist size) is provided by the manufacturer or can be measured via a simple imaging setup, as well as the position of the beam waist, located at the individual fibre end facets and clearly visible under a microscope.

These beam parameters are very important to accurately model optical binding. Their exact determination is crucial to get meaningful theoretical results and are rather difficult to obtain for a free space setup [17], therefore the choice fell on the fibre optical trap similar to Singer *et al* [11] who as well investigated longitudinal optical binding or Guck *et al* [9] who utilised a fibre trap to investigate the properties of cells.

This chapter is chronologically laid out as the experiments initially progressed over the first year of my PhD, parts of this work were done in cooperation with Philip R.T. Jess (fibre trap), Lynn Paterson and Muriel Comrie (work on biological samples). In the beginning of this chapter I describe the optical fibre trap, which was setup with an additional helper tweezers [11] to easily load the trap and manipulate the array. Then a description of a simple particle tracking program follows that enables the localisation of the optical bound matter in the trap. Further I compare different types of fibers, used in the trapping setup. Initial experiments with Chinese Hamster Ovary (CHO) cells, that exhibit optical binding [11] as well as dielectric spheres were investigated. This led to investigations that concentrated on dielectric spheres arrays with a varying refractive index of the host solution.

The aim of this chapter is to present the basis of the experimental methods and investigations used throughout my thesis.

2.1 Optical fibre trap

The design of the dual beam fibre optical trap as shown in figure 2.1 is a straight forward process. Here I will give an overview of the key components that were used to setup the fibre trap and to investigate optical binding.

Optical fibres lie at the heart of the trap realised in this thesis and will be investigated in the continuation of this chapter, specifically I will take a closer look at single mode and multimode fibres and their suitability to conduct studies in optical binding. Both types of fibers were illuminated by a 15W Diode pumped Ytterbium Fibre Laser (IPG Photonics) linearly polarised

with a calculated coherence length of less than $1mm^1$ and a collimated beam diameter of $5mm$, which fills out the input aperture of the fibre coupling optics and make expansion optics unnecessary. The laser beam is split with a 50:50 beam splitter cube (BS) into two arms. The optical power in each arm could be separately adjusted with a variable neutral density filter (ND) before entering the coupling optics.

By carefully choosing the optical path difference to be well above the laser coherence length, standing wave effects [30] were excluded.

One fibre (F1) was mounted on a cover slip in a fixed position above the imaging setup. The second fibre (F2) was mounted on an XYZ stage and could be aligned with F1 much like in a fibre to fibre pig tailing setup with a variable distance between the two fibre ends of about 10 to $150\mu m$, see figure 2.1 (right).

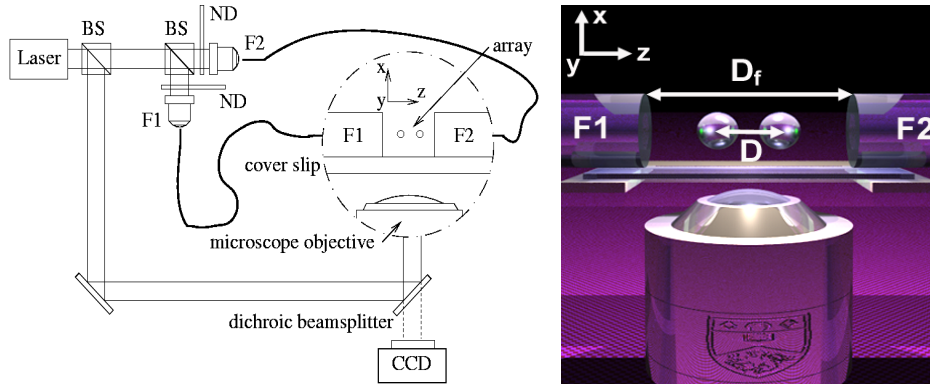


Figure 2.1: Fibre optical trap setup. Left: Light at $1070nm$ from a Laser is coupled via two ND filters into fibre F1 and F2 to ensure equal power distribution. Right: The counter-propagating light fields at $1070nm$ emerge from two single mode fibers (F1 and F2) with a variable separation of the fibre facets D_f . The array is formed in the gap between the two fibers (F1 and F2) with D being the separation of the spheres and D_f the fibre separation. At equal power distribution the array center of symmetry ($D/2$) coincides with half the fibre separation ($D_f/2$). A separate helper tweezers was incorporated through the observation setup via a dichroic mirror to initialise the array.

The correct alignment of such a trapping geometry is however important. Knowing the acting trapping forces, shown in figure 2.2 can intuit on how a misaligned fibre trap can perturb a trapped particle or array. The trapping forces can be resolved into two main components (shown in figure 2.2 (a)):

¹from IPG: $L_{coherence} = \frac{2*c}{\pi} * \frac{\ln(2)}{halfpowerbandwidth} = 0.44 * \frac{\lambda^2}{Linewidth}$ with $\lambda = 1070nm$; $Linewidth = 1.23nm$

- The gradient force, which draws the particles in the direction of increasing intensity, towards the centre of the fields for Gaussian beams.
- The scattering force, which pushes the particle in direction of the beam propagating direction.

If the fibre trap is perfectly aligned (shown in figure 2.2 (b)), the acting forces from both beams cancel each other and the particle or array finds its equilibrium state at half the fibre separation ($D_f/2$).

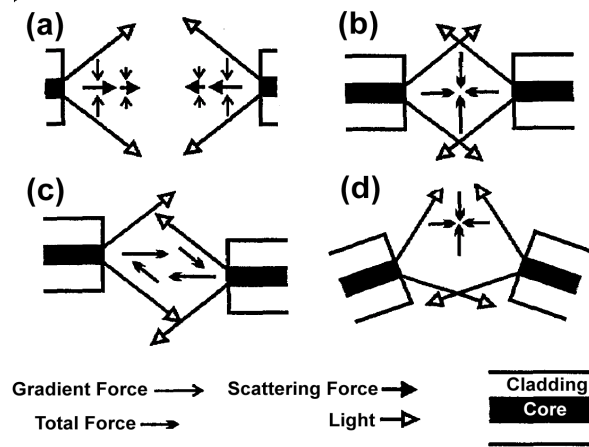


Figure 2.2: Fibre optical trapping geometry: (a) Schematic of the gradient and scattering forces for each of the two fibres that form the trap. The length of the arrows indicates the approximate strength of the acting forces. Images (b) to (d) indicate the direction of the total forces when the fibres are (b) perfectly aligned, (c) translational misaligned and (d) rotational misaligned. Figure obtained from reference [8].

Provided that both beams are of equal intensity, this on the other hand gives the possibility to move the trapped sphere along the axis of the CP fields by attenuating one beam with respect to the other. We can distinguish two different types of fibre misalignment:

- Positional misalignment: Both fibre ends are counter-propagating aligned but offset from each other, as depicted in figure 2.2 (c). Such misalignment can be easily spotted, as the array starts to move in a circular motion as the spheres are guided by either one beam (in figure 2.2 (c) this would result in a clockwise movement of the array).
- Rotational misalignment: In this case both fibres still have their centre aligned along the same axis, but are at skewed angles. Here the array would be formed off the central axis (as shown in figure 2.2 (d)).

Of course it is possible that both types of misalignment happen at once. The exact counter-propagating alignment of the two fields to within a fraction of the beam waist is critical for good trap operation. The alignment was observed and readjusted if necessary with an imaging setup.

The imaging system consisted out of a $50\times$ Mitutoyo microscope objective (NA=0.42 working distance= 15mm) or a $60\times$ Newport microscope objective (NA=0.85 working distance= $250\mu\text{m}$) that had an additional single beam tweezers incorporated through it. This auxiliary tweezers was operated by coupling part of the fibre trap light into the optical path of the imaging system. This helper tweezers was used to load the optical fibre trap as the trapping area is (due to the large cladding of the fibre) approximately $60\mu\text{m}$ above the glass cover slip, so every sphere in the array need to be separately tweezed and moved into the fibre trap. Furthermore it gave the possibility to alter the array *in situ*. The array was observed through a dichroic beam splitter with a CCD camera (Watec WAT 902DM2S) connected to a computer with a frame grabber card to capture images. A short-pass wavelength filter in front of the camera was used to block out the trapping wavelength. The experiment was illuminated from above the cover slip from a distance of 200mm to ensure uniform illumination and to keep additional heating of the sample to a minimum.

2.2 Data analysis

To obtain position trajectories from the digital images it is important to accurately calibrate the pixel size of each image. This can be achieved by taking images from a Microscope calibration grid with a pitch of $100\mu\text{m}$ in the z and y plane on top of the cover slip. Here the measurement error was reduce by averaging over multiple images and by choosing the calibration pitch as large as possible. The calibration was verified by measuring the size of a $100\mu\text{m}$ size structure, the error in this measurement was $<1\mu\text{m}$. This gives an estimated overall calibration error of $\pm 1\%$.

From the calibrated images one needs to determine the fibre separation D_f (see figure 2.3) which effects the distribution of the optical field and its variation can have significant influence on the array formation. D_f was measured at the individual corner of each fibre. Due to the large cladding diameter of the fibre ($125\mu\text{m}$) shadowing occurs², making an exact determination of

²Due to the limited resolution depth of the microscope.

D_f at the position of the fibre core more difficult. This method was verified by remeasuring a calibrated fibre trap in a Scanning Electron Microscope (SEM) leading to an estimated accuracy of better than $3\mu\text{m}$ and an estimated accuracy of $\pm 4\%$ by repeated measurements for the applied video analysis technique.

Particle tracking was performed by utilising a LabVIEW script with a pattern recognition algorithm³ to determine the position of each sphere or cell within each frame of the captured movie. In the first frame the spheres are selected and then convoluted at every consecutive frame with this first image. The best match of the convolution gives the center position of the sphere. The versatility of the approach lies in the convolution algorithm as a region of interest is selected, that can be spheres or cells but also the edges of the fibers to track *in situ* variations of their separation D_f .

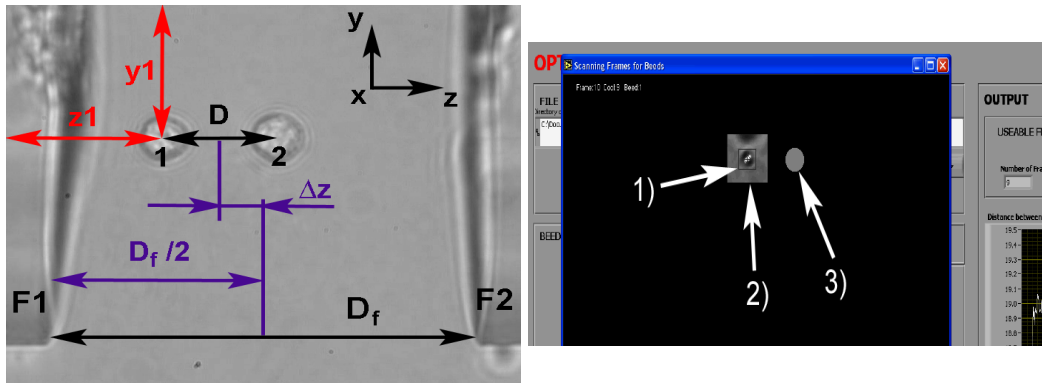


Figure 2.3: Left: The picture shows the geometrical layout of the images taken, from which the LabVIEW algorithm finds the y and z position of each sphere or cell (marked 1 and 2) in every frame of the captured movie. It then calculates the distance D between the beads and Δz the distance of the central line between the beads $\frac{D}{2}$ to a reference center line, located between the two fibers $\frac{D_f}{2}$. $\Delta z = 0$ would correspond to a perfectly centrosymmetric array between the two fibers. Δz being positive indicates a displacement in μm of the arrays symmetric axis towards fibre surface F2 (negative $\Delta z \Rightarrow$ displacement towards F1). Right: Screen shot of the LabVIEW tracking program depicting its key features. 1) marks the currently tracked object. 2) is the region of interest which is overlaid over the previous known position of the object to enhance the tracking algorithm. 3) once an object is identified it is overlaid with a grey spot to eliminate multiple recognitions of similar objects.

The tracking program gives the y and z position of each object (see figure 2.3 for cells) $y_1 z_1$ for object number 1 and $y_2 z_2$ for object number 2. From this data the distance (D) between the center points of the objects as well as the displacement (Δz) of the center point between the two objects (at

³Standard LabVIEW convolution algorithm included in LabVIEW Vision Development Module library called IMAQ ©National Instruments.

$\frac{D}{2}$) relative to the central symmetric axis between the two fibers (at $\frac{D_f}{2}$) was calculated. The error in the position of the object can be better than $0.5\mu m$ dependent on the number of frames. As the error of the position is directly correlated to the number of frames that are analysed as well as how often the objects are moved for short static measurements the error can be estimated to be $0.5\mu m$ while for long dynamic measurements it can increase to $2\mu m$ in extreme cases. This error is related to the pattern matching convolution algorithm. As all consecutive frames are correlated to the initial image, here for example drift in the imaging setup can induce an image blur and increase the error over time. Although the algorithm is 2D rotation invariant it does not account for variation in 3D which can occur when cells are trapped. At this point I am well equipped to do first initial measurements with the fibre trap.

2.3 Fibre trap design considerations

Designing a fibre trap one may initially believe that a multi mode fibre is preferable to a single mode, as light coupling is more efficient and alignment easier. Therefore I compared a multi mode with a single mode fibre trap in their ability to trap CHO cells as well as spheres.

For the multi mode fibre (cladding diameter = $125\mu m$, core diameter = $50\mu m$, NA = 0.2) a $20\times$ microscope objective (NA = 0.4, focal length = $9mm$, working distance = $1.7mm$ and entrance aperture = $6mm$) was used. The following mode profile, shown in figure 2.4 (left) was obtained with this fibre and shows a speckle pattern. The different path length of the modes within the multi mode fibre causes this speckled pattern due to the interference of the modes at the fibre output. A super-Gaussian is fitted to aid the eye for comparison, the measured spot size⁴ was $45-50\mu m$.

With the single mode fibre (mode field diameter at $1060nm = 6.2 \pm 0.5\mu m$ and NA = 0.14) a $10\times$ microscope objective (NA = 0.25, focal length = $16.5mm$, working distance = $5.5mm$ and aperture = $7.5mm$) was used to couple into each fibre. A Gaussian mode was obtained with this fibre (shown in figure 2.4 (right)), the spot size was $6.6\mu m$. From the Gaussian fit⁵ the beam waist w_0 was calculated to $\sqrt{2} * 2.43 = 3.43\mu m$ at a wavelength of $1070nm$ for both measurements. These parameters are reasonably close to

⁴Diameter of the spot image on the fibre surface.

⁵ $I = A * exp(-(r/w_i)^2)$ with $w_i = w_0/\sqrt{2}$

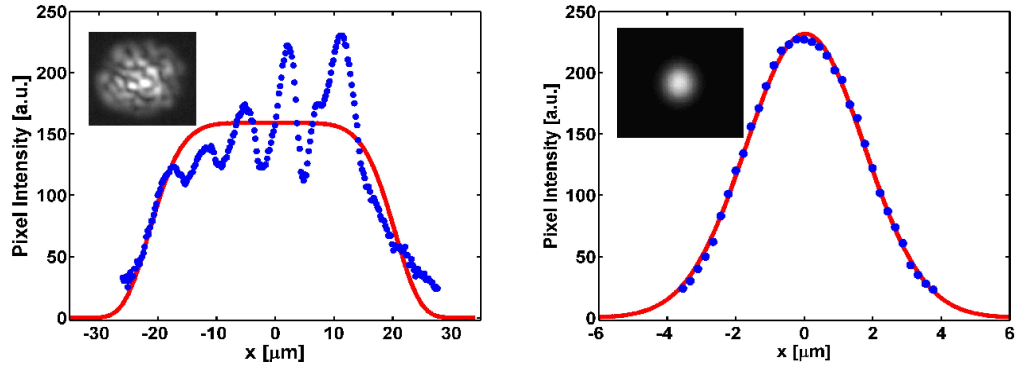


Figure 2.4: Left: Multi mode fibre profile with a 6^{th} order super-Gaussian fit. Right: Single mode fibre profile with a Gaussian fit. Inset shows the corresponding intensity near field pattern, not to scale.

$3.1 \pm 0.25 \mu m$ (including the error) given by the manufacturer⁶ and will be used in the theoretical simulations presented in the following chapters.

In both traps arrays of up to three Chinese Hamster Ovary (CHO) cells were observed. If a two CHO cell array is moved⁷ the volume occupied in a multi mode trap is far bigger than in a single mode trap due to the bigger emission cone of the multi mode fibre. The super-Gaussian fit of the multi mode line profile in figure 2.4 contains 6 regular Gaussian curves, due to the mode structure it is not a full cone where the trapped cells occupy preferably the maxima. Figure 2.5 shows the position trajectory points red and blue for each CHO cell between the two fibers while being displaced several times over more than 2000 measurements.

Comparing both graphs shows that the y position spreads over less than $1 \mu m$ for the single mode and $7 \mu m$ for the multi mode fibre. Trapping within a single mode fibre in the transverse propagation plane is therefore well defined due to the sharper intensity peak as compared to a multi mode fibre with a wide emission cone. Specifically the multi mode fibre trap has an approximately 7 times bigger trapping volume than a single mode fibre trap, which can be useful for guiding or cell handling applications in biophotonics [10]. Spheres can also be trapped in a multi mode fibre trap, polymer spheres up to $100 \mu m$ can be bound in a chain [10], as they do not exhibit array formation. If smaller silica spheres of about $5.17 \mu m$ are placed in the trap then

⁶Given as mode field diameter (MFD) where intensity has decreased to $1/e^2$ which is equal to spotsize and $2 \times w_0$ [35].

⁷By varying the power output in one fibre with respect to the other.

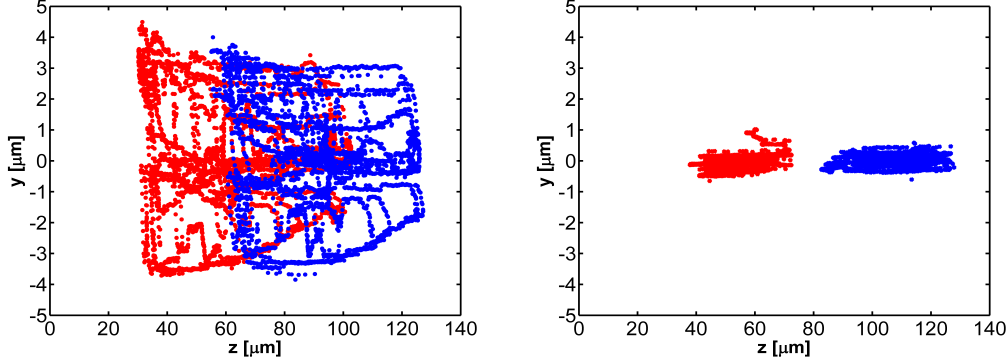


Figure 2.5: Comparison of the z and y positions of a two CHO cell arrays in a multi mode fibre trap with $32\mu\text{m}$ separation D (left) and single mode fibre trap with $54\mu\text{m}$ cell separation D (right). Red and blue crosses show the position for each of the cells while being displaced over several frames. $15\mu\text{m}$ is the approx. diameter of the individual cells with a constant fibre separation of $120\mu\text{m}$ and 100mW trapping power for both traps. Although the cell diameter is constant the cells in the single mode trap exhibit a larger separation leading to non overlapping tracking trajectories.

multiple trapping positions can be observed, this is shown in figure 2.6.

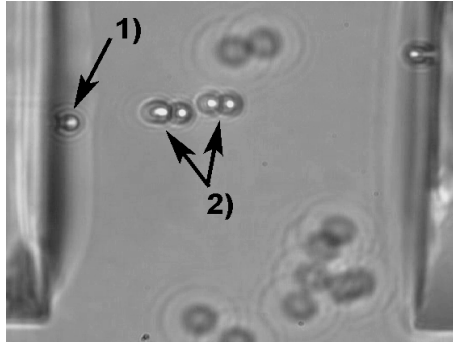


Figure 2.6: $5.17\mu\text{m}$ spheres in a multi mode fibre trap. 1) One sphere is captured in a single intensity peak and guided to the left. 2) Four spheres are trapped at positions where intensity maxima overlap. Two collapsed arrays are formed, with the arrays being at different positions in xyz .

These arrangements are not well defined and happen randomly. Spheres are guided past each other as they are guided within one intensity maximum and trapping only occurs if two maxima overlap.

Attempts were made to get a coherently illuminated beam profile for the multi mode fibre by wrapping the fibre around a post of 6mm in diameter. The beam profile improved only marginally and a speckled pattern was still observed.

Here I conclude that multi mode fibre can be used to trap sizes larger than $10\mu m$ and open up the possibility to form 3 dimensional sphere chains within overlapping mode maxima. Also they give the possibility to utilise multi mode fibre coupled high power diodes as a cheaper alternative to a laser to fibre coupling setup. At this point further experiments were only conducted with the single mode fibre trap to obtain stable trapping along the beam propagation axis with strong confinement in the xy-plane, thereby limiting array formation to one dimension.

2.4 Investigated matter

As indicated in the previous section different preliminary experiments were carried out with cells and microspheres, here I want to focus on characterising these radically different types of matter and concentrate in particular on the refractive index of them, which plays a prominent role in optical binding.

2.4.1 Chinese Hamster Ovary cells

One aspect of my investigations focused on Chinese Hamster Ovary (CHO) cells that were previously observed to form optically bound arrays [11]. In the experiment the cells were diluted in Minimal Essential Medium (MEM)⁸, which was added to the experiment to achieve a lower cell density when necessary. The cells used in the experiment were roughly characterised (size and refractive index) to aid comparative measurements with spheres. The size and shape of the cells vary strongly within one sample; the averaged cell diameter used in the experiments ranged between 11 to $17\mu m$ (measured with cell culture counter).

⁸MEM is a cell culture medium and contains amino acids, salts, glucose and vitamins to nourish a variety of cells.

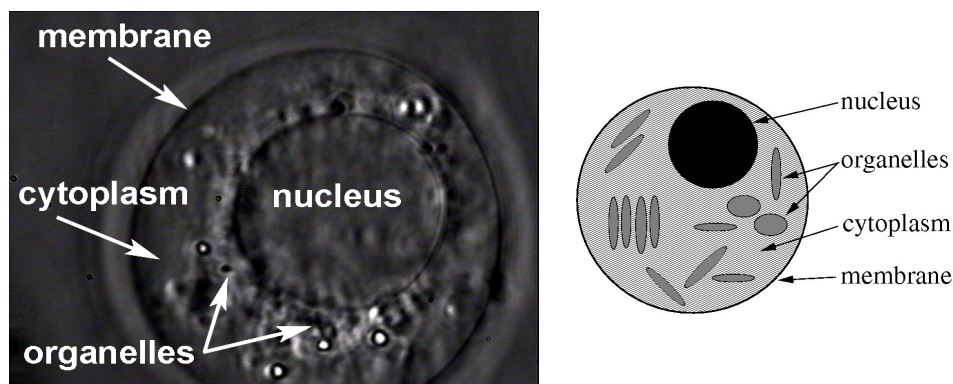


Figure 2.7: Left: Phase contrast image of a Chinese Hamster Ovary (CHO) cell. Basic contents are marked in the image. Right: Refractive index distribution within a cell different shadings correspond to a different refractive index value n , as shown in the table.

The overall refractive index of a cell can be estimated by summing over the volume contents of it. With the data from [36]:/Users/klaus/Desktp/3DpotentialDATA copy.png

cell content	n	$f[\%]$
nucleus	1.39	5-10
cytoplasm	1.37	50-80
organelles	1.42	5-15
membranes	1.46	0.5-1

The refractive index difference (Δn) between host solution and cell was estimated to be around 0.04 to 0.05 for a wavelength of $589nm$, this is compared to regular microspheres in water ($\Delta n \approx 0.1$) very low.

A first set of experiments focused on CHO cells arrays (see figure 2.8 1), 2) and 3)) and their center separation D . Unfortunately no conclusive correlation between their size (between 10 to $18\mu m$) and the array separation of two CHO cells (between 30 to $60\mu m$) could be established at this stage.

By attenuating the optical power in one fiber relative to the other, results in a displacement (Δz) of the array within the fiber trap, a counter intuitive phenomena was observed. In some cases of these studies it was found that one cell moved faster than the other, causing the distance D to either reach a minimum when displaced towards one fiber end (catching up with the other

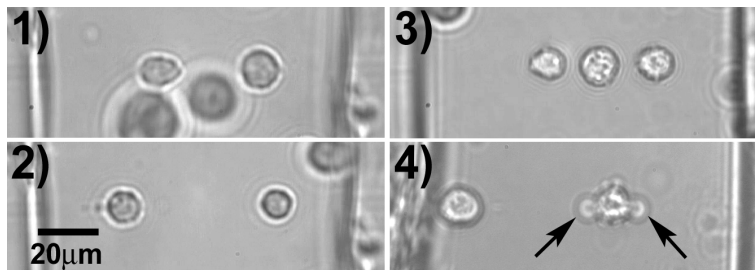


Figure 2.8: CHO cell array formation: 1) and 2) shows example pictures of a two cell array with separations D between 30 to $60\mu m$. 3) Three CHO cell array. 4) Two CHO cell array, with the right hand cell exhibiting optical damage (bubble formation) at the points where the optical fields enter and exit (marked with arrows).

cell) or a maximum when displaced to the other fiber end (moving ahead of the other cell). One CHO cell in the array seemed to interact stronger with the optical field than the other, it moved faster when the array was displaced within the trap. After 10 minutes in the trap such a fast moving cell showed severe signs of photon damage (shown in figure 2.8 4)). The cell exhibits bubble formation at the sides where the optical field penetrates at $100mW$ emerging from each arm whereas its counterpart does not. Investigations of single cell damage showed that some CHO cells can exhibit damage after 10 minutes at $80 - 100mW$ emerging from each arm. In other cases a single cell did not show any damage after 20 minutes at $200mW$. This led to the conclusion that different cells interact stronger or weaker with the two emerging optical fields, resulting in damage and in faster displacement in an optically bound array, which could not be explained by their size variation. In an experiment where the cell switched positions in the array, this could be verified and a possible side dependence eliminated (figure 2.9).

This strong variation in the interaction with the optical field can be due to the difference in contents of the cells. Just before a cell splits it has got double the contents of a regular cell. This can furthermore qualitatively explain the large variation of the cell array separation D .

Importantly, optically bound CHO cells are the largest matter to form an array to date (each has a radius of about $\approx 8\mu m$). It is worthwhile to note that the refractive index difference between the cell and the host medium is low in comparison to beads in regular water and changes in Δn seem to strongly affect the array formation.

This correlation lead to the investigation in the following section where microspheres arrays were investigated in dependence of Δn .

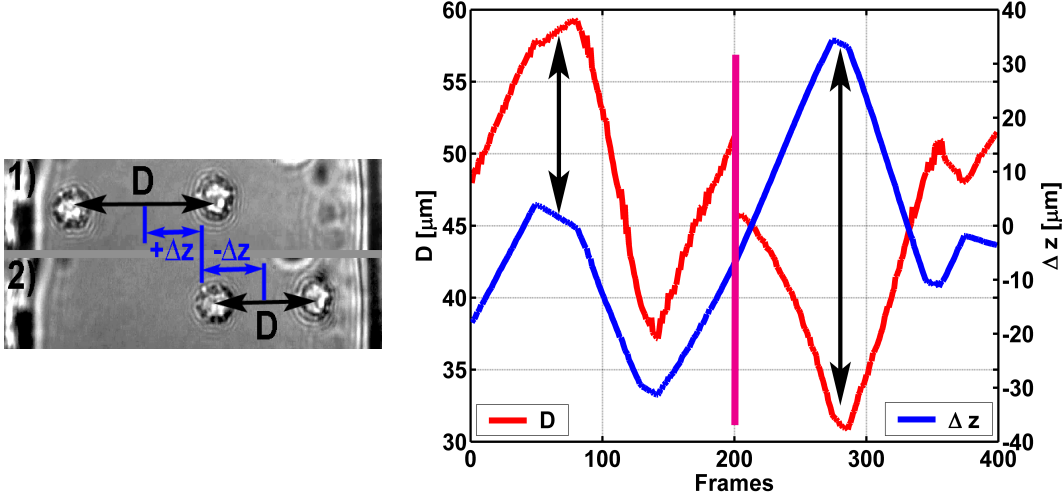


Figure 2.9: Left: By attenuating either one field the array of two CHO cells can be displaced in the fiber trap. 1) Left hand field attenuated, the array is guided to the left - D increases Δz is getting positive. 2) Right hand field attenuated - D decreases while the array center Δz is getting negative. The images sequence shows that the left cell is moving faster than the right one. Right: Corresponding displacement plot, Δz , of the array center (blue) and the array separation D . It can be seen that one cells moves faster, causing D to reach either a minimum or a maximum when displaced towards either fiber. At frame 200 (magenta line) the array was flipped to verify that the behaviour is dependent on the cell not on the side at which it resides (marked with black arrows).

2.4.2 Microspheres

Follow up experiments were carried out using silica⁹ microspheres in solution from Bangs Laboratories and Duke Scientific. In this section I will briefly evaluate the key material parameters for optical binding, especially the refractive index difference (Δn) between the sphere (n_{sphere}) and the host medium (n_{host}). Accurate determination of Δn is crucial for the subsequent theoretical modelling of optical binding.

Refractive index measurements on silica microspheres were carried out by Bangs laboratories using index matching technique and the following three results obtained $n = 1.431, 1.442$ and 1.458 at $\lambda = 588.9nm$.

Duke Scientific gives the refractive index of their silica spheres to 1.40 to 1.46 at $\lambda = 589nm$ (at a temperature of $23^\circ C$).

For fused silica the refractive index dependence on λ can be approximated

⁹The refractive index of polystyrene is $n = 1.59$ at $589nm$ (Bangs Laboratories) and $n = 1.57$ for $1064nm$ [11]. Polystyrene was not used, as the paraxial approximation would start to break down for high refractive index contrasts.

with the following formula (this is an approximation of the dispersion equation [37], with parameters A, B from [38]):

$$n = A * \left[1 + \left(\frac{B}{\lambda} \right)^2 \right] \quad (2.1) \quad \begin{array}{l} n = \text{refractive index} \\ A = 1.4485 \\ B = 48.7436 \end{array}$$

Using equation 2.1 a refractive index of $n = 1.458$ at $588nm$ and $n = 1.451$ at $1070nm$ is obtained. The results show that there is a shift to a lower refractive index value of $\Delta n \approx 0.007$.

Although the refractive index of the spheres can be more accurately calculated, factors such as the storage time can also alter the refractive index of the sphere, as water is absorbed by the sphere¹⁰[39] due to its porosity and can not be fully accounted for. Hence for the simulations an estimated refractive index of $n \approx 1.41$ for 1 and $3\mu m$ sphere diameter and $n \approx 1.42$ for $5\mu m$ sphere diameter, with errors $\pm 4\%$ was used ($n = 1.43$ was used in previous work [18] for simulations with two counter-propagating free space beams).

The sphere radius r_{sphere} has a size distribution (Bangs laboratories) such that the standard deviation (STD) of the mean diameter for $3\mu m$ is given as $< 10\%$. This variation will be accounted for in the next chapter to aid a comparison and error evaluation between experimental and theory.

To mimic the refractive index difference between host solution and CHO cells and to investigate the array formation for a varying refractive index of the host solution the spheres were diluted in a de-ionised (DI) water and sucrose solution [11]. The refractive index of the solution was measured with a recalibrated Brix refractometer¹¹.

The Brix refractometer is calibrated for the yellow sodium D-lines at $589nm$ ¹² from references [40] and [41] a conversion plot %Brix to n was obtained, see figure 2.10(red crosses). Experimentally the refractive index was measured with light at $1070nm$ emerging from the laser source through the Brix refractometer. The scale was read through an IR viewer to obtain the Brix equivalent for the used wavelength. A shift of -0.9% Brix for $1070nm$ for different sucrose solution was measured. However there is a significant error in

¹⁰The refractive index changes from 1.36 to 1.42 (at $575nm$) over a period of $800h$ [39].

¹¹Brix refractometers are usually used in the Wine industry and by bee keepers to measure the sugar content of wine or honey. It is basically an Abbe refractometer that measures the critical angle but is calibrated in %Brix rather than refractive index.

¹²The sodium line spectrum is dominated by a bright doublet at 588.99 and $589.59nm$.

this measurement as internal dispersion compensation optics are optimised for $589nm$.

A better approximation for $1070nm$ can be obtained by fitting a curve to the conversion data and linearly shifting it to a given refractive index value from literature sources. The literature gives the refractive index of DI water to:

Reference	n	Temperature	λ	Pressure
IAPWS [42]	1.326	0°	$1.013\mu m$	1MPa
B. Richerzhagen [43]	1.325	10°	$1.064\mu m$	n.a.
B. Richerzhagen [43]	1.320	50°	$1.064\mu m$	n.a.
P. Schiebner [44]	1.328	30°	$0.8\mu m$	n.a.

This data results in an interpolated shifted line fit in graph 2.10, where the following formula (quadratic fit) was used to calculate the refractive indexes from Brix [%] to n :

$$n = 6.857 * 10^{-6} * brix^2 + 1.397 * 10^{-3} * brix + n_\lambda(T) \quad (2.2)$$

Here $n_\lambda(T)$ denotes the temperature (T) dependent refractive index of DI water, that was interpolated for the graph (see figure 2.10) to about $25^\circ C$.

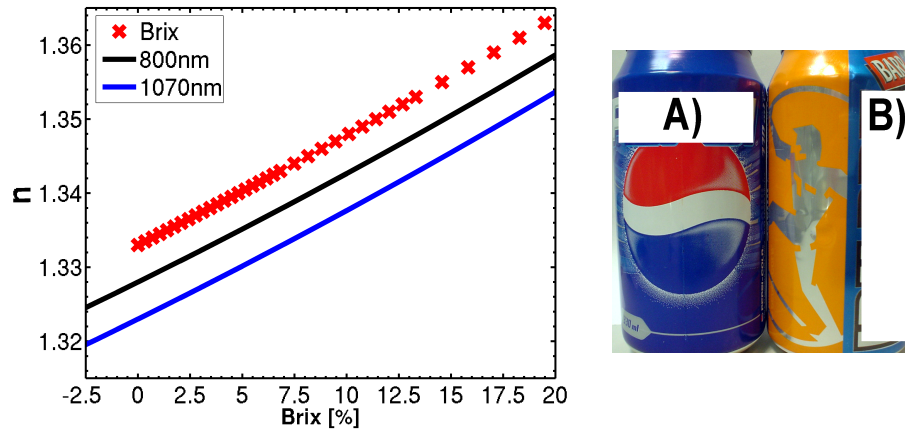


Figure 2.10: Left: Graphs shows the conversion from Brix to refractive index. Crosses show the conversion data at $589nm$. Solid line represents the fit through the crosses and linearly shifted to the refractive index of DI water at $1064nm$ (blue) and $800nm$ (black) at a temperature of $25^\circ C$. Right: Here the sucrose content of two popular soft drinks is compared with A) = 11.2% Brix and B) = 10.5% Brix.

To obtain a lower refractive index than with DI water, some measurements were also carried out with D_2O (heavy water) having a refractive index of 1.328 [45] for the sodium D-lines. The linear approximation (formula 2.2) from DI water gives a refractive index of 1.320 at $1070nm$ and similar for $800nm$. The refractive index of D_2O was measured to approximately -2.5% Brix at $589nm$ this converts from the formula above to $n = 1.320$ for $1070nm$, this is in agreement with the interpolation of formula 2.2 for negative Brix values.

At this point I want to continue solely with the term $\Delta n = n_{sphere} - n_{host}$, denoting the refractive index difference or refractive index mismatch between the sphere and the host medium. At this stage it is possible to perform measurements for a variable Δn of 0.03 to 0.09 with an accuracy of ± 0.001 .

As studies with the CHO cell arrays indicated, a low refractive index difference between host solution and bound matter is a key parameter in the formation of optically bound arrays. In a follow up experiment the dependency of Δn to the number of spheres that can be bound before the array collapses and a chain is formed [17] was investigated. Figure 2.11 shows the maximum number of $5.17\mu m$ sized silica microspheres that form an array for different Δn .

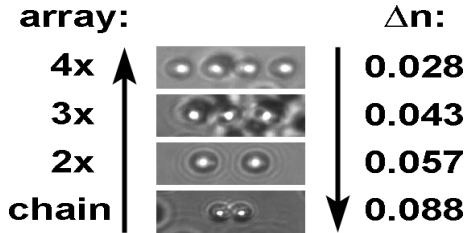


Figure 2.11: Array formation dependency on Δn for $5\mu m$ silica spheres. Number shows maximum number of beads before the array collapses. For $\Delta n=0.088$ the spheres have collapsed into a chain. With decreasing Δn more spheres can be bound before the array collapses.

Here we clearly see that the smaller the refractive index difference between matter and host solution, the more particles can form an optically bound array. Notably the refractive index difference plays an important role in the array formation.

There are further important factors we have to take care off for the error evaluations in the next chapter. For a low Δn , the optical forces acting are weak and the array creation (after loading by the helper tweezers) was observed after a time scale of several seconds before the spheres reached their

equilibrium separations (at $\Delta z = 0$). The low refractive index difference between the spheres and the host medium made an increase of the waiting time between the initiations of the array and measurement necessary due to a longer response time of the array. During measurements a fluctuation in the sphere separation may be caused due to the open sample cell used in the experiment, where a slight flow can perturb the array formation in contrast to the use of closed cells [9]. These and other noise sources such as laser fluctuations (maximal 3% of the output power) and external vibrations were compensated by long integration times of up to 1 minute for each experiment. To account for evaporation of the host medium, which changes the concentration (by $< 4\%$ over the duration of data acquisition equal to 5 minutes) and hence the refractive index, the host medium was washed off after each measurement and new medium and spheres added.

2.5 Conclusion

In this chapter I introduced the experimental setup, a counter-propagating (CP) dual-beam fiber optical trap, to investigate longitudinal optical binding. Key features of the presented fiber trap are a variable separation between the fibers, a combined imaging and helper tweezers setup allowing the trap to be loaded or the array altered. The fiber trap was characterised by measuring the mode field diameter and a comparative study between multi mode and single mode fiber in their ability to trap matter was presented.

During the initial stage of this project I developed a particle tracking program with which it is possible to quantitatively track the position of the optically bound spheres. Importantly this program made it possible to track the fiber separation D_f *in situ*. This versatile feature will be used in the next chapter and is to best of my knowledge not possible with common particle tracking software.

I elucidated via initial experimental investigations of Chinese Hamster Ovary (CHO) cells and dielectric spheres the importance of the refractive index difference Δn between optically bound matter and host solution. The influence of the refractive index difference plays a prominent role in the formation of optically bound matter. Furthermore these experimental findings on the refractive index difference form the basis for the studies conducted in the following chapter. These findings already intuit that optical binding is a complex multiparameter problem and the realm of investigations will be herein

extended.

Although an inexpensive measurement method was generated to determine the refractive index of the host solution by utilizing a re calibrated Brix refractometer. Special care was taken to accurately estimate the refractive index of the sphere to obtain meaningful theoretical results in the following chapters. For a future more accurate method of determining the refractive index one could adapt the approach by Flynn *et al.* [46] where the change in forward scattered light of a trapped particle is used to determine the refractive index in a CP trap.

From these initial investigation I move now on to take a closer look at arrays of two spheres and their separation D to gain a better understanding from the simplest case of optical binding.

Chapter 3

Optical binding of two dielectric spheres

3.1 Introduction

Longitudinal optical binding is in contrast to most common optical tweezers, with predefined trap sites e.g. [24, 47] and standing wave traps [30] where the spheres are spaced by $\lambda/2$, a self mediated system. For an optically bound array (shown in figure 3.1 (top)) the interplay between light and matter creates trapping positions self-consistently where the net force on each sphere is zero.

In such a counter-propagating geometry forces perpendicular to the propagation direction of the two optical fields confine the spheres of the array in the xy -plane. On the other hand forces acting along the propagation direction (z -axis) are most important as they define the optical potential in which the spheres then reside. Two forces oppositely directed along the propagation axis are acting on any one sphere in a two sphere array: One arises from the unperturbed beam (shown in figure 3.1 (bottom) in white), while the second force originates from the diffracted beam (shown in figure 3.1 (bottom) in green) by the spheres nearest neighbour. Wherever those two forces are equal a stable equilibrium separation D is obtained and an array is formed.

Optical binding arises from the fact that the force acting on a given sphere is composed of two components along the z -axis, one from the laser field whose beam waist is closest to the given sphere and a second oppositely directed force arising from the CP laser field that is partly refocused onto the given

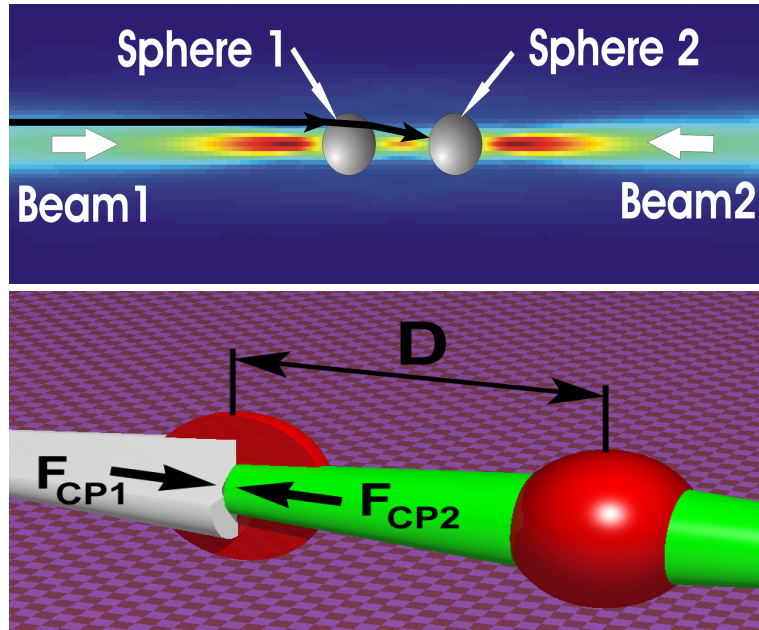


Figure 3.1: Top: The black arrows give an intuitive picture of the diffractive refocussing effect of the sphere (underlaid is a simulated intensity plot of the whole array). Bottom: Two sphere array with two oppositely directed forces acting, the beam (white) emerging from the left hand side exerts a force F_{CP1} on the sphere while the diffracted beam (green) coming from the second sphere exerts a force F_{CP2} . Wherever those two forces are equal a stable equilibrium separation D is obtained and an array is formed.

sphere by the other sphere. Balancing of these two forces by the refocusing of the spheres provides an intuitive explanation of optical binding.

The formation of optically bound arrays is dependent on parameters that determine the interaction between the optical fields and particles and hence the resulting forces, as was indicated in preliminary experiments in the previous chapter. In a counter-propagating geometry the optical fields emerging from the fibers are described by their mode diameters, their separation and intensity. For a symmetric case, where both fields are equal, the emitted intensity is a minor factor [11] as it only scales the magnitude of the acting forces. The mode field diameter is determined in our experiment by the core diameter of the fibre. The only variation of the optical field can be implied by the separation of the fibers and will be part of the investigations conducted in this chapter.

The optical field is perturbed by the presence of the host medium and the spheres, which are distinguished by the refractive index distribution within the optical path. Different materials and sphere sizes alter the optical field distribution, which then creates a distinct equilibrium separation (D) of the

spheres for given field and material parameters.

Intriguingly, the set of the optically bound spheres represents a nonlinear system as the optical field and refractive index distribution are influenced by one another. Such a system can exhibit multi- or bistability for a certain set of parameters and will be part of the investigations in this chapter. This bistability is not due to predefined trapping positions as shown with two lensed fibers in [48]. Bistability in optical binding is possible in the coupled light-sphere system due to feedback: Changing the sphere separation alters the electromagnetic field distribution via the focusing properties of the spheres, which in turn alters the forces on the spheres. Due to this feedback the forces on the spheres viewed as a function of sphere separation can become highly nonlinear, and give rise to bistability.

A numerical model (detailed in Appendix A) was utilised to calculate the counter-propagating fields and the forces in the propagation directions (z-axis) arising on a system of two spheres for a varying separation distance D between them, from two counter-propagating beams. Whenever the sum of forces on one bead from both beams equal zero a possible equilibrium position for the system is obtained, see figure 3.1 (bottom). An example calculation is shown in figure 3.2 (left).

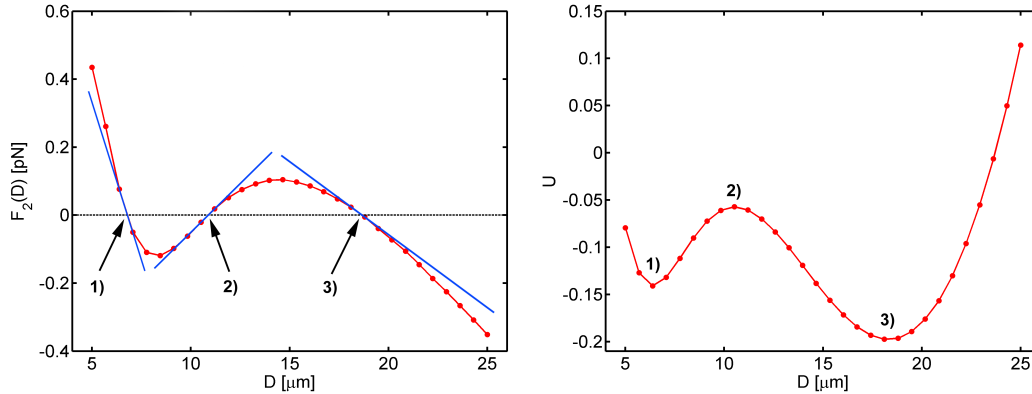


Figure 3.2: For the parameter values chosen in this example the system is observed to have more than one stable equilibrium separation. Left: Plot of the computed force $F(D)$ acting on either sphere (assuming centrosymmetric array formation) versus sphere separation D . Equilibrium separations (D) of the two spheres are found when the force $F = F_{CP1} + F_{CP2}$ is zero. Depending on the sign of the slope (represented by blue lines) through the equilibria they are either stable (negative slope) or unstable (positive slope). Right: Calculated effective potential (U) of the system. The numbers correspond to the stable (1,3) and unstable (2) solutions in both pictures. With parameters of $\lambda = 1070nm$, $n_h = 1.32$, $\Delta n = (n_s - n_h) = 0.09$, $r_{sphere} = 1.5\mu m$ and separation of the CP fields $D_f = 90\mu m$.

By plotting the force $F(D)$ acting on either sphere versus the sphere separa-

tion D we can determine the stability of the solution, stable equilibria having a negative slope, indicating a restoring force.

From the calculated forces we may also numerically determine the effective potential, which will prove useful in intuiting the spheres motion. A sample calculation of the potential is shown in figure 3.2 (right).

Experimentally and theoretically several key parameters will be investigated, for example the refractive index of the host solution was changed between 1.32 and 1.36. This led to simulation of the force dependent on the separation D and the refractive index. In the following sections I will present experimental and theoretical data on the dependence of the center to center separation D between two optically bound silica spheres on key physical parameters. These key parameters are: The waist separation D_f of the two CP light fields, as well as the sphere size and Δn .

3.2 Linear array formation

For an array of two spheres, and a fixed fibre separation D_f , the stable equilibrium sphere separations depends on the refractive index difference Δn between the spheres and host medium. In the first set of experiments the influence of Δn on the array spacing D for $5\mu m$ and $1.28\mu m$ diameter spheres with a fixed fibre spacing of $D_f = 90\mu m$ was explored for a wavelength of $\lambda = 1070nm$ and $w_0 = 3.4\mu m$. The experimental data and comparison with the numerical modelling is shown in figure 3.3.

In addition the theoretical model, described in the appendix section A, is used to predict these stable equilibrium separations.

For $5\mu m$ spheres (left plot in figure 3.3) we find that the equilibrium separation decreases with Δn , whereas for $1.28\mu m$ spheres (right plot in figure 3.3) the equilibrium separation is seen to increase with Δn , both in agreement with the numerical modelling. Furthermore, for the smaller sphere size the numerics predicts a bistable region at around $\Delta n = 0.06$. Experimentally the bistability could not be resolved for this example, but still a trend for the experimental sphere separation D to increase with Δn is evident.

An intuitive picture of the dependence of the equilibrium spacing D on the refractive index difference Δn is as follows: The small angle approximation to the focal length of the spheres [49] is $f = r/(2 * \Delta n)$, which shows that the focal length of the sphere decreases with increasing refractive index difference. Since optical binding arises physically due to the refocusing of the light

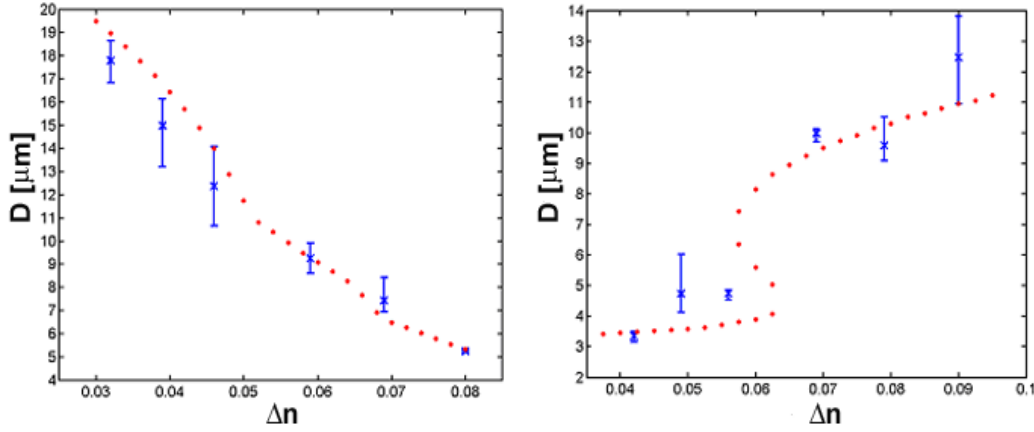


Figure 3.3: Dependence of the equilibrium sphere separation D on the refractive index difference Δn for $5\mu\text{m}$ (left picture) and $1.28\mu\text{m}$ (right picture) silica spheres. The experimental results are shown as blue data points where the errorbars indicate spread of the measurement values for 12 data sets and typically 300 measurements with at least 3 different sphere pairs. Red dots indicate the modelling results.

fields by the two spheres onto each other, the equilibrium sphere separations are expected to follow the same trend as the sphere focal length, namely that it would decrease with increasing Δn . This trend is clearly seen for the $5\mu\text{m}$ diameter spheres (left plot in figure 3.3), but not for the $1.28\mu\text{m}$ diameter spheres (right plot in figure 3.3). A reason for this behaviour will be given in the next section.

3.3 Bistability in optical binding

The second set of experiments was designed to explore the bistability in optical binding, see figure 3.4.

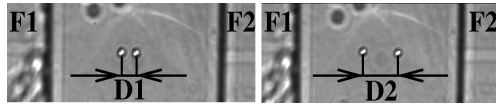


Figure 3.4: The picture shows two images of the observed bistability with different separations $D_1 \approx 8\mu\text{m}$ and $D_2 \approx 19\mu\text{m}$ between the two spheres for constant parameters.

In particular, the stable equilibrium separation D of two $3\mu\text{m}$ diameter silica spheres was measured as a function of the refractive index difference for a fixed fibre separations of $D_f = 70, 90, 100\mu\text{m} \pm 4\%$. The experimental results

are shown in blue in the left hand plots in figure 3.5 a), b) and c) respectively along with the corresponding numerical model results indicated by the red dots. In all of these experimental plots the blue crosses represents the overall mean value for a series of realisations, and the blue vertical bars delineate the spread in measured values. For example, in figure 3.5 b) the overall mean values of the sphere separation was taken over on average 12 data sets of about 300 measurements each with typically 3 different sphere pairs. We see that there is good overall agreement between the experimental results and the stable solutions from the numerical model; the regions of negative slope in the D versus Δn plot being found to be unstable (see figure A.7). In particular, the experiment shows the bistability predicted by the theoretical modelling.

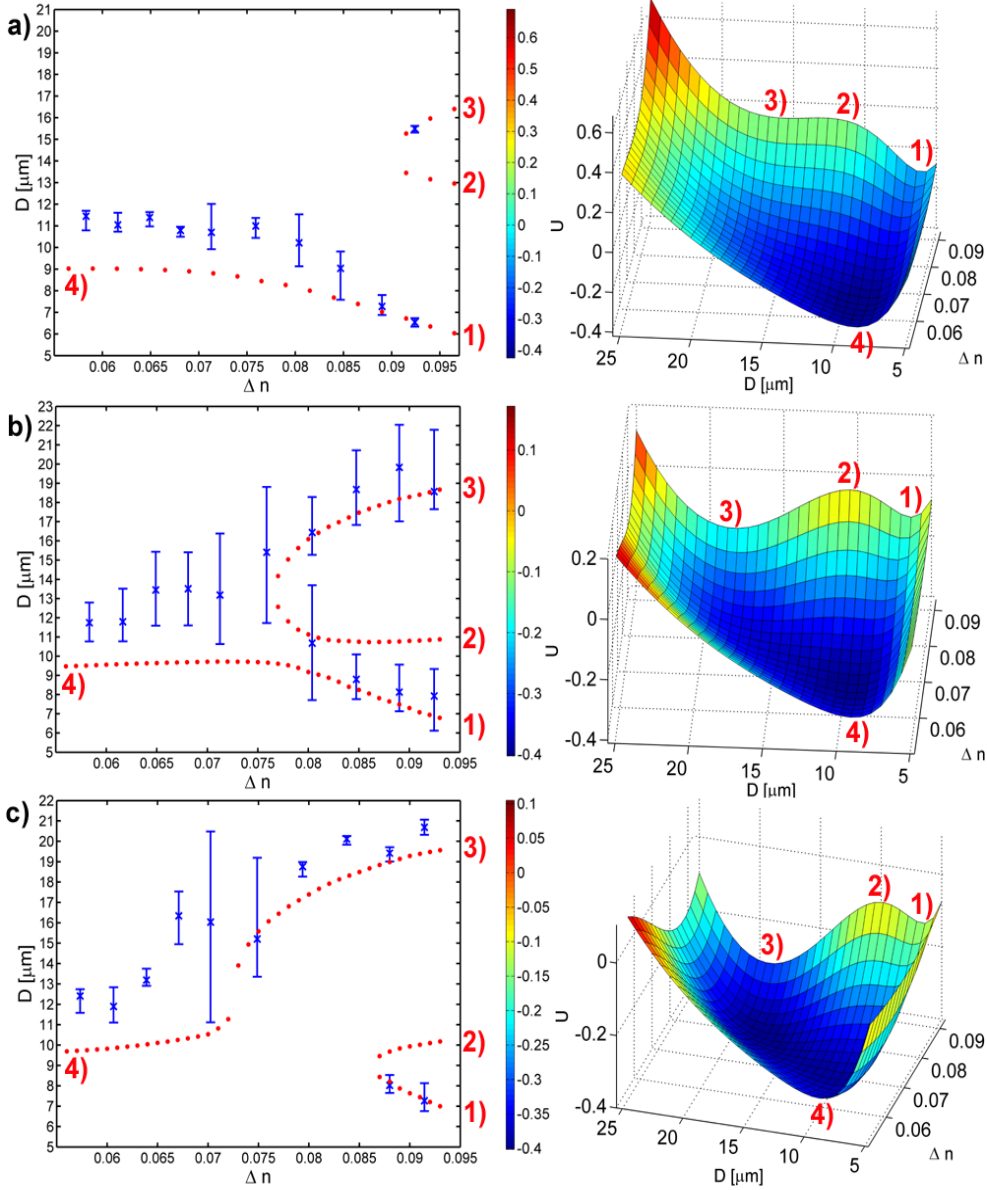


Figure 3.5: Experimental and theoretical results for the bistability in a two sphere system for a fixed fibre separations of $D_f = 70, 90, 100\mu\text{m} \pm 4\%$ corresponding to a), b), c) respectively for a variable index mismatch Δn . On the right the equivalent calculated potential is shown. The numbers indicate corresponding points in the graphs to aid the eye. a) The left hand plot shows the experimental (blue) and theoretical (red) data for the sphere separation D versus refractive index difference Δn for a fibre separation of $D_f = 70\mu\text{m}$. The right hand plot shows the corresponding theoretical plot of the potential U as a function of D and Δn . b) The left hand plot shows the experimental (blue) and theoretical (red) data for the sphere separation D versus refractive index difference Δn for a fibre separation of $D_f = 90\mu\text{m}$. The right hand plot shows the corresponding theoretical plot of the potential U as a function of D and Δn . c) The left hand plot shows the experimental (blue) and theoretical (red) data for the sphere separation D versus refractive index difference Δn for a fibre separation of $D_f = 100\mu\text{m}$. The right hand plot shows the corresponding theoretical plot of the potential U as a function of D and Δn .

For the fibre spacing $D_f = 70$ in figure 3.5 a) we see that the sphere separation hovers around $D = 11\mu m$, and a bifurcation point appears around $\Delta n = 0.09$ beyond which a new stable upper branch appears. This is also seen in the plot of the numerically generated effective potential U which is plotted on the right hand side of figure 3.5 a) as a function of D and Δn . In particular, for $\Delta n = 0.06$ there is a global potential minimum at around $D = 10\mu m$ and marked 4), but for $\Delta n > 0.09$ two potential minima, marked 1) and 3), are evident (along with an unstable potential maximum marked 2)). Furthermore the lower branch, which exists below the bifurcation point, exhibits the expected trend that the sphere separation decreases with increasing Δn .

In contrast, for the fibre spacing $D_f = 90\mu m$ in figure 3.5 b) we see that the bifurcation point is reduced to $\Delta n = 0.077$, and both the upper and lower stable branches are equally evident in the sphere separation and potential plots. In contrary the sphere separation for the lower bistable branch has a tendency to decrease with Δn , the sphere separation for the upper bistable branch has a tendency to increase with Δn . Thus, in the vicinity of bistability of the optical binding the simple argument based on focusing that the sphere separation must decrease with increasing refractive index difference is negated, and this underlies the differences seen for the two cases in figure 3.3 with and without bistability.

As the fibre spacing is further increased to $D_f = 100\mu m$ in figure 3.5 c) we see that the bifurcation point has increased to $\Delta n \approx 0.087$, but in this case it is the lower branch that appears only beyond the bifurcation point (in contrast to the case in figure 3.5 a) for $D_f = 70\mu m$ where it is the upper branch that only appears beyond the bifurcation point). The plot of sphere separation versus refractive index difference is in this case mainly dominated by the upper branch with the trend for D to now increase with Δn .

As expected from the competition of two stable solutions, the experimental fluctuations indicated by the blue vertical bars in figures 3.5 a) to c), are largest closest to the bifurcation points where new bistable branches appear. Furthermore, it is also seen that the deviation between theory and experiment in figures 3.5 a) to c) is largest for smaller values of Δn . This is understood by realising that as the index mismatch decreases the net optical forces acting on the spheres also get smaller, so the equilibria are created by cancellation of ever smaller forces due to the CP fields. In this situation the numerical equilibria become more and more sensitive to the precise material parameters, whereas for larger index mismatches the equilibria are more ro-

bust against slight parameter variations.

This is due to two effects: first by raising the refractive index the respective forces on the sphere are getting smaller, figure 3.6 (right). More importantly the forces on the two beads follow equilibrium over a wider range of separation distances between them figure 3.6 (left).

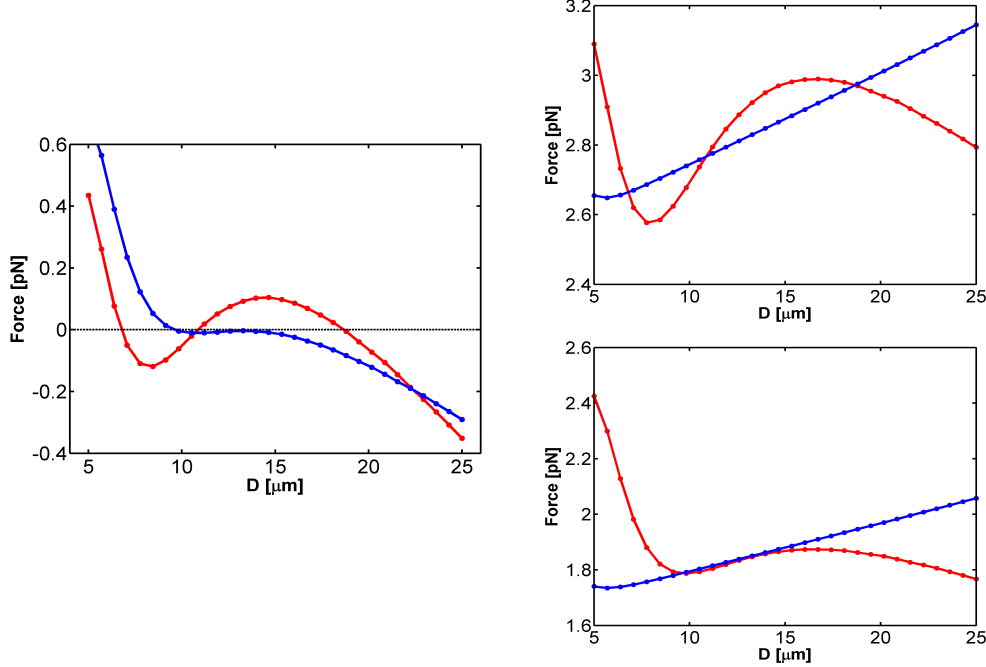


Figure 3.6: Left: Force acting on the spheres for different separations D between them (with a fibre separation of $90\mu m$). The red graph shows three solutions for a refractive index mismatch of Δn about 0.09 the bistability point. The blue graph shows the simulation for $\Delta n = 0.07$ the point of bifurcation, here solutions can appear between 10 to $15\mu m$. As the forces are almost equal over a large range of separations of the spheres. The individual forces are shown on the right. Right (top): $\Delta n = 0.09$ The individual forces on one sphere are shown; blue, the force evolving from the unperturbed field and red from the diffracted field. Right (bottom): same as above for $\Delta n = 0.07$. Importantly the acting individual forces have decreased by $\approx 40\%$ from about $3pN$ to $1.8pN$ by lowering the refractive index difference.

At the bifurcation point ($\Delta n = 0.07$) there is a zero transition at $D = 10\mu m$ as shown in figure 3.6(left - blue graph). However it is not as distinct as for the bifurcation point (at $\Delta n = 0.09$) and over a sphere separation range $10 - 15\mu m$ the forces from both CP fields are almost equal.

Consequently in the experiment slight differences in refractive index of the spheres and the host medium and their size can produce experimental results anywhere in this regime, even for long integration times of up to 1 minute.

This can also be seen if the potential plots are compared. Especially for a

fibre separation of $100\mu m$ a large area of the potential (shown in figure 3.5 c)) is quite shallow (dark blue area). Experimentally solutions can occur anywhere as the optical potential has no strong gradient over a wide area. Thus the observed measurement spread is dependent on fluctuation in sphere parameters which are captured by measuring different arrays and averaging over these results.

To elucidate the sensitivity, I will evaluate theoretically slight changes in sphere parameters for a refractive index difference of $\Delta n = 0.09$.

By changing only the refractive index of both spheres by $+0.3\%$ a shift for the first stable solution of -8.2% is obtained, the second stable solution shifts by $+2.1\%$ while the unstable solution shifts by $+2.6\%$.

Varying only the sphere diameter by $+3.3\%$ (Bangs laboratories gives the STD of the mean diameter $3\mu m$ to $<10\%$) causes the first stable solution to shift by -4% and the second only by -0.1% , while the unstable solution changes by -15.5% .

Also slight changes of the host refractive index can shift the simulations¹. For $+0.3\%$ the first solution shifts by $+17.8\%$ and the second stable solution by -2.8% while the unstable solution is shifted by -5% .

The fibre separation can induce shifts in the data (as the system had to be re-setup for each measurement step of Δn). Where an error of $+1\%$ shifts the first stable position by $+3\%$, the second stable position is shifted by $+0.2\%$ and the unstable position is shifted by -0.4% .

The interplay of these parameters can change the agreement of theory and experiment significantly. However to achieve consistent results material parameters were left constant for all simulations to obtain comparable results. Additionally the trapping forces acting on the spheres influence the spread of the measurements. For lower Δn values all forces acting on the spheres are reduced in magnitude making them more susceptible to perturbations (e.g. slight flow within the open sample cell). This in turn produces a wider spread of the experimental data within the accessible theoretical regime in which the forces are following close to each other.

A closed sample cell [9] would overcome these limitations: however such an enclosed design was not realised as it would have not permitted us to *in situ* vary the fibre separation D_f .

In the experiment these sensitivities add up and induce the relative large

¹In an evaporation experiment the concentration of the host medium was found to change by 5% over a duration of 5 minutes.

measurement spread. Nevertheless, there is a very good correlation between the numerical graphs and experiments and excellent evidence for bistability.

3.4 Hysteresis

Hysteresis between two solutions is inherently linked to a nonlinear system when one key variable is cycled and thus should be observable in bistable optical binding.

As indicated by the numerical simulations and experimental findings, the potential landscape of the bistability is strongly dependent on the fibre separation. In particular, the observed bistability in optical binding suggests that hysteresis in optical binding could be observed if the fibre separation was slowly cycled in the bistable regime so that the sphere separation would follow adiabatically its local stable equilibrium value.

Here I will elucidate this dependence on the fibre separation more clearly. The following sequence shows the evolution of the potential for different fibre separations while leaving the potential axis (U) constant, figure 3.7.

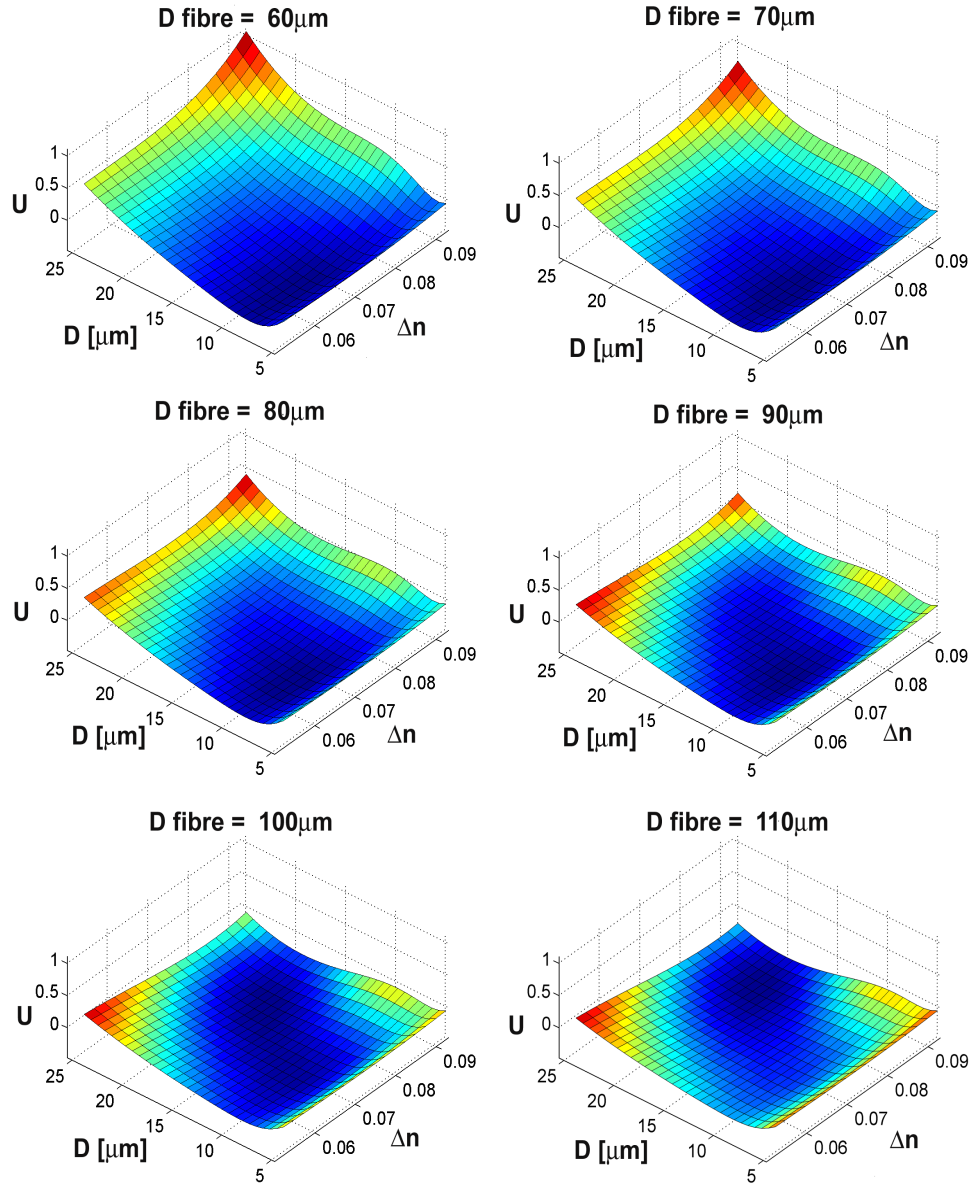


Figure 3.7: Tilting of the optical potential map by varying the fibre separation D_f . The optical potential is getting tilted and only marginally reformed so the main structure of the potential is preserved. Top left to bottom right for fibre separations ranging from 60 to 110 μm in 10 μm steps.

As shown in figure 3.7, when the fibre separation is de- or increased the potential becomes more tilted rather than reformed. In such a tilting potential landscape one would expect that the sphere separation follows the underlying local minima, rather than the global minima, like a marble on a structured game board with mountains and valleys. Thus a hysteresis loop should be traced out when the fibre separation is cycled .

3.5 Experimental observation of hysteresis

For this experiment the separation between the fibre ends was slowly cycled with a stepper motor from $140\mu m$ to $40\mu m$ and back to $140\mu m$.

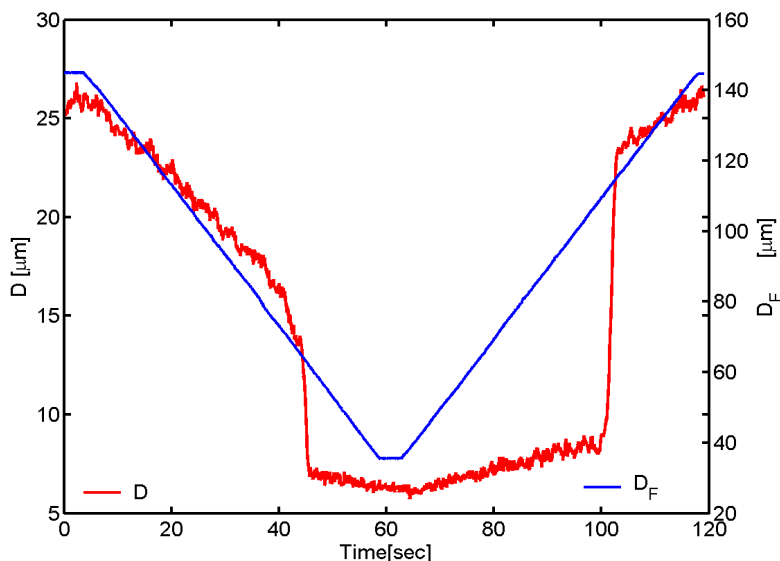


Figure 3.8: Variation of the fibre separation plotted against the number of frames. Red, shows the variation in sphere separation and blue indicates the movement of the fibre.

For a relatively slow cycle velocity of the fibre ends, $1\mu m/sec$, the spheres were experimentally found to adiabatically follow the changing fibre separation in the system and hysteresis was observed. This is shown as the blue data in figure 3.9 (left plot) for which the experimentally measured sphere separation D is plotted parametrically as a function of the fibre separation D_f .

The red data in figure 3.9 (left plot) shows the theoretical sphere separation

as a function of fibre separation, and there is excellent overall agreement between the theoretical calculations and experiment. The agreement is best for

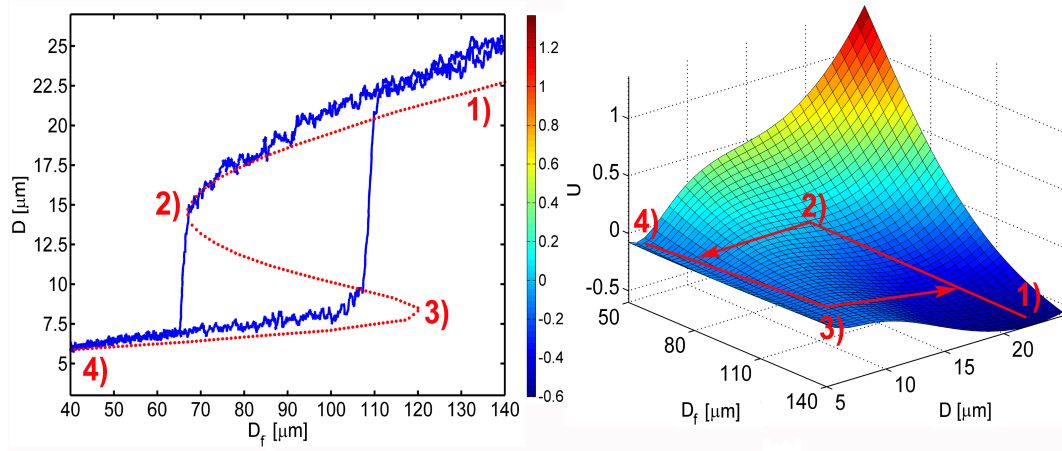


Figure 3.9: Left: Equilibrium sphere separation D plotted parametrically as a function of the fibre spacing D_{fibre} from experiment (blue data) and theory (red data). Right: Corresponding effective potential U as a function of sphere spacing D and fibre spacing D_{fibre} . The numbers are analogous in both graphs to aid the eye. 1) corresponds to the start and end point of the full hysteresis cycle, 2) is the lower switch point 3) is the point at which the cycle is reversed and 4) is the upper switch point.

smaller fibre separations but dwindles for larger separations. The explanation for this is that for large fibre separations the magnitude of the cancelling optical forces acting on the spheres is getting ever smaller. This means that vibrations and imperfections in the system, can play a bigger role if they are at the same order of magnitude, and deviations between theory and experiment are not unexpected.

To put this in context, the Rayleigh range for the fields emitted by the fibers is around $30\mu m$ so that for a fibre separation of $100\mu m$ the fields are considerably reduced in intensity compared to the input. Thus, at the upper switching point we see that the system switches early, which can be attributed to enhanced sensitivity to external perturbations and noise around the switching point. In particular, the data is clearly noisier on the upper branch for fibre separations between $D_f = 110 - 140\mu m$ in comparison to the lower branch for fibre separations between $D_f = 40 - 60\mu m$.

The detailed numerical hysteresis loop is sensitive to the parameters used, in particular the upper switching point can change by many microns with a small change in refractive index.

Also if the fibre spacing is changed too quickly the hysteresis loop be-

comes washed out and eventually vanishes. This is illustrated in figure 3.10 (left) where the experimentally measured sphere separation is parametrically plotted as a function of fibre separation for velocities $v_{black} = 30\mu\text{m}/\text{sec}$, $v_{blue} = 10\mu\text{m}/\text{sec}$, and $v_{red} = 4\mu\text{m}/\text{sec}$, as D_f is cycled between $40\mu\text{m}$ to $130\mu\text{m}$. If the speed is reduced to $v_{red} = 2\mu\text{m}/\text{sec}$, as in the right plot in figure 3.10, the hysteresis was observed to extend to $130\mu\text{m}$, close to the theoretical value in figure 3.9. Material sensitivities are also reflected in the

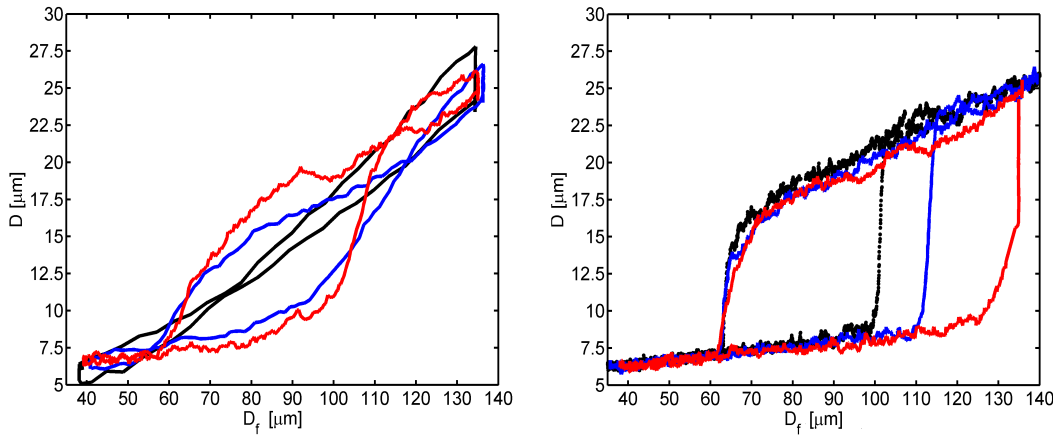


Figure 3.10: Left: If the fibre speed is set too high the hysteresis loop washes out ($v_{black} = 30\mu\text{m}/\text{sec}$; $v_{blue} = 10\mu\text{m}/\text{sec}$; $v_{red} = 4\mu\text{m}/\text{sec}$). Right: With a speed of $v_{red} = 2\mu\text{m}/\text{sec}$ the hysteresis was observed to extend to $130\mu\text{m}$. If the hysteresis loop is repeated several times with the same sphere pair, results for the upper switching point between 100 and $110\mu\text{m}$ were obtained (black and blue showing only the extremes of these measurements) with $v_{black} = v_{blue} = 1\mu\text{m}/\text{sec}$.

experimental observations, where the hysteresis loop for different pairs of spheres can vary in a way not fully accounted for by the nominal size and refractive index differences within one batch.

In a follow up experiment I investigated the dependence of the switching point when the material parameters are left constant, figure 3.10 (right). By considering only one sphere pair and reiterating the hysteresis loop 4 times the observed maximum deviation (other results are not shown) of the upper switching point is between 100 and $110\mu\text{m}$ (see figure 3.10 (right) black and blue line). In one extreme case for a different sphere pair the upper switching extended to $130\mu\text{m}$ (this result was taken for a higher fibre variation speed of $2\mu\text{m}/\text{sec}$, shown in the red curve, figure 3.10 (right)).

It should be noted that the lower switching point at $\approx 60\mu\text{m}$ is more robust and is reproducibly observed in the experiments at this fibre separation.

However, even with a fixed sphere pair and fibre velocity, the upper switching point in the bistable loop can vary from shot to shot, this is shown in the blue and black curves in figure 3.10 (right). Such shot to shot variations are clearly largest at the vicinity of switching points, where the effective potential U is flat and the forces are close to zero. Here the system is more susceptible to the effects of noise, which then initiates the transition. Figure 3.9 (right) shows U as a function of sphere spacing D and fibre spacing D_f , at the upper switch point $D_f \approx 110\mu m$ the potential is relatively flat as a function of D . In contrast, near the switch down point $D_f \approx 60\mu m$ the potential has much more structure as a function of D , and it is expected that the switch down dynamics should be much more robust as seen in the experiments. Theoretically this extension of the hysteresis loop at the upper switch point is captured with an increased resolution of the spheres in the code (shown in figure 3.11). In these simulations the slab number was increased and the propagation steps within each slab increased as well. Due to the increase of computation time, fewer points on the hysteresis were calculated.

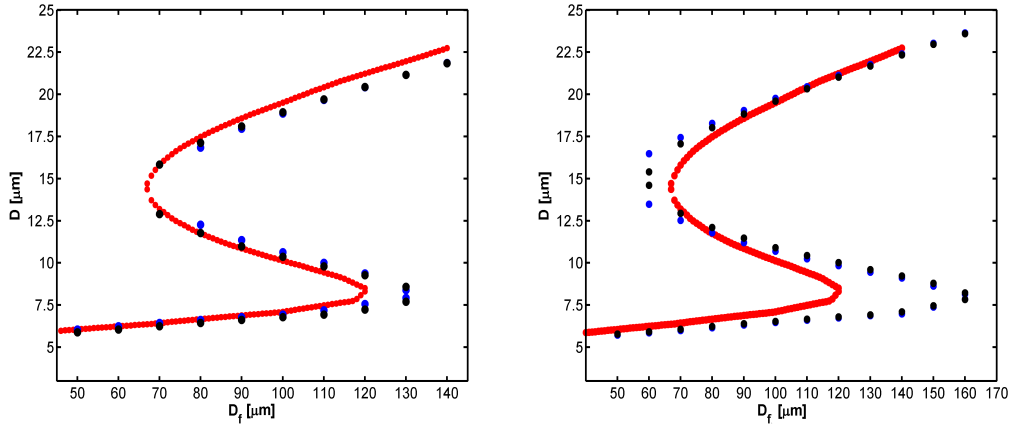


Figure 3.11: Left: 3 step propagation within one slab and the whole sphere being modelled with a slab number of 26 (blue) and 50 (black). Right: 6 step propagation within one slab and the sphere being approximated with a total slab number of 44 (black) and 60 (blue). For comparison the original theoretical simulation is shown in both graphs in red.

Nonetheless, this demonstrates that the numerics converge for a higher resolution and that hysteresis can occur in optical binding. The model predicts that the sphere equilibria should be independent of power, which is confirmed in the experiments over a range of $60mW$ to $200mW$ from each fibre. At the lowest powers the system is far noisier, as

mechanical vibrations, evaporative flow in the open sample cell, and other external perturbations are more able to induce premature transition between the stable branches, or even cause a total loss of the particles from the trap, at large fibre separations .

For this reason, the experiment shown in figure 3.9 and 3.10 were performed at the relatively high power of $200mW$, allowing the access to data at very large fibre separations. The other experiments were performed at no more than half this power. At high enough powers one would expect that heating effects (convective currents) ought to interfere with the predicted behaviours. Nevertheless, over a significant range of powers, it is observe that the equilibrium positions remain fixed.

3.6 Conclusion

Refocusing of the counter-propagating fields by the spheres does indeed provide an intuitive picture of the observed optical binding. In this section I presented the first experimental and numerical data for the dependency of the binding of two spheres as a function of the refractive index mismatch and the dependency upon fibre separation. The system of two bound spheres maybe readily used as a sensitive refractive index measurement method for spheres or the host medium. Provided that either two refractive index out of three (n_{host} , $n_{sphere1}$ and $n_{sphere2}$) in the system are known to sufficient accuracy. Bistability may readily be observed with judicious choice of fibre separation. Physically, bistability can occur in optical binding as the light is modified 'refocused' by the spheres and the light in turn tells the spheres how to move, thus optically bound matter is a nonlinear phenomena. It is this feedback that allows the force acting on the spheres viewed as a function of sphere separation to become nonlinear and to display several zero crossings, hence to show bistability.

Importantly I was able to show that hysteresis can occur in optical binding and give further evidence that optical binding can be viewed as a nonlinear system.

The model is applicable directly to sphere sizes in the Mie and Lornetz-Mie regime and shows good agreement with the experiment. For this reason smaller sphere sizes were not considered here, as Rayleigh scattering would be dominant and the model would be expected to fail. Furthermore it should be noted that the paraxial approach used for the model limits its applicabil-

ity to low refractive index differences. Both limitations of the model are in more depth elucidated in the appendix section A.2

Importantly bistability as well as optical binding is not limited to two spheres. Higher order arrays have been observed before [17, 11]. Interestingly three $3\mu\text{m}$ spheres were observed to exhibit bistability, see figure 3.12.

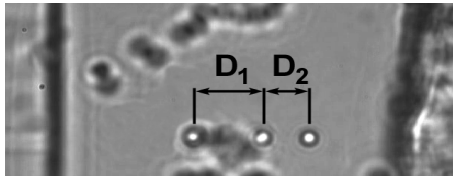


Figure 3.12: Three $3\mu\text{m}$ spheres with two different distances between the spheres of $D_1 = 12\mu\text{m}$ and $D_2 = 8\mu\text{m}$ at a fibre separation $D_f = 60\mu\text{m}$ at $\Delta n = 0.08$.

Here the symmetry of the array around $D_f/2$ used to calculate increasing array separations (as described in A.5.3) cannot be exploited anymore and therefore the computation time is increased significantly, as every sphere has to be varied individually and the force from both fields calculated.

Similar to higher order linear arrays (for $N > 3$): For example in a four sphere array ($N = 4$) one needs to alter the sphere separation of the two central spheres stepwise and scan for every step the two outer spheres. This represent computationally a formidable challenge and was not attempted. Furthermore experimentally there are issues to consider for such higher order arrays: Higher order arrays are readily observed for small sphere sizes ($r_{\text{sphere}} < 0.5\mu\text{m}$), where we are at the boarder to the Rayleigh regime and the model is expected to start to fail for such small sphere sizes. Alternatively one could use bigger particles which are not observed to exhibit binding for large refractive index differences and therefore need to be in a sucrose solution to decreased the refractive index mismatch. These observations are in contrast to [17] where higher order arrays were observed without changing the refractive index and for large sphere radiuses, this could be attributed to the bigger waist size (w_0) used in the experimental setup. Intriguingly one of the key questions of investigation is, are such higher order arrays regularly spaced or irregularly.

Furthermore the bistable potential opens up the possibility to study thermally induced transitions in adjacent potential minimas (see figure 3.2 (left)) [50] in the realm of optical binding, here the thermal energy must be large enough for the particles to overcome the potential barrier (marked 3) in figure 3.2 (left)). Here however it might be cumbersome to find the exact system

parameters for which those minimas are the same, otherwise the spheres might reside in the global minimum and only one transition to the lowest potential is observed.

Optical binding is in many respects in its infancy and likely will play a pivotal role in self assembly of small crystalline structures using optical forces. Although refocusing of the light fields by the bound matter can yield an initial explanation for longitudinal optical binding in the Mie regime it fails to explain the response of the array spacing (D) in the bistable regime to a varying refractive index mismatch (Δn). Therefore this underlying phenomenon will be investigated in more detail in the next chapter.

Chapter 4

Visualisation of the field distribution in optical binding

In the following chapter I will describe an experimental technique for the *in situ* visualisation of the field redistribution which occurs during optical binding. This is achieved through the novel application of a dual beam fibre trap incorporating a pulsed femtosecond laser source.

The trap operates in an environment with a fluorescent dye added to the host medium. Two-photon excitation of the dye by the ultrashort pulse laser [51, 52] used as the trapping light permits us to map the light redistribution around each trapped microparticle. Thus it is possible to observe the binding process in real time and compare it with numerical simulations of the field distribution. Firstly, I want to discuss the extension of the numerical model that underpins the experimental observations.

4.1 Theoretical model extension

The theoretical model comprises of either one single or two counter-propagating (CP) laser fields of wavelength λ aligned along the propagation axis z , which originate from one or two single mode fibers with ends located at $z = 0$ and $z = D_f$, (D_f being the fibre spacing for the CP case) which are being modelled as collimated Gaussian beams of waist size w_0 and power P . They interact with dielectric silica spheres of refractive index n_s , diameter D , with the centres located at positions $z_j, j = 1, 2, \dots, N$ and immersed in a host medium of refractive index n_h . In this section the main interest is in the

field distributions involved in optical binding as opposed to the self-consistent determination of the microparticle spacings, so the positions of the sphere centres are taken as input parameters from the experiment for the cases of both optical binding or by a helper optical tweezers with its axis aligned orthogonal to the z-axis. Applying the paraxial wave theory, described in the theoretical model chapter, the evolution of the optical fields distorted by a varying number of spheres N is calculated.

To obtain the intensity distribution the field is modelled as pillboxes [18] of dimensions $350 \times 350 \times 120nm$ in x,y,z respectively, for the experimentally determined sphere positions z_j . The field intensity follows from calculations of ϵ_+ and ϵ_- for the CP case (with ϵ_- being disused for a single beam) where both beams are assumed to be incoherent to:

$$I_{field}(x, y, z) = |\epsilon_+(x, y, z)|^2 + |\epsilon_-(x, y, z)|^2 \quad (4.1)$$

I_{field} = Field intensity
 ϵ_{\pm} = CP fields

A stepsize of $100nm$ in z was used to calculate the field in a plane at $nx/2$, ny in the propagation direction ($nx = ny = 257$ is the grid size of the pillboxes, $nx/2$ donates the centreline at $x(i)$ where $i = 129$). In the experiment the detected quantity is the two-photon fluorescence signal from the fluorescein as imaged and collected along the x-axis. The experimentally detected two-photon fluorescence signal, adapted from [53], is proportional to

$$I_{two-photon}(y, z) \propto A * \int I_{field}^2(x, y, z) dx + C \quad (4.2)$$

I_{field} = Field intensity
 $S_{two-photon}(y, z)$ = Observed CCD signal
 $A \& C$ = Scaling factors

and is used to compare the predicted fluorescence profiles from the numerical simulations with the experimental measurements. Although the model cannot predict the absolute magnitude of the fluorescence signal, comparing the observed and numerical spatial profiles of the fluorescence provides information on the beam diffraction.

The calculated fluorescence intensity distribution is shown as a false colour plot with the maximum field strength being normalised to the colour red. For a more precise comparison between model and experiment the respective centreline intensity distribution were taken. A and C in equation 4.2 are linear correction factors to compensate for contrast and brightness fluctuations from the experimental images.

4.2 Experimental setup

The dual-beam fibre optical trap was slightly modified for the subsequent experimental studies in this chapter. A titanium-sapphire (Ti:Sa) femtosecond laser at a central wavelength of $\lambda = 800nm$ (p-polarised) with $95fs$ output pulses at a repetition rate of $80MHz$, average power $\sim 1W$ (pulse energy of $12.5nJ$, $131kW$ peak power), was used to operate the fibre trap. The light was coupled into two single mode fibers (Thorlabs 780HP for 780 to $970nm$; mode field diameter $w_0 = 5.0 \pm 0.5\mu m$ at $850nm$; Numerical Aperture 0.13 ; Attenuation $< 3.5dB/km$ at $850nm$) via a $\lambda/2$ plate and a polarising beam splitter. The optical power emerging from each fibre could be adjusted with the neutral density filters to ensure equal field distribution of $40mW$ (see figure 4.1).

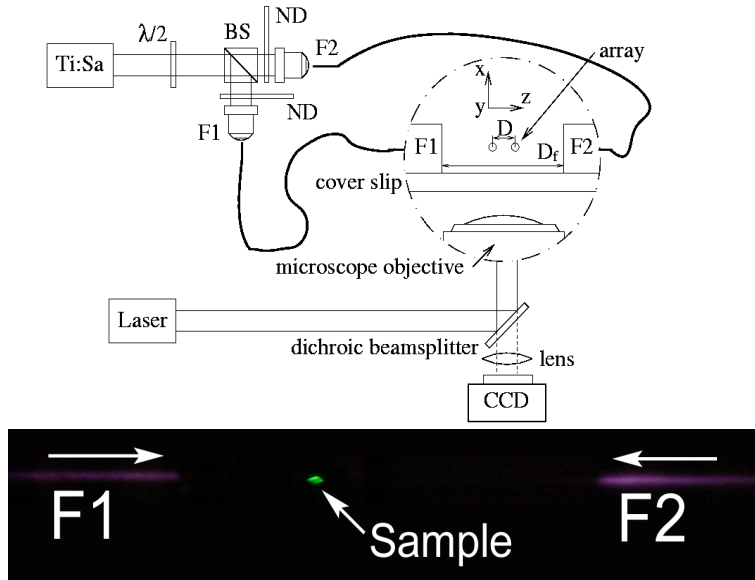


Figure 4.1: Fibre optical trap setup: Light at $800nm$ from a Ti:Sa femtosecond laser is coupled via ND filters into fibre F1 and F2 to ensure equal power distribution. Inset shows fibre trap side view: The array is formed in the gap between the two fibers (F1 and F2) with D being the separation of the spheres and D_f the fibre separation. A second helper tweezers is coupled into the observation microscope via a dichroic beam splitter to hold a sphere in the beam or to initiate the array. Images were taken through the microscope via the CCD camera in front of which a lens could be flipped to achieve varying image magnification. The lower image shows a photo of the sample area - clearly the two fibers can be seen to the left and right with the excitation light (violet-red) leaking out. The sample itself can be seen in the middle (marked with arrow) emitting green light, due to the two-photon fluorescence.

By choosing the optical path difference ($5cm$) of the CP beams larger than the laser coherence length (calculated pulsed laser coherence length $< 50\mu m$),

standing wave effects [30] were avoided. Similar to the previous experiment one fibre (F1) was mounted on a cover slip which was in a fixed position above the imaging setup, the second fibre (F2) was mounted on a XYZ stage and could be aligned with F1 much like in a fibre to fibre pig tailing setup (D_f being distance between the two fibre ends as shown in the inset in figure 4.1). A separate ytterbium fibre laser (IPG Photonics) at $\lambda = 1070nm$ was introduced into the sample chamber orthogonal to the beams creating the fibre trap. This beam was tightly focused via a microscope objective and created a separate helper optical tweezers that permitted loading and manipulation of the optically bound array [11].

The imaging system consisted of a $100\times$ long working distance microscope objective (Mitutoyo) or alternatively a $60\times$ microscope (Newport) and a CCD camera (Watec WAT 902DM2S), which was connected to a computer with frame grabber card to capture the images. In the data presented, the microscopic field of view for the $100\times$ objective was not always sufficient to get an image showing the field distribution in the array and both fibre ends at the same time. To ensure experimental data was acquired when the array center was at $D_f/2$, and thereby assuring a centro-symmetric intensity distribution, a lens was flipped in front of the CCD camera and the power distribution readjusted via the $\lambda/2$ plate when necessary. A short pass filter was used to block out both trapping and tweezing wavelengths and solely pass the two-photon excitation light. The experiment was illuminated from above the cover slip and could be switched off to capture the two-photon images. Data analysis of these images was performed by the LabVIEW script described earlier, to determine the positions of the beads. A similar script was used to obtain the line profile of the fluorescence intensity distribution as well as the experimental false colour images from the grey scale two-photon image which are shown in the following figures but are not to scale.

By utilising two-photon fluorescence I solely want to focus on the redistribution of the optical field pertinent for optical binding. For the experimental data presented here I exclusively consider a single frame of a measurement thereby neglecting the associated spread of the separation due to experimental and material imperfections, which can have an influence on the sphere separation and can induce experimental deviations, as shown in the previous chapter, in the sphere separation and therefore have a strong influence in the exact modelling of the optical field. By considering a single experimental measurement of the sphere separations it is possible to overcome this and achieve good qualitative agreement between experiment and theoretical

model.

4.3 Dispersion

Next I want to consider the pertinent parameters for the first demonstration of the femtosecond fibre trap. To date most optical trapping experiments have incorporated continuous wave laser sources. Standard single beam traps have used femtosecond sources recently for simultaneous trapping and nonlinear excitation [54]. When considering the femtosecond fibre trap, group velocity dispersion (GVD) [55] and nonlinear optical effects such as self phase modulation (SPM) [55] become an issue as they alter the pulse duration. In the experiment the fibre length was between 30cm and 40cm to keep these effects at a minimum.

To compare the change in pulse duration, I measured the pulse via intensity autocorrelation prior to and subsequent to propagation in a 375mm length of fibre, for an input pulse of 95fs increased to 800fs after the fibre thus showing the dramatic effects of dispersion. Before the fibre the spectrum is of Gaussian shape, after the fibre the spectrum broadened significantly due to nonlinear optic effects by a factor of approximately 2.6, see figure 4.2.

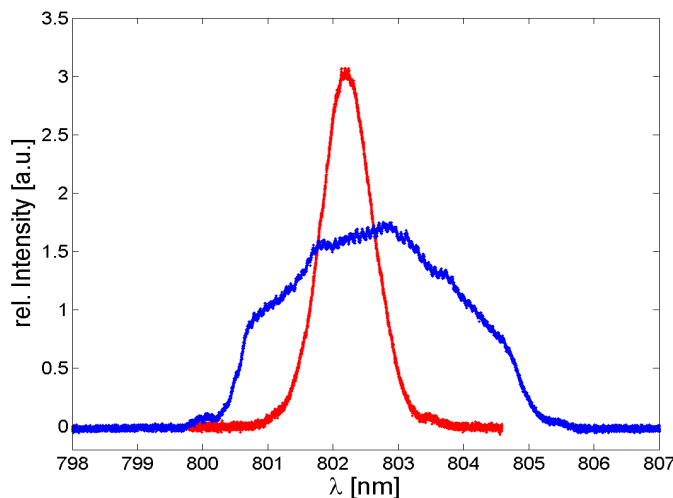


Figure 4.2: An input pulse of 95fs duration increased to 800fs after propagating in 375mm length of fibre thus showing the dramatic effects of GVD. Before the fibre the spectrum is of Gaussian shape (red), and after the fibre (blue) the spectrum broadened significantly by a factor of approximately 2.6 due to SPM.

The spectrum is not broad enough to excite one photon fluorescence in the fluorescein, which can be observed in a supercontinuum [53].

Although the pulse duration and spectrum were increased, a two-photon fluorescence signal was still readily observed from the dye within the sample medium, indicating that the average intensity of $40mW$ after the fibre, which corresponds to a pulse energy of $0.5nJ$ and pulse peak power of $0.6kW$, are still sufficient to obtain two-photon fluorescence. A comparative measurement with a $30mm$ shorter fibre showed no significant change in pulse duration and spectrum. It should be noted that nonlinear processes occur approximately within the first few mm of fibre [56, 55]. However with a fibre length exceeding $60cm$ a two-photon fluorescence signal was not obtained as GVD is present over the whole length of the fibre.

4.4 Two-photon excitation

The host medium for the microparticles was prepared following the studies in the previous chapter; a de-ionised water and sucrose mixture is used to produce a variable host refractive index, and fluorescein (broad excitation band centred around $480nm$ and emission band centred around $530nm$) was added to the sample [51, 52] with a relatively high concentration of approximately $150\pm 30mg/l$, since our peak pulse power is relatively low compared to that of Ref. [57]. Adding fluorescein to the host medium did not change its refractive index. It is known that fluorescein marker concentration fluctuations can lead to linear deviations [57] in the observed two-photon signal between experimental realisations. Also, excitation power variations, due to laser fluctuations between measurements and readjustments to the field distribution to center the array via the $\lambda/2$ plate, have a quadratic influence [58, 59] on the observed two-photon signal. Since the power fluctuations were small ($< 5\%$), induced deviations were therefore approximated as linear. It is important to note that the model does not account for the experimental changes in the two-photon signal due to the variations in marker concentration and excitation power. However, since the theory cannot fix the absolute fluorescence signal strengths, the numerical results were linearly scaled via factors A and C in formula 4.2, to allow for comparison of the spatial profiles of the fluorescence. Furthermore these fluctuations did not influence the array formation as it is independent of power [11] as they apply to both beams accordingly. When the Ti:Sa laser was operated in the continuous-wave (cw)

regime no signal was detected by the CCD camera and this is interpreted as evidence for two-photon excitation in the experiment¹.

4.5 Visualisation of the light redistribution in optical binding

Now I will move on to discuss the visualisation of the optical binding and its accompanying light intensity redistribution. As a first step, light is permitted solely to enter one of the fibers and the helper tweezers is used to hold a single microsphere ($N = 1$) in the path of the single laser field. The $5.17\mu\text{m}$ silica sphere is scanned through the emerging field and the observed light pattern is compared with a simulation. The image sequence (upper part of figure 4.3, images 1) to 6)) shows good agreement with the experiment and similar simulations conducted in Ref.[60]. When the bead is not fully centred light is diffracted away from the beam path creating a cone of low intensity light emerging from the rim of the bead, which is shown in a transverse line profile plot from a to b along the y-axis in figure 4.3 (right).

¹The two-photon process can be readily observed by eye - the photo of the sample cell figure 4.1 shows nicely the excitation and emission colours.

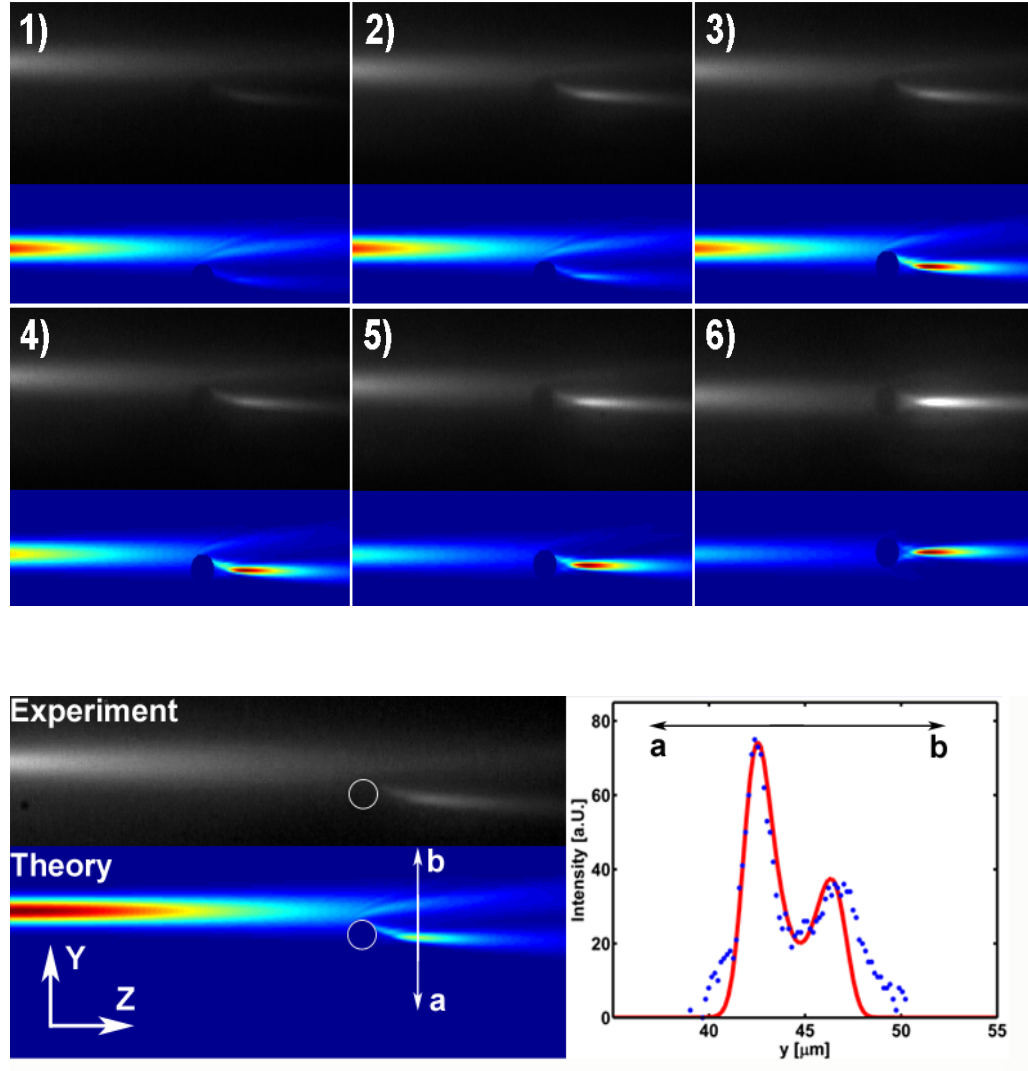


Figure 4.3: Top: 1) to 6) image sequence showing a $5.17\mu\text{m}$ silica sphere being scanned into the beam path. Black and white images show the experiment, the false colour images show the corresponding theoretical simulations. Bottom: Diffraction pattern of a $5.17\mu\text{m}$ silica sphere being offset along the y-axis by an optical tweezers. The sphere position (overlaid white circle) is at approximately $50 \pm 1\mu\text{m}$ from the beam waist. The insert on the right shows the intensity distribution along the y-axis from a to b at $8 \pm 1\mu\text{m}$ after the sphere which has an offset from the beam axis of $3 \pm 0.5\mu\text{m}$ (experiment: blue dots; theory: red line). Light is diffracted away from the beam path creating a valley of low intensity light at the beam axis.

To calibrate the model to the fluorescence intensity the center line intensity distribution was extracted from an image of the optical field emerging from the single mode fibre (modefield diameter $5.0 \pm 0.5 \mu\text{m}$ at 850nm) and compared to the theoretical simulations of an unperturbed field in water², shown in figure 4.4 A). At a propagation distance (z) of $55 \mu\text{m}$ the optical field of the 800nm excitation wavelength has decayed beyond the excitation threshold of the fluorescein. At this point theory and experiment start to disagree, but very good agreement for over $50 \mu\text{m}$ from the fibre output is observed. This disagreement is not observed in all experiments as an equal power distribution in all experiments was not feasible (as this is dependent on the average laser power) as well as concentration variation of the dye sucrose solution can have an significant impact in the cut off behaviour of the observed signal.

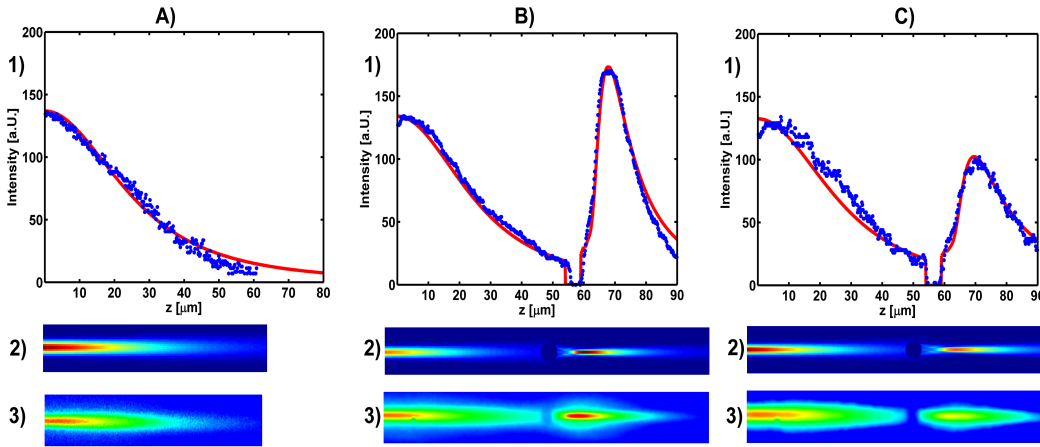


Figure 4.4: A) Single beam emerging from the fibre without sphere 1) On-axis or centreline intensity distribution (red dots - experimental data; blue line - theoretical prediction). 2) Theoretical simulation. 3) Experimental observation. Diffraction pattern of a $5.17 \mu\text{m}$ silica sphere held by an optical tweezers at $54 \pm 1 \mu\text{m}$ from the beamwaist in a single beam originating from the left side of the images. Comparison between different refractive index differences: B) $\Delta n = 0.07$. 1) Centreline intensity distribution (dots: experimental data; line: theoretical prediction). 2) Theoretical simulation of diffraction pattern. 3) False colour images of two-photon fluorescence. C) $\Delta n = 0.05$. 1) Centreline intensity. 2) Theoretical simulation. 3) False colour images of two-photon fluorescence.

To elucidate the influence of the refractive index difference between the sphere and the host medium on the results in figure 4.4 a comparison of a single $5.17 \mu\text{m}$ diameter sphere diffracting the fibre output beam path at a distance

²Measurements of the refractive index of water without fluorescein showed no difference.

of $54 \pm 1\mu m$ from the beam waist for B) $\Delta n = 0.07$, and C) $\Delta n = 0.05$ ³ is presented.

For each example plot 4.4 shows a comparison of the experimental and numerical on-axis fluorescence signals ($y = 0$), whereas plots 2 and 3 show the numerical and experimental fluorescence profiles over the yz -plane, respectively. This numerical labelling of the plots is used in all subsequent plots. These results show that the higher the refractive index difference the more the light is refocused after the sphere, as expected intuitively, and this observation is at the heart of the interpretation of how optical binding works, at least in the Mie size regime considered here. More specifically, the focusing length of the sphere in the small-angle approximation (measured from the sphere center) is $f = R/(2\Delta n)$ which yields $f \approx 18\mu m$, in reasonable agreement with the results in 4.4 where a focus appears at around $70\mu m$.

4.6 Refocusing by biological matter

At this point it would be interesting to investigate whether the refocussing effect can also be observed with a Chinese Hamster Ovary cell, see figure 4.5 (inset).

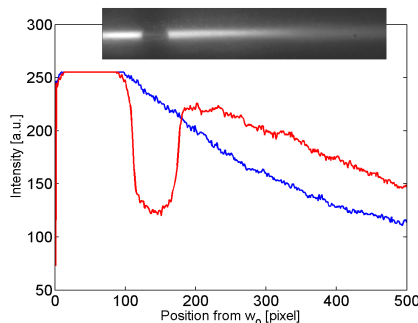


Figure 4.5: On-axis intensity distribution of a CHO cell being guided along the propagation axis from one beam emerging from the lefthand side (red), for comparison the unperturbed Gaussian guiding beam is shown too (blue). Despite that the camera is saturated shortly after ω_0 , the refocusing effect of the cell can clearly be seen by comparing the two profiles. The experimental picture is shown in the black and white inset.

Although the refractive index difference between a CHO cell and its host

³Note that for $3\mu m$ and $5.17\mu m$ diameter silica spheres in water and a free space wavelength of $800nm$, the sphere diameter is almost five and nine times the wavelength in the host medium and therefore the experiments are in the Mie size regime.

medium is very small a subtle refocusing effect was readily observed and is shown in figure 4.5. Importantly here the refocusing effect is less pronounced as with a higher refractive index difference shown in the previous section with spheres. This indicates that diffractive refocusing is the underlying principle of optical binding between cells as well.

4.7 Optically bound arrays

Next I want to consider the case of optically bound arrays with CP laser fields. The number of spheres in an array and the associated separation is dependent on various parameters such as wavelength, waist size and separation, refractive index difference and sphere diameter which has been investigated in the previous chapters; here the focus is the field redistribution that accompanies optical binding and its measurement using two-photon fluorescence. In the previous chapter it was observed that the optically bound array spacing can vary due to variations in sphere size and/or refractive index, even for spheres from the same batch that should nominally have the same properties. To avoid this only a single realisation is considered of each array, so that the array spacing is fixed, and this allows for comparison between theory and experiment.

Optical binding with CP fields arises from the fact that the net force acting on each sphere has two components deriving from the force exerted from each laser field. Considering the case of two spheres for illustration, a given sphere will experience a direct force from the field emanating from the closest laser fibre end, and a second oppositely directed force from the refocused laser field emanating from the other fibre. Balancing of these two forces is the usual explanation of how optical binding can arise, and the extension to more particles follows. Figure 4.6 A) is for example of an optically bound array of two spheres ($N = 2$), and shows the intensity distribution profile for two $3\mu m$ spheres with a separation of $8\mu m$, and very good agreement is obtained between the numerical and experimental profiles.

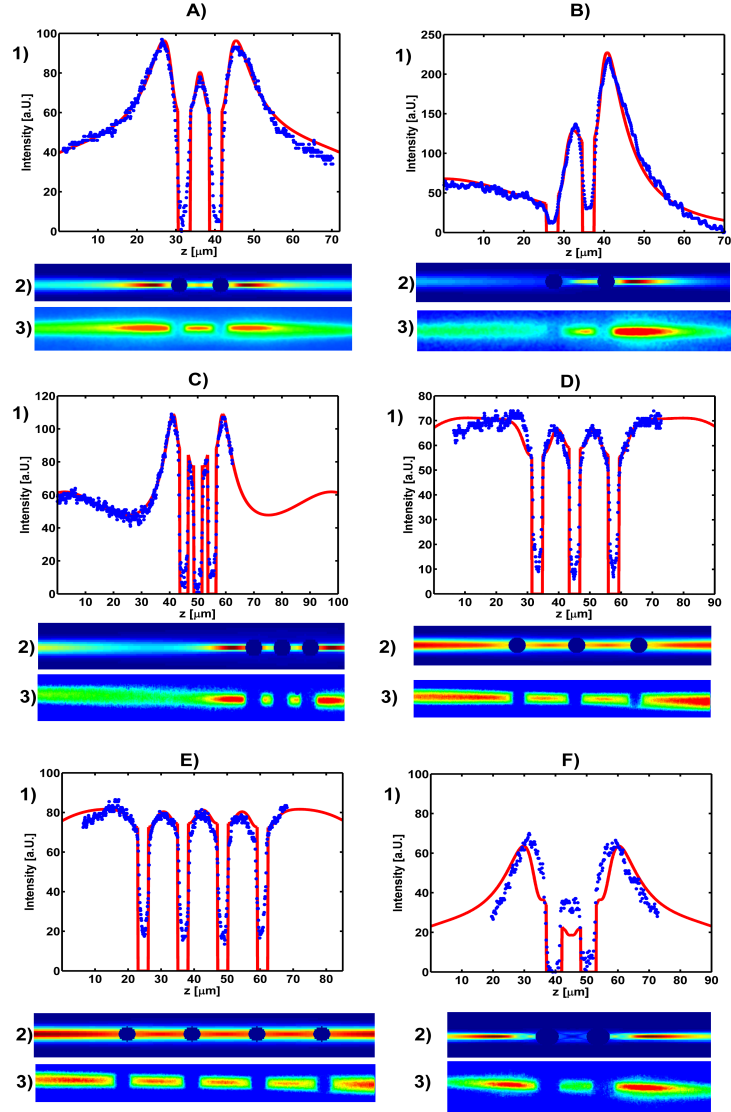


Figure 4.6: A) Two $3\mu\text{m}$ sphere array with a separation of $8\mu\text{m}$ at $\Delta n=0.06$. A1) Centreline intensity distribution showing the full waist separation of $72\mu\text{m}$ (blue - experimental data; red - theoretical prediction). A2) Theoretical simulation of diffraction pattern in a 2 sphere array. A3) False colour image of two-photon fluorescence. B) Same array as in A) with right field blocked at this image the spheres got a separation of $9\mu\text{m}$ the array centre point has got approximately $32\mu\text{m}$ distance to the beam waist. B2) Theoretical simulation of diffraction pattern in a 2 sphere guiding configuration. B3) False colour image of two-photon fluorescence beam coming from left side of picture. C) Three $3\mu\text{m}$ sphere array with a separation of $5\mu\text{m}$ at a $\Delta n=0.05$ with a waist separation of $100\mu\text{m}$. C1) Centreline intensity comparison between theory and experiment which is being cut off at $60\mu\text{m}$. C2) and C3) theoretical and experimental images of diffraction pattern. D) Three $3\mu\text{m}$ sphere array with a separation of $12\mu\text{m}$ at $\Delta n=0.02$ with a waist separation of $90\mu\text{m}$. D1) Centreline intensity comparison between theory and experiment. C2) and C3) theoretical and experimental images of diffraction pattern. E) Four $3\mu\text{m}$ sphere array with a separation of $12\mu\text{m}$ at a $\Delta n=0.01$ with a waist separation of $85\mu\text{m}$. D1) Centreline intensity plot. D2) Theoretical image matching D). F) Two $5\mu\text{m}$ sphere array with a separation of $11\mu\text{m}$ $\Delta n=0.04$ with a waist separation of $90\mu\text{m}$. D1) Centreline intensity comparison between theory and experiment. C2) and C3) theoretical and experimental images of diffraction pattern.

In particular, the profiles clearly show that the intensity is refocused after the spheres, in keeping with the physical picture of optical binding. Figure 4.6 B) is the same as figure 4.6 A) except the right laser field has been blocked, causing the particles to be propelled to the right due to imbalance of the optical forces now acting on the spheres, and for an elapsed time such that the particle spacing had increased to $9\mu\text{m}$. Good agreement is obtained between theory and experiment, and this example further shows that two-photon fluorescence can be used as a tool to obtain real-time monitoring of the dynamics of optically bound arrays. To obtain binding for larger arrays the refractive index difference needed to be lowered in order to inhibit the collapse of the array into a closed chain [17, 11]. Qualitatively this phenomena may be explained as follows: a lower refractive index difference subsequently causes less light being refocused by a sphere (as was shown in figure 4.4 onto its nearest neighbour in the array. For the case of $3\mu\text{m}$ sized spheres this means that by decreasing the refocusing effect of each individual sphere, the balance of the forces from both CP fields is still maintained for a higher number of spheres N . The results in figures 4.6 C) and D) are for optically bound arrays with $N = 3$. Figure 4.6 C) shows three spheres bound in an array, when Δn is changed to 0.05. The separation of the spheres decreased to $5\mu\text{m}$ and did not permit the optical field to emerge further between the spheres. If the refractive index difference is further lowered the separation of the three sphere array increases to $12\mu\text{m}$ thus permitting the fields in between the spheres to evolve further. It can be clearly seen that the refocussing effect has decreased significantly as both exit peaks of the intensity at either end of the array have decayed off in comparison to C). With a refractive index difference of 0.01, $N = 4$ spheres can be bound in an array whilst having a very large spacing of $12\mu\text{m}$, as shown in figure 4.6 E). Here again the reduced refocusing effect can be clearly seen at each end of the array, where the on-axis intensity peak has significantly decreased in comparison to figures 4.6 A) or C).

Additionally a two $5\mu\text{m}$ sphere array with a separation of $11\mu\text{m}$ at $\Delta n = 0.05$ is shown. Here the field between the two spheres has hardly evolved even though the refractive index difference is relative high.

These examples amply demonstrate that imaging of two-photon fluorescence is a reliable tool for visualising the redistribution of intensity in optical binding of arrays, and that our model for the field propagation is valid in the Mie size regime considered here.

4.8 Optical bistability in bound matter

As the sphere position influences the diffractive refocusing of the field and vice versa this may result in more than one stable sphere separation as shown in the previous chapter. In figure 4.7 A) and B) two such stable positions for $2.3\mu\text{m}$ spheres are shown.

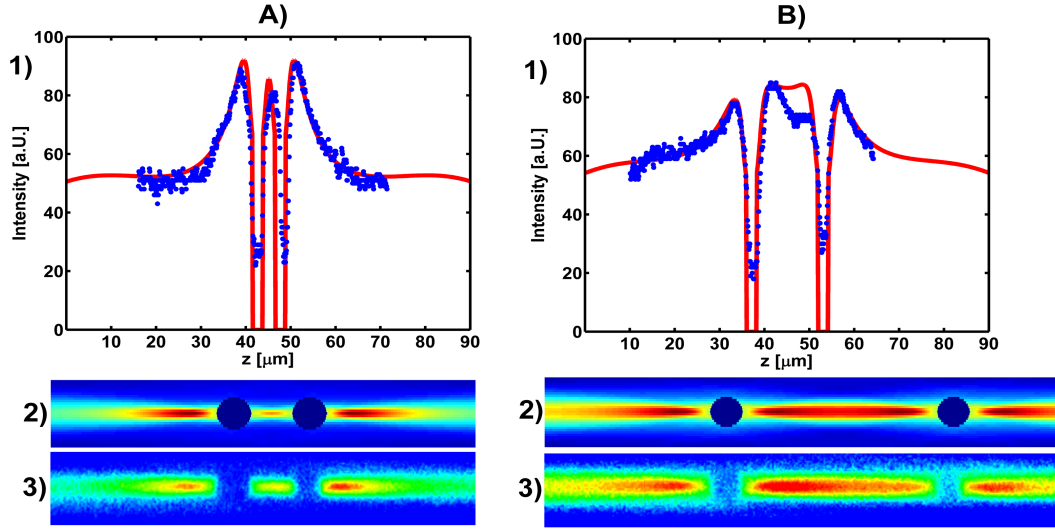


Figure 4.7: On-axis intensity distribution of two $2.3\mu\text{m}$ sphere array exhibiting bistability with a separation of A) $5\mu\text{m}$, and B) $16\mu\text{m}$ with $\Delta n=0.09$ and a waist separation of $90\mu\text{m}$. The respective on-axis intensity plots show a slight disagreement for a separation of $16\mu\text{m}$ in B1) which is caused by sphere size variation within the sample batch. Respective intensity planes are shown in A2) and B2) for the simulations and A3) and B3) from the experiment.

Comparing both graphs shows that with a small separation the intensity peak after the light exits the array is very pronounced which indicates a high intensity and a strong optical gradient. For the large separation those peaks have significantly decreased permitting the field intensity between the spheres to evolve.

4.9 Conclusion

In this chapter I described the development of a novel femtosecond fibre optical trap that permitted the first direct visualisation of the process of optical binding for microparticles, including the light distribution within an array

and the light redistribution in optical guiding. A numerical model for diffraction and beam propagation was developed based on the the paraxial code of Ref. [18, 61] that allowed a direct comparison between experiment and theory for the resultant light redistribution in these cases. It also permitted validation of the physical and the numerical model of optical binding in the Mie size regime.

Visualisation of the light distribution within an optically bound array confirms that diffractive refocusing of the incident light fields is one of the key physical issue for array formation.

I expect that the two-photon imaging methods reported in this section will have broader use in the field of optical binding and in diagnosing the physics of optical micro manipulation.

Interestingly binding at a wavelength of $800nm$ and $w_0 = 2.5\mu m$ is not observed for $3\mu m$ at higher refractive index differences e.g. at $\Delta n = 0.09$, here the spheres collapsed. This is in contrast to $\lambda = 1070nm$ and $w_0 = 3.4\mu m$ shown in figure 3.5. Also bistable binding was not observed for $3\mu m$ at $\lambda = 800nm$, here the bistable regime shifted to a sphere size of $2.3\mu m$.

At this point, these observation can only be qualitatively explained as two parameters were varied, the wavelength as well as the modefield diameter. Specifically, the modefield diameter and NA for $800nm$ is $NA = 0.13$, $w_0 = 3.6\mu m$, with a Rayleigh range of $\pi\omega_0^2/\lambda = 25\mu m$, which is in contrast to the experiments from the previous chapter. Where at a wavelength of $1070nm$ the NA equals to 0.14 , $w_0 = 3.6\mu m$ and the Rayleigh range is calculated to be $38\mu m$. These optical field parameter changes, the gradient as well as the wavelength of the field incident on the spheres, have significant influence on the field distribution at the sphere and can be attributed to cause the observed shift in optical binding and bistability to smaller sphere sizes. The scaling of the sphere size is approximately linear with the wavelength and the modefield diameter.

Importantly this shift of the bistability is well captured by the numerics, as the stable positions were found experimentally to be $5\mu m$ and theoretically to $5.7\mu m$. Theoretically the unstable solution was found at $8.0\mu m$, the second stable solution was theoretically predicted at $14.7\mu m$ and experimentally measured to $16\mu m$, with a Δn of 0.09 in D_2O and a fibre separation of $90\mu m$. Here again good agreement between the theoretically modelled and experimentally observed equilibrium separations could be established.

Chapter 5

Restoring forces and correlation in optical binding

Colloidal suspensions are nowadays well established as controllable systems that offer the possibility to investigate a wide range of physical phenomena. One intriguing question in such colloidal suspensions is the memory effect of its particles. Which is in the simplest case, does one colloid remember the position of its nearest neighbour some time in the past. Let us consider the case of two individual particles being confined in a potential well, where the position trajectory of only one particle can be measured. Even if the Brownian forces that displace the observed particle from equilibrium are known, the trajectory of the second particle cannot be deduced and the system is unobservable¹. But if some sort of coupling mechanism is introduced between the two spheres the system becomes observable and we can calculate the position trajectory of the second (unknown) particle solely from the knowledge of the first particle trajectory, the thermally induced forces acting on it and the shape of the potential well. Such a coupling mechanism that renders a system observable can be by hydrodynamic interaction via the host medium in the realm of optical tweezers. This hydrodynamic coupling between two individually trapped (but not optically coupled) spheres has been studied by Meiners and Quake [63], Bartlett [64] and for more than two spheres by Polin [65]. The geometry used to investigate such purely hydrodynamic coupling is show in figure 5.1 (left). Two optical tweezers hold two spheres at a variable

¹Observability [62] is a mathematical measure which states whether a system has a memory and its past internal state can be calculated from the system input and output variables.

distance apart from each other. The thermal noise induced movement of the spheres is in this case coupled via the liquid between them. Interestingly the cross-correlation of the two normal modes of the spheres motion showed time delayed anti-correlation due to the complex fluid flow in between the trapped objects. The novelty of our approach described in this chapter is

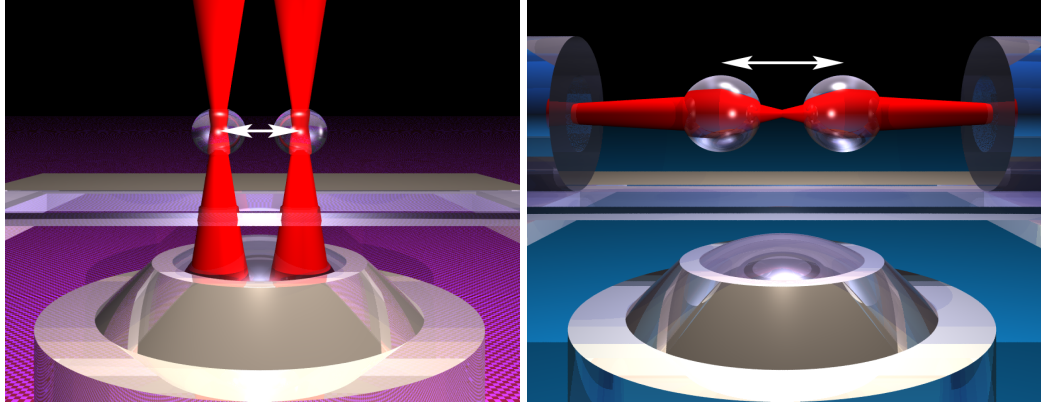


Figure 5.1: Left: Two individually trapped spheres held by two optical tweezers, the light fields are shown in red. Such a system is used in studies by [63, 64] to investigate purely hydrodynamic coupling between two spheres. The white arrow indicates the interaction direction between the two spheres. Right: In an optically bound array the interaction between the two spheres is via the trapping light fields (shown in red). Here the interaction between the two spheres is along the propagation direction of the two beams and indicated by a white arrow.

that virtually no correlation studies have been performed in an optically bound system where the optical coupling plays a prominent role, as shown in figure 5.1 (right). The optical coupling mechanism between a particle and its nearest neighbour lies at the heart of optical binding. This optical interaction between the colloidal particles in such a bound array thus should lead to correlated positional fluctuations between the trapped objects, mediated by the trapping light. In this chapter I will present data and analysis on the correlated behaviour of a one-dimensional array of two optically bound micro particles in the presence of noise, and theoretically fully incorporating both the optical and hydrodynamic interactions between the microparticles. In particular, I will show that measurement of the decay time of the correlation functions of the center of mass and relative normal modes provides an *in situ* method for determining the optical restoring forces acting on the optically bound particles, thereby determining the linear response of the system. Building upon the experiments in chapter 3, I will now move on to investigate small displacements of the trapped spheres due to Brownian noise, starting

at the simplest case of only one trapped particle to elucidate the approach. This chapter is organised as follows, first I will describe the optical fibre trap and the underlying theoretical model used for one sphere and for two optically bound spheres. Then the experimental and theoretical results for a two sphere case are presented. A future outlook is given at the end, including a discussion of parasitic interference effects in an optically bound array.

5.1 Integrated optical fibre trap

The counter-propagating fibre trap described in the previous chapter had to be integrated with the sample chamber in a hermetically sealed system, to achieve the necessary accuracy for the Brownian motion measurements. Specifically to avoid perturbative flow, evaporation and achieve counter-propagating alignment of the fibres an integrated trap had to be built (see reference [66] for a detailed description of different integrated fibre trap designs). To begin I will describe the beam delivery setup, this was amended slightly to enhance the temporal light power stability and to allow for additional power monitoring of the trapping light.

The two opposing fibres (marked F1 and F2) were operated using light from a continuous wave Ytterbium Fibre laser (IPG Photonics) at $\lambda = 1070nm$ with an optical isolator to avoid perturbations of the laser due to back reflections. The light was coupled into one single mode fibre, and split into two equal beams via a 50:50 fibre splitter (OZ optics Ltd.) to provide equal field distribution within the trap of $110mW$ from each fibre. With this setup it was ensured that laser fluctuations and drift of the in-coupling stage would affect both beams accordingly. Additionally, the back-coupled light from the trap was measured at the second fibre splitter in-coupling port to observe and eradicate long-term drift of the coupling setup. This enabled to achieve overall light intensity stability within the trap of better than 7% over multiple experimental realisations. Also this allowed for control of contamination in the trap. When dirt (usually of the order of $1\mu m$ diameter and smaller) enters the array the back-coupled light will increase and give a good indication when the experiment had to be halted.

To further ensure symmetric array formation at half the fibre separation one arm could also be attenuated by a variable fibre attenuator, and the fibres were of different length to again avoid standing wave effects from the opposing fields.

Two different fibre trap designs were utilised and evaluated during the experiments. A first design was realised by R.F. Marchington and will be discussed in detail elsewhere. Here the sample chamber consisted of a polydimethylsiloxane (PDMS) micro fluidic structure in which the two fibres were embedded to form a counter-propagating fibre trap with a fixed separation D_f between the fibre ends. The sample medium with the microspheres was injected through a $100\mu m$ flow channel, perpendicular to the fibre trap. The micro fluidic structure was hermetically sealed to prevent evaporation and flow within the sample. The softness of the PDMS did not allow for accurate alignment of the two fibres and each trap had to be tested on the degree of misalignment of the fibres before being used. A misaligned trap causes the trapped spheres to circle back and forth between the two beams. A sensitive measurement method here is a collapsed chain of 4 to 5 spheres which gives a good indication on how well aligned the fibres are (in a good trap the chain stays centred at $D_f/2$).

In a second design a v-grooved (Adamant Kogyo Ltd.) glass coverslip was used to align the two fibres. The sample chamber itself was built in a multi step process:

- The base of the sample chamber consisted out of two flexible heating elements (MINCO) that were sandwiched between two glass coverslips. A gap of $2mm$ between them allowed the trap area to be viewed via the microscope.
- The two fibres were loosely placed facing each other on top of the sandwiched base structure. The v-grooved glass coverslip was placed on top of the fibres, so the fibres reside in the groove.
- Now the sample medium was added slowly, so no air pockets could form in the sample area. Additionally, by moving the v-groove along the two fibres air bubbles could be removed from the sample area. Once the sample area was bubble free, the gap between v-groove slip and the glass bottom structure was hermetically sealed around the edges of the v-grooved coverslip with liquid PDMS.
- The whole structure was fixed via a clear plastic lid with 4 screws, which were carefully tightened. Before the fibres were pressed into the v-groove, their separation was fine adjusted to give a fixed separation D_f between the two fibre facets.

A drawing of the sample chamber is shown in figure 5.2.

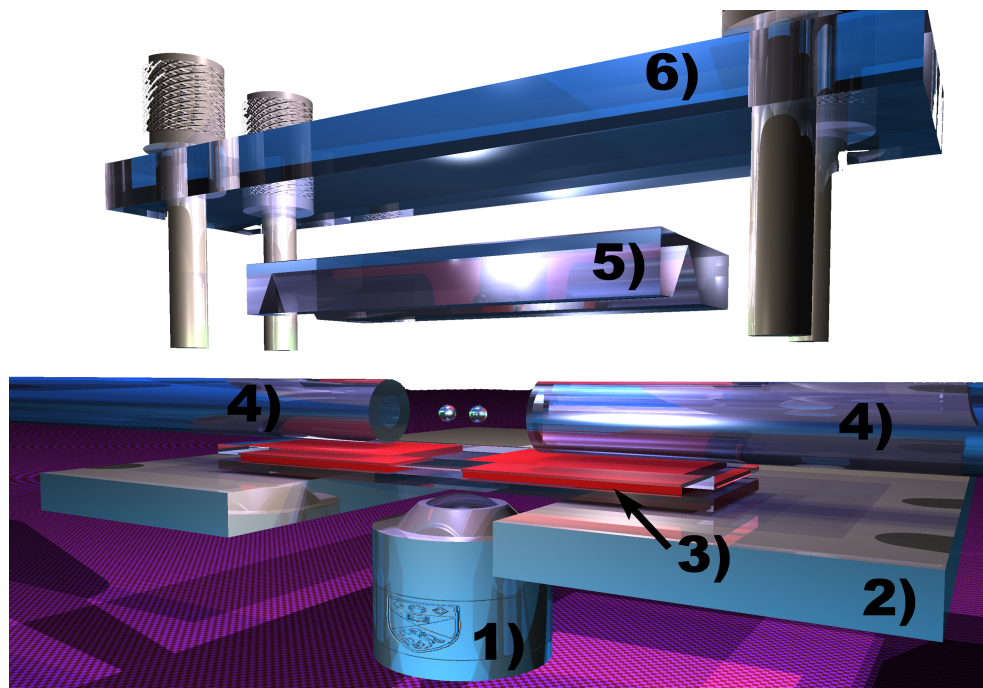


Figure 5.2: Exploded drawing of the integrated fibre trap: 1) Imaging setup with additional helper tweezers. 2) Aluminium base plate to hold the whole sample cell. 3) Glass base sandwich structure, consisting out of two heaters (red) sandwiched between two glass coverslips, a gap between the heaters allowed for imaging of the array. 4) Single mode fibres. 5) Glass v-groove to align the two fibres counter-propagating. 6) Clear PVC cover lid with 4 screws to tighten the whole sample cell.

Although the alignment accuracy of this trap is excellent it suffers from the fact that the sample chamber is hermetically sealed. Here contaminations that get enclosed during the assembly process cannot be washed out as in a flow channel design. These contaminations (dirt) will over time accumulate in the fibre trap and therefore did not allow for long measurement integration times. Each piece of dirt acts as a Rayleigh scatterer and decreases the Brownian motion of the spheres. Due to the observation mechanism via the quantity² of back-coupled light (described above), it was however possible to eradicate measurements where dirt entered the fibre trap.

The base coverslip could be heated to $40^\circ \pm 0.5^\circ\text{C}$ with the two thermofoil heaters (MINCO) to enhance the Brownian motion of the system and de-

²Dependent on the exact spheres parameters (refractive index) around 15mW for a $3\mu\text{m}$ 2 spheres array at 110mW per fibre at $D_f = 90\mu\text{m}$.

crease the measurement integration time [65]. The trap temperature was measure with a high sensitivity infrared (IR) camera; a detailed description of these experiments will be given in section 5.2.7. To ensure convective heat currents are not present the position distribution of each sphere along the x-axis (perpendicular to the beam propagation direction) was measured as well. A Gaussian distribution of the position histogram indicates that such non Brownian noise sources are not present³ [67]. Additionally, measuring the distribution of the two trapped spheres along the x-axis, for all measurements presented the distribution in z and x showed a Gaussian profile without slanting [67]. This indicated that convective heat currents in the sample chamber are not present.

A mono-disperse mixture of silica microspheres and water as described in chapter 2 was used as the sample medium.

The trapped spheres were observed via a microscope objective (MITOTUYO long working distance 50 \times) onto the CCD array of a fast camera (Basler A622f) with a data acquisition rate of $\Delta t = 0.0025sec$. To further enhance the image quality of the captured footage for subsequent particle tracking, a Koehler illumination setup [68] was add to the experiment rig.

Following the approach of [65], the captured frames were analysed utilising an IDL based particle tracking software [69] and the particle position in z_N extracted with an accuracy of better than $50nm^4$. Subsequent data processing involved compensation of an angular offset of the z-axis to avoid crosstalk between the z and x coordinates of the spheres.

These changes were key to achieve the required accuracy in the measurements to determine the spring constants involved in the fibre trap system on N spheres ($N = 1, 2$).

In the following section I describe the theoretical model that underpins my subsequent experiments.

5.2 Theoretical model

To theoretically predict the restoring forces and the sphere motion in response to Brownian noise in the counter-propagating fibre trap two different models were used. I am first going to describe the theoretical extension obtained from

³Liquid flow in the sample chamber would result in a slanted Gaussian distribution.

⁴Here the developed particle tracking software proofed to be insufficient as the limit is about half a pixel, dependent on the used microscope this is not better than 80 nm.

Prof. E.M. Wright based on the model described in the theoretical chapter, to determine the spring constants of the system of one sphere. Secondly I will describe a model developed by Dr. M. Mazilu which simulates the particle dynamics for a given spring constant of the system for one sphere. Throughout an experiment with a $5\mu m$ silica sphere is used to compare experimental results to the theoretical predictions.

Finally I am going to extend both theories to a two sphere array and compare it with experimental findings.

5.2.1 Simulation and calculation of the restoring force on a single sphere

Initially I want to introduce the restoring forces acting on a single sphere in a counter-propagating fibre trap as shown in figure 5.3.

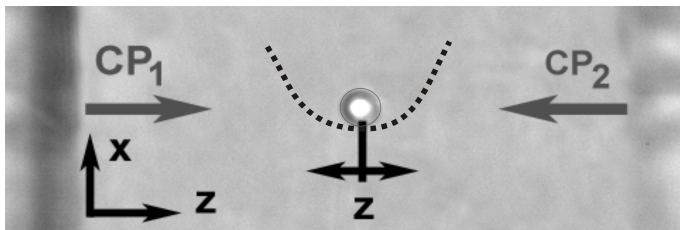


Figure 5.3: Single sphere in a CP beam trap. Here only one spring constant is acting (κ), which is shown as the dashed potential in which the sphere reside. Indicated as $z(t)$ are the noise induced fluctuations around $D_f/2$ where $z = 0$. The underlaid picture is from an captured frame of the experiment.

Two approaches will be introduced in this section, which will use a single $5\mu m$ silica sphere immersed in D_2O in a CP fibre trap, with light field parameters $110mW$ at $\lambda = 1070nm$ with $\omega_0 = 3.6\mu m$ and separation of the beam waists of $D_f = 50\mu m$ as an example. First a static approach is used to calculate the spring constant, based on the theoretical model of chapter A.5 for one sphere. Here the magnitude of the force is calculated for different displacements from equilibrium (at $D_f/2$). Secondly a dynamic approach is introduced, which uses the Langevin equation of motion to simulate the thermally induced motion of a sphere in a harmonic potential well for a given spring constant. Additionally both theoretical approaches are compared to experimental findings.

5.2.2 One sphere spring constant theoretical calculation

Here I am utilising the theoretical model to calculate the force acting on a single sphere, presented in the theoretical chapter in equation A.23 extended to two counter-propagating beams. When the particle is displaced along the z -axis from equilibrium at $z = 0$, $D_f/2$ it feels a restoring force against the direction of the perturbation, whose magnitude can be calculated for different offsets $-1\mu m \leq z \leq 1\mu m$ from the center $D_f/2$. An example calculation is shown in figure 5.4.

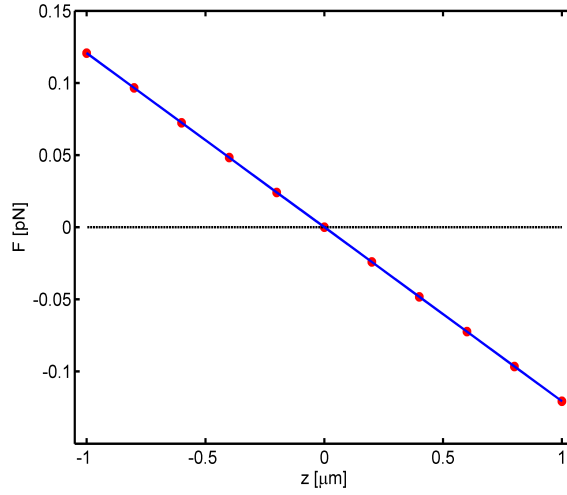


Figure 5.4: Evolution of the force on one sphere exerted by two counter-propagating beams when displaced from equilibrium at $D_f/2$ where $z = 0$. For a $5\mu m$ silica sphere with a refractive index mismatch of $\Delta n = 0.1$ with field parameters of $110mW$ at $\lambda = 1070nm$ with $\omega_0 = 3.6\mu m$ and $D_f = 50\mu m$. Here the acting force evolves linear as $F = -\kappa_z z$ with $\kappa_z = 0.121pN/\mu m$.

From the slope of the graph, the spring constant κ of the system can be directly obtained, with $F = -\kappa z$. Here $\kappa_z = 0.121pN/\mu m$ for the simulated case in figure 5.4.

Similar to A.26 the effective potential can be calculated to

$$U = - \int^D \delta z F(z) \quad (5.1)$$

and can aide direct comparison between the experiment and model. With the known trap stiffens the response of such a one sphere system to Brownian

noise can be simulated.

5.2.3 Dynamic simulation of one sphere in a potential

Following approaches from references [67, 69] the trajectory of a particle in a harmonic energy potential well is defined by the one dimensional Langevin equation [70]:

$$\frac{\partial z(t)}{\partial t} = -\frac{z(t)}{\tau} + F(t) \quad (5.2) \quad \frac{m \frac{\partial^2 z(t)}{\partial t^2}}{m = \text{mass}} = \text{initial term}$$

where the inertial term has been neglected due the strong viscous damping of the host medium [67, 69]. τ is the autocorrelation decay time⁵ of the particle position z , which is given by:

$$\tau = \frac{6\pi\eta r_{\text{sphere}}}{\kappa} \quad (5.3) \quad \kappa = \text{spring constant}$$

$F(t)$ is the thermal or Brownian force acting on the sphere; which has zero mean $\langle F(t) \rangle = 0$ and variance

$$\sigma_F^2 = \langle F(t)F(t') \rangle = 2 \frac{1}{\underbrace{6\pi\eta r_{\text{sphere}}}_{\gamma}} k_b T \delta(t - t') \quad (5.4) \quad \begin{array}{l} \gamma = 6\pi\eta r_{\text{sphere}} \\ \gamma = \text{viscous drag coefficient} \\ k_b = \text{Boltzmann's constant} \end{array}$$

where η is the viscosity of the host medium and γ the viscous drag coefficient of the sphere of radius r_{sphere} . The particles position is given after time t from the initial position at $t = 0$ with z_0 by:

$$z(t) = z_0 \exp\left(-\frac{t}{\tau}\right) + \int_0^t F(t') \exp\left(-\frac{t-t'}{\tau}\right) dt' \quad (5.5)$$

where

$$z'(t) = -\frac{1}{\tau} z_0 \exp\left(-\frac{t}{\tau}\right) + F(t) + \int_0^t F(t') \left(-\frac{1}{\tau}\right) \exp\left(-\frac{t-t'}{\tau}\right) dt'$$

⁵At the 1/e point.

Under experimental conditions the movement of the spheres is sampled via (for example) a camera at discrete times $t_j = j\Delta t$ where j is the integer of the sampled data points or individual frames and Δt is the sampling rate determined by the frame rate. This simplifies equation 5.5 to:

$$z_{j+1} = \exp\left(-\frac{t}{\tau}\right) + f_{j+1} \quad (5.6) \quad \text{where } z_j = z(t_j)$$

where f_{j+1} is again the Brownian noise source with zero mean $\langle \sum_j f \rangle = 0$ and variance

$$\sigma^2 = \frac{k_b T}{\kappa} \left[1 - \exp\left(-\frac{t}{\tau}\right) \right] \quad (5.7)$$

This formula can be simply programmed in a random walk model utilising MATLAB. Now the sphere trajectory can be calculated for a given temperature and trap stiffness. For the $5\mu m$ sphere such a trajectory is plotted in figure 5.5 (left). Hence for a given spring constant and temperature the

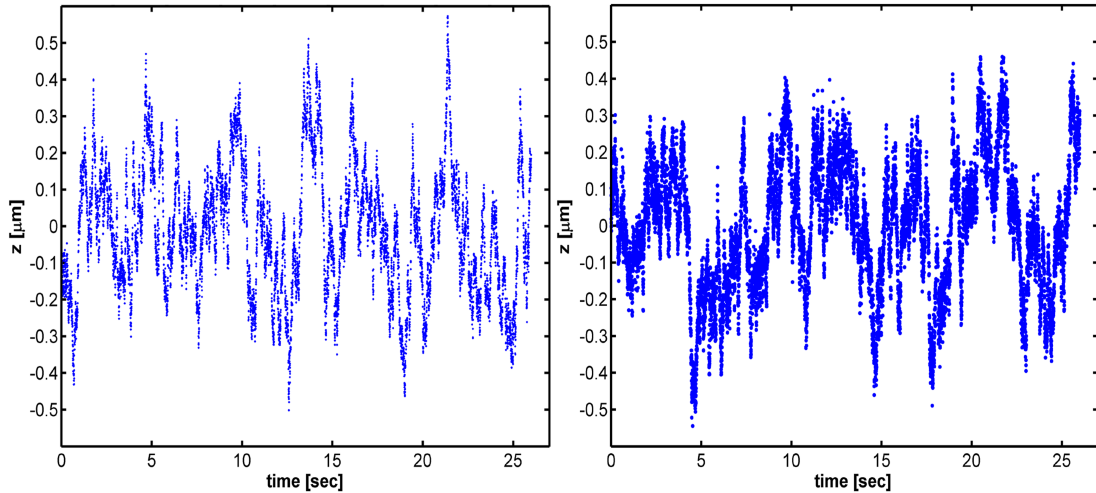


Figure 5.5: Left: Random walk simulation of a $5\mu m$ in a harmonic potential with a spring constant of $0.132pN/\mu m$ at room temperature. The shown data set is over $27sec$ total sampling time and a sampling interval of $\Delta t = 2.6msec$. Right: Experimental sample set (with the corresponding conditions of the simulation), the sample set proves that a sampling rate of $385Hz$ suffices to sample the frequency of the movement randomness, see [71]. The data was obtained from the experiment described in the previous chapter.

random walk for a sphere can be simulated and directly compared with the

experiment, shown in figure 5.5 (right).

Next I will compare experimental and theoretical results for the spring constant of one sphere in a CP trap.

5.2.4 Trap stiffness from Boltzmann statistics

The position ensemble, resulting from a particle moving in a potential (equation 5.2) with sampled positions shown in figure 5.5, is described by Boltzmann statistics [71].

$$P(z) = \exp\left[-\frac{U(z)}{k_B T}\right] = \exp\left[-\frac{z^2}{2\sigma_z^2}\right] \quad (5.8) \quad U(z) = \frac{1}{2}\kappa z^2$$

Where $P(z)$ is the probability of finding the sphere in a potential $U(z)$ in thermal equilibrium. Figure 5.6 shows such a probability distribution for experiment and theory. By measuring the probability density $P(z)$, the po-

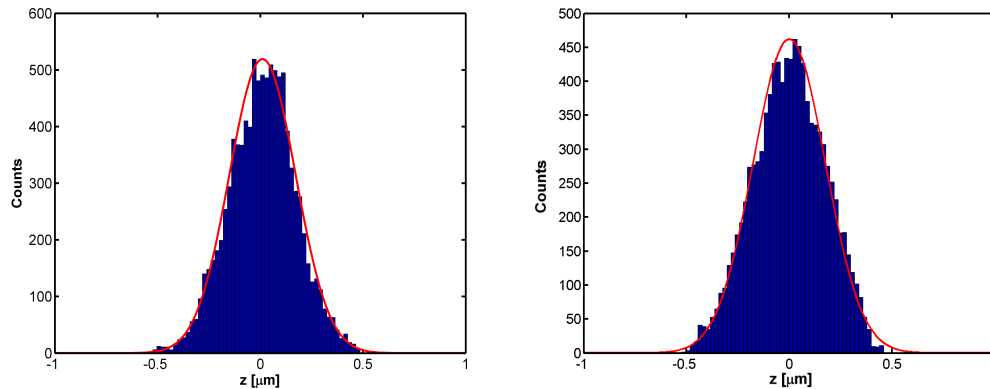


Figure 5.6: Same Data as figure 5.5. Left: Theoretical distribution Right: Experimental distribution function. A Gaussian curve is fitted to the bins of 50nm width to aid the eye.

tential experienced by the particle can be calculated [72]:

$$U(z) = -k_b T \ln [P(z)] + C \quad (5.9) \quad \begin{array}{l} U(z) \text{ in units of energy} \\ [\text{Nm}] \text{ or } [\text{J}] \\ C \text{ is potential offset for} \\ \text{normalisation to zero} \end{array}$$

In figure 5.7 the potential for the 5 μm silica sphere in the CP trap is plotted. Additionally I overlaid the numerically modelled potential which follows

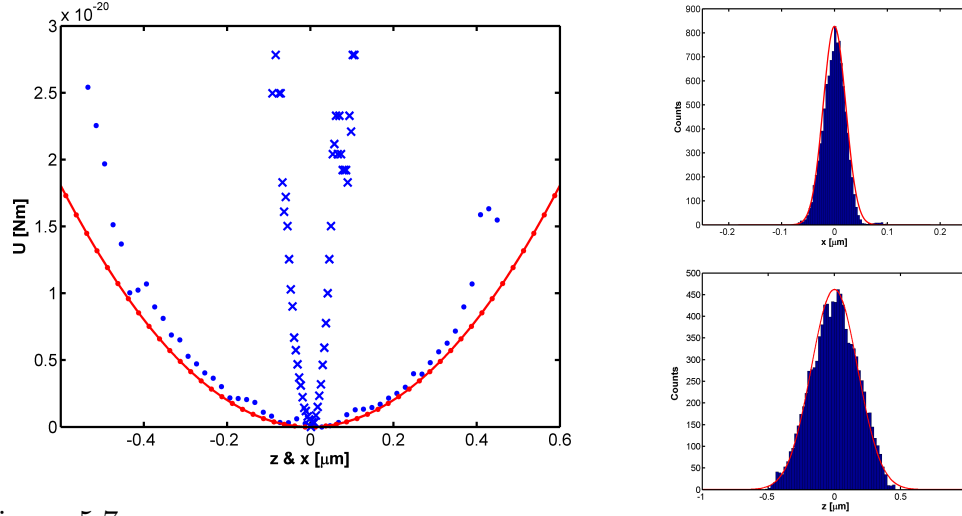


Figure 5.7: Effective potential of one $5\mu\text{m}$ silica sphere in an CP fibre trap. Red line - simulated potential along the z -axis. Blue dots - experimental determined potential along z -axis. Blue crosses - experimental determined potential along x -axis. Here the light field parameters were 110mW with a fibre separation of $50\mu\text{m}$. For comparison the two histograms for the z and x position data of the sphere are shown in the two right hand graphs (above displacement in x - below displacement in z).

from the data of figure 5.4 with equation 5.1 to $U(z) = \frac{\delta F(z)}{\delta z}$ with the experimental potential from equation 5.9 for direct comparison. In figure 5.7 both potentials are shown for the z and x -axis. Importantly due to the divergence of the fields emerging from the fibers, the trap stiffens along the field propagation axis is lower than in the plane of propagation (the xy -plane). The experimental force constant can be quantified via the Equipartition theorem [73, 74, 71, 72] which states:

$$\kappa_\sigma = k_b T / \sigma_z^2 \quad (5.10)$$

where σ^2 is the variance of the position distribution. This measurement is independent of the viscosity η , however it relies on the accurate calibration of the system to measure the position fluctuations (here) $z(t)$ as additional non Brownian noise can decrease the measured trap stiffness value⁶.

From the equipartition theorem the experimental trap stiffness follows to $\kappa_z^\sigma = 0.131\text{pN}/\mu\text{m}$ and $\kappa_x^\sigma = 8.95\text{pN}/\mu\text{m}$.

⁶Errors (e.g. from fluid flow or vibrations) comes in to the square - hence any inaccuracy has a significant effect.

5.2.5 Trap stiffness from the autocorrelation decay time

A particle confined in an harmonic potential well has a exponentially decaying position autocorrelation function [75, 71]:

$$\begin{aligned} \langle z(0)z(t) \rangle &= \langle z \rangle^{-2} \exp\left(-\frac{t}{\tau_z}\right) \\ &= \langle z \rangle^{-2} \exp\left(-\frac{\kappa}{6\pi\eta r_{sphere}} t\right) \end{aligned} \quad (5.11)$$

z = displacement along z-axis
 $\langle z \rangle^{-2}$ = normalisation of autocorrelation

Where $\langle z \rangle^{-2} = k_b T / \kappa_z$ is the mean square fluctuation of the particle⁷. From the position autocorrelation decay time follows, as in equation 5.3 from reference [75], the spring constant κ_z^τ to:

$$\kappa_z^\tau = 6\pi\eta r_{sphere} / \tau_z \quad (5.12) \quad \kappa_z^\tau = \text{trap stiffness in } z$$

Importantly the autocorrelation method does not rely on exact calibration of the position detection as the autocorrelation is normalised to unity. It relies however on a harmonic potential in which the sphere is confined. Experimentally the following results for κ_z^τ and κ_x^τ were obtained (figure 5.8): $\kappa_z^\tau = 0.126 \text{ pN}/\mu\text{m}$ and $\kappa_x^\tau = 3.77 \text{ pN}/\mu\text{m}$.

With these two methods to determine the trap stiffness, I am now in a position to utilise one sphere as a local viscosity probe.

5.2.6 Local viscosity probe

In the previous sections I have introduced two autonomous ways of determining the trap stiffness; equation 5.12 and equation 5.10 which is independent of the viscosity of the host medium. The local viscosity is temperature dependent [71] and will be important for subsequent measurements for two spheres for an increased trap temperature. For this reason I will give an example of how a trapped sphere can act as a local viscosity probe, following the approach of [71].

From 5.12 follows

⁷In the analysis used to normalise the autocorrelation to unity at $t = 0$ as $\frac{\langle z(0)z(t) \rangle}{\langle z(t) \rangle^2}$.

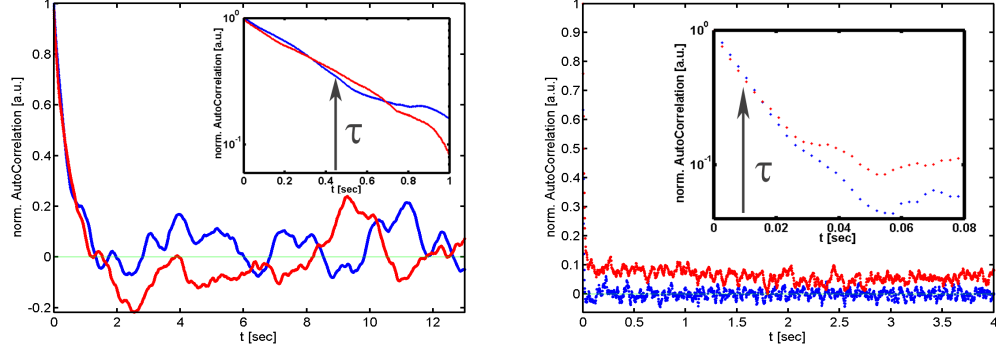


Figure 5.8: Left: Blue normalised autocorrelation of the z displacement of a $5\mu m$ silica sphere. Red shows the result from the random walk model with the experimentally determined spring constant $\kappa_z^\tau = 0.126pN/\mu m$. Right: Blue experimentally determined autocorrelation for the sphere in x . Red theoretical simulation for the experimentally determined spring constant $\kappa_x^\tau = 3.77pN/\mu m$. Importantly the oscillations around the zero line are dependent on the length of the data set (as the data set length increases the oscillations become less evident) and the trap stiffness. Although for the autocorrelation in z the amplitude of these oscillations is very high the autocorrelation decay time τ at the $1/e$ point (arrowed in both graphs in the inset log plot) has been tested to be robust against different length of data sets.

with $1cP = 0.001 Pa \text{ sec}$

$$\begin{aligned} \frac{1}{\tau_z} &= \frac{\kappa_z^\sigma}{6\pi\eta r_{sphere}} \\ \eta &= \frac{\kappa_z^\sigma \tau_z}{6\pi r_{sphere}} \end{aligned} \quad (5.13)$$

Where κ_z^σ is determined via the variance method and τ_z is calculated from the autocorrelation decay time. So an *in situ* measurement method for the local viscosity is given. For the described $5\mu m$ silica sphere experiment, with an estimated trap temperature of $20^\circ C$ (room temperature) the measured viscosity follows to $1.29cP$, which is in agreement with the viscosity from the literature of $1.25cP$ for the host medium (D_2O at a temperature of $20^\circ C$), as shown in graph 5.9 (red).

In the graphs of figure 5.9 the data points (obtained from the literature) were fitted with a fourth order polynomial $Fitt = p_1 * x^4 + p_2 * x^3 + p_3 * x^2 + p_4 * x + p_5$ where the constants p_i are shown in the following table, the references are given within.

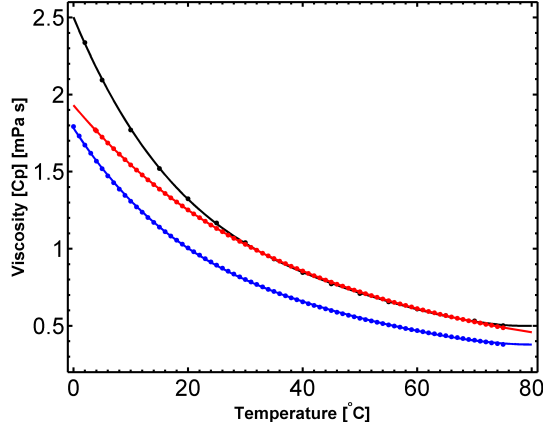


Figure 5.9: From the literature obtained temperature dependent viscosity. Black - DI water with 10% sucrose solution. Red - D_2O . Blue - DI water (H_2O).

Host medium	p_1	p_2	p_3	p_4	p_5
10%Brix [76, 77, 78]	$1.82 * 10^{-8}$	$-4.93 * 10^{-6}$	$0.60 * 10^{-3}$	$-4.41 * 10^{-2}$	1.93
D_2O [79]	$5.90 * 10^{-8}$	$-1.29 * 10^{-5}$	$1.15 * 10^{-3}$	$-5.73 * 10^{-2}$	1.78
H_2O^8 [80, 78]	$9.81 * 10^{-8}$	$-2.16 * 10^{-5}$	$1.90 * 10^{-3}$	$-8.93 * 10^{-2}$	2.50

Importantly the viscosity is strongly dependent on the temperature, especially around room temperature. Therefore I want to give a brief discussion on temperature effects and measurements in the next section.

5.2.7 Temperature measurements and heating effects

In this section I will briefly discuss heating effects in the fibre trap and elucidate different temperature measurement methods.

The local trap temperature in the experiment can be probed just like the viscosity via the Brownian motion of the trapped sphere by determining the diffusion coefficient $Diff$, from [81, 82] and from the Stokes-Einstein relation [83, 84]:

$$T_{Diff} = \frac{Diff * 6\pi\eta r_{sphere}}{k_b} \leftarrow \langle z^2 \rangle = \frac{\sum_n \Delta z^2}{n} = 2Diff\Delta t \quad (5.14)$$

$\langle z^2 \rangle$ = Mean square displacement
 n = number of discrete data points

The temperature calculation presented here evolves from the mean square displacement (MSD) of a particle that is bombarded by fluid molecules, in this case for one dimension along the z-axis. *Diff* indicates the Brownian thermal induced diffusivity or diffusion coefficient [82]. In the experiment no agreement was achieved between the approximated trap temperature of $273K$ and the determined one $T_{Diff} = 1417K$.

Here I suspect that the sampling of the spheres motion via the video analysis is not accurate enough to produce a meaningful result. For this reason the trap temperature has been either approximated by measuring with a thermocouple or via measurements with an infrared (IR) camera for the heated sample cell.

To give the sample medium a set temperature, heating elements were incorporated into the trap, this enhances the Brownian motion and decreases the integration time due to the enhanced Brownian movement of the spheres. The temperature⁹ was measured with an IR camera as shown in figure 5.10.

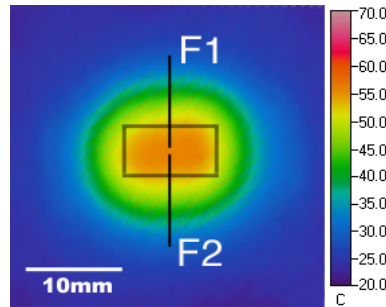


Figure 5.10: Temperature gradient in the sample area. Here the heated top coverslip is imaged via an IR camera and shown in an false colour plot. The two fibers (F1 and F2) are shown in the picture to elucidate the geometry. The actual sample cell made up by the v-groove $10 \times 5mm$ spans over the marked area in the picture. A gradient of $\approx 5^\circ C$ is measured over the sample area. However no convective currents were observed in the analysed data. The images shows a homogeneous temperature of $\approx 62^\circ C$ at the sample area.

With this method the temperature was determined prior to every experimental realisation, where the sample was additionally heated.

Heating of the sample cell also changes the refractive index of the host medium; here a correction of $n_h = n_h^{20^\circ} - 0.013$ for a temperature from 20 to $50^\circ C$ via the formula $n_h(T) = n_h^{20^\circ} - 0.00045(T - 20)$ where T is in $^\circ C$ from [85] is used for the theoretical simulations.

⁹The temperature of the top glass cover slip without fluid.

Additional heating in the sample cell can lead to convective roles in the host medium, which can induce perturbations to the Brownian motion trajectory of the trapped sphere. As the temperature shown in figure 5.10 is homogeneous over the trapping area perturbations from heat convection are unlikely. Such non Brownian perturbations can easily be spotted as they lead to slanting of the Gaussian distribution of the sampled position data, especially in the direction of the flow channel parallel to the two fibre ends (along the x-axis). However these effects were not observed in the experimental data (see figure 5.7 (right - above) where a Gaussian shape is maintained). Convective rolls can also be induced due to local heating from the optical field particularly when the sample area is at room temperature. To investigate the absorption and subsequent heating of the laser radiation and the Koehler illumination a drop of DI water was placed on a coverslip. After 30 minutes the temperature was measured with the IR camera (with a sensitivity of $\pm 0.1^\circ\text{C}$) see figure 5.11.

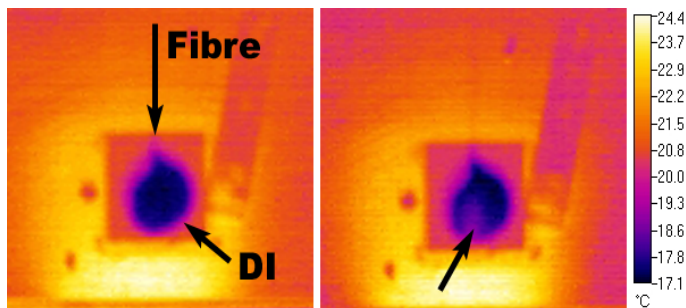


Figure 5.11: Absorption heating of a drop of DI water by 110mW of 1070nm light emerging from a single mode fibre. Left: Picture shows the direction of the single mode fibre, the drop of DI-water is shown in the center of the picture in black at a temperature of 17.4°C . Right: after 30 minutes the water at the vicinity of the fibre has reached a temperature of about 19°C .

100mW of laser power launched from one single mode fibre into the DI water host medium changed the temperature by $\approx 1.6^\circ\text{C} = 1.6\text{K}$. In units of k_bT this is only $1.6 \times 1.38 \times 10^{-23}\text{J/K}^{10}$. For the subsequent measurements this heating effect was treated as minor and not implied in the calculations of the trap stiffness. In some experiments D_2O was used with a even lower absorption coefficient than water.

In addition, no heating effects were observed from the Koehler illumination of the setup, here the water droplet showed no temperature change after 30

¹⁰Where $k_bT \approx 4pN \times nm$.

minutes of illumination under experimental conditions (without laser). Heating effects of the laser can have effects on the sample medium viscosity and on the measured trap stiffness and were found by [80] to be of the order of 2%¹¹ at 100mW for a single beam gradient tweezers with a high NA (NA=1.3) for spheres in water. Contrary to my experiment, the heating effects in water are of the order of $\approx 0.8K$ and differ by a factor of 2 to my findings for two diverging beams with NA=0.14. My results are closer to the findings by [86] of $\approx 1.0 - 1.5K$ (here for all experiments wavelength and laser power are comparable). Still for the lower NA used in in the fibre trap experiment one would expect a lower heating effect as those reported by [80, 86]. Due to the different geometry dual beam versus single beam trap a direct comparison seems not feasible at this stage.

In addition [80] found that the absorption effects of the spheres are minor, so the absorption of the host medium (water) is prominent.

In conclusion more accurate measurements need to be undertaken to draw quantitative conclusions from the experiment. At the present stage the exact temperature can only be approximated and used as a rough verification of the experimentally determined viscosity, via comparison to the temperature given in figure 5.9.

5.2.8 Discussion

First I give an overview of the obtained trap spring constants from the two different measurement methods:

	κ_x x-axis	κ_z z-axis
Equipartition theorem σ	8.95pN/ μm	0.131pN/ μm
Autocorrelation decay time τ	3.77pN/ μm	0.126pN/ μm

Here the disagreement between κ_x from the equipartition theorem and the autocorrelation measurement is quite significant and leads to conclude that the trap stiffness measurement via video analysis starts to break down for too high spring constants. It should be noted that discrepancies between different trap stiffness measurement methods are not uncommon, here a mismatches

¹¹Heating effects decrease the viscosity of the medium so the trap stiffness is overestimated.

of a factor of two has been reported in reference [87] for a single gradient tweezers geometry utilising a quadrant photodiode. In the literature video analysis method has been extensively used to measure spring constants of up to $2pN/\mu m$ [67] for a single gradient tweezers. Here it is worth checking whether the movement of the sphere is sufficiently sampled via the viscous relaxation time which indicates the time scale over which the relaxation after perturbation of the sphere in suspension takes place and is the ratio of viscous drag coefficient and the spring constant. From [65, 67]

$$\tau_{visc} = \frac{6\pi\eta r_{sphere}}{\kappa} \quad (5.15) \quad \begin{array}{l} \gamma = 6\pi\eta r_{sphere} \text{ viscous} \\ \text{drag} \\ \tau_{visc} = \text{viscous relaxation} \\ \text{time} \end{array}$$

In the experiment the viscous relaxation time follows to $\tau_{visc} = 452msec$ and is well above the sampling time of the camera with $\Delta t = 2.6msec$ and also fails to explain the discrepancy between κ_x^σ and κ_x^τ .

However in the following section I am mainly interested in the spring constants along the beam propagation direction for a two sphere array and will determine them via the autocorrelation decay time. To built confidence in the video analysis autocorrelation technique I compared it to a quadrant photodiode (QPD) trap stiffness measurement for a single beam gradient tweezers geometry (see for example [73, 88]). In the following figure 5.12 the spring constants for the video analysis method and the QPD measurements are shown for a single beam gradient tweezers for different light field powers.

In this tweezers geometry the video analysis starts to break down at κ exceeding $20pN/\mu m$. At higher levels of κ the random walk of the sphere is getting too small to be resolved by the video analysis method used. Still it sufficiently captures low trap stiffness as in the present counter-propagating fibre trap along the beam propagation axis (z-axis). This assured that the in subsequent experiments used autocorrelation method gives reliable results for low enough trap powers as in a CP tweezers geometry. However the discrepancy of the spring constants κ_x^σ and κ_x^τ cannot fully be explained at this stage.

Also comparison to trap stiffness values published in the literature [89] for a dual beam fibre trap are not directly applicable to our experiment as different laser sources and fibers were used. However it was worth checking the

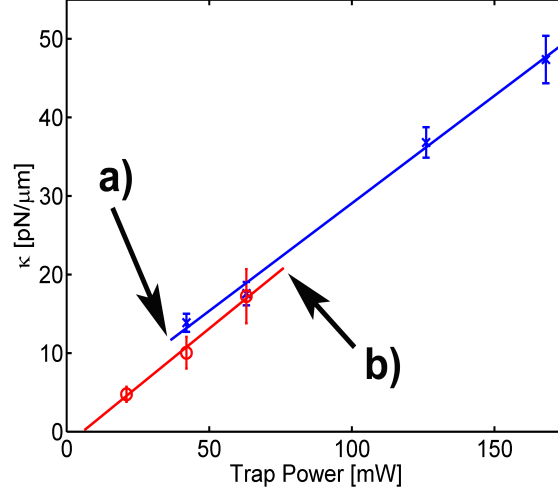


Figure 5.12: Comparison between QPD (blue) and video analysis (red) trap stiffness measurement for a single gradient tweezers at different power levels. The error bars indicate the difference between the two trap axis. Both methods to determine the spring constant have break down point past which meaningful results cannot be obtained: a) indicates the point where the backscattered light onto the the QPD cannot be sufficiently resolved anymore, b) indicates the point past which the sphere motion could not be accurately enough resolved and no meaningful results were obtained for higher trap powers. QPD measurements obtained from Dr. Peter Reece.

results of [89] and [8] with our theoretical model¹²:

Reference	r_{sphere}	κ_z Literature	κ_z Simulation results
[89]	$1.29\mu m$ (silica)	$0.044pN/\mu m$	$0.025pN/\mu m$
[89]	$2.53\mu m$ (silica)	$0.258pN/\mu m$	$0.035pN/\mu m$
[8]	$1.5\mu m$ (polystyrene)	$0.017pN/\mu m$	$0.011pN/\mu m$

For [89] no agreement could be established, as the mode field diameter was not explicitly stated in the publication. The disagreement between the experiment from [89] and the theoretical model is quite significant and a full explanation to whether this is due to incorrect modelling parameters cannot be given at this stage. The results for [8] agree better, however not all parameters were clearly stated and needed to be approximated.

¹²With data obtained from the references: $\lambda = 0.532\mu m$; $P = 22mW$; $\omega_0 = 1.5\mu m$; $D_f = 125\mu m$; $\Delta n = 0.1$ [89]. And $\lambda = 1.3$ and $0.83\mu m$; $P = 7mW$; $\omega_0 = 4.5$ and $2.5\mu m$; $D_f = 200\mu m$; $\Delta n = 0.21$ [8].

In the next section I want to extend the work presented to a two sphere array.

5.3 Investigation of an optically bound two sphere system via Brownian motion

The theoretical models described here have been developed by Prof. Ewan M. Wright and Dr. Michael Mazilu and will be subsequently compared to the experimental findings.

5.3.1 Calculation of the restoring forces

To model the correlated motion between two optically bound spheres I will employ the theoretical approach of Prof. Ewan M. Wright. The model is based on the approach by Meiners and Quake [63] and Bartlett *et al.* [64] and includes the hydrodynamic coupling between the spheres. In this section their hydrodynamic coupling theory is extended to include the optical coupling between two optically bound particles as well.

Two identical spheres are assumed optically bound along the z-axis by a pair of mutually incoherent, but otherwise identical counter-propagating laser fields in a dual beam fibre trap. The spheres of radius r_{sphere} are taken to have an equilibrium separation D , and the deviations of the sphere centres from their equilibrium positions along the z-axis are labelled $z_n, n = 1, 2$. The spheres are assumed to be tightly bound in the plane transverse to the laser propagation axis due to the confinement provided by the Gaussian intensity profiles, and hereafter I concentrate on the longitudinal motions along the z-axis. Then adopting the notation of Bartlett *et al* [64] the Langevin equations of motion for small amplitude sphere displacements can be written in matrix form as

$$\frac{d}{dt} \begin{pmatrix} z_1 \\ z_2 \end{pmatrix} = \begin{pmatrix} A_{11} & A_{12} \\ A_{12} & A_{11} \end{pmatrix} \begin{pmatrix} f_1(t) + kz_1 + \zeta z_2 \\ f_2(t) - kz_2 + \zeta z_1 \end{pmatrix} \quad (5.16)$$

Here $A_{11} = 1/(6\pi\eta r_{sphere})$ and $A_{12} = 1/(4\pi\eta D)$ detail the longitudinal mobilities, η being the viscosity, $f_n(t)$ are randomly fluctuating functions with correlation functions $\langle f_n(t) \rangle = 0$ and $\langle f_m(t)f_n(t) \rangle = 2(A^{-1})_{mn}k_b T\delta(t - t')$,

representing the fluctuating forces acting on the spheres with effective temperature T to account for Brownian noise. The force terms are proportional to the spring constants, where $k \geq 0$ represent the direct force on a chosen sphere when that sphere is displaced while the other sphere is held fixed, and the force terms proportional to ζ describe the cross force that arises on the chosen sphere at its equilibrium position when the other sphere is displaced. Compared to previous studies by Meiners and Quake [63] and Bartlett *et al.* [64] the new ingredient considered here is the cross force term. The cross force coefficient ζ is positive by virtue of the following physical argument: Longitudinal optical binding arises from the fact that the force acting on a given sphere, say sphere 1, is composed of two components along the z-axis, a direct force directed along the positive z-axis from the laser field emanating from fibre 1 which is closest to sphere 1, and a second oppositely directed cross force arising from the counter-propagating laser field emanating from fibre 2, and that is refocused onto sphere 1 by sphere 2 (see figure 5.13 (left)).

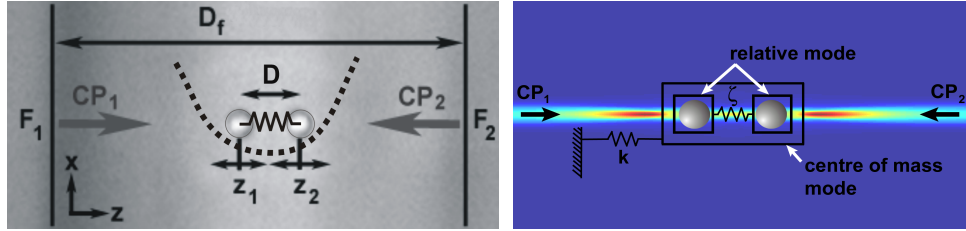


Figure 5.13: Fibre optical trap setup. Left: the two counter-propagating light fields (CP_1 and CP_2) at 1070nm emerge from two single mode fibers (F_1 and F_2) with a separation of the fibre facets D_f . The array is formed in the gap between the two fibers with D being the equilibrium separation of the spheres centres and $z_{1,2}$ indicate small displacements from the equilibrium position of the two spheres along the z-axis. The array center of symmetry ($D/2$) coincides with half the fibre separation ($D_f/2$). The two normal modes of the bound array are highlighted in the graphic: The dashed line represents the potential related to the center of mass motion of the two sphere system. The spring between the two spheres indicates the optical cross interaction between the spheres, the relative motion of them within the system. Right: Here the two normal modes are highlighted: Center of mass $Z_1 = (z_1 + z_2)/2$ from which the cross force constant ζ is determined. The normal mode coordinate $Z_2 = (z_1 - z_2)$ for the relative motion with the direct force constant k .

Balancing of these two forces results in the equilibrium separation for the two optically bound spheres. If sphere 2 is displaced from its equilibrium position and slightly away from sphere 1, then the focus produced by sphere 2 of the field from fibre 2 will likewise be moved away from sphere 1. This implies that the cross force acting on sphere 1 will be reduced in comparison to the direct force, so that sphere 1 will move in the direction of the displacement

of sphere 2, which implies $\zeta \geq 0$. The cross force thus tends to correlate the motions of the two spheres.

To proceed I introduce the normal mode coordinate $Z_1 = (z_1 + z_2)/2$ for the centre of mass motion, and the normal mode coordinate $Z_2 = (z_1 - z_2)$ for the relative motion [64, 63] see figure 5.13 (right). Then applying the same theoretical approach described by Bartlett *et al.* [64] to the above model, the correlation functions ($j = 1, 2$) are found to

$$C_n(t) = \frac{\langle Z_n(t)Z_n(0) \rangle}{\langle Z_n^2(t) \rangle} = \exp\left(\frac{-|t|}{\tau_n}\right) \quad (5.17)$$

where t is the delay time, and the decay times for the center of mass ($n = 1$) and relative ($n = 2$) normal modes are given by

$$\frac{1}{\tau_1} = kA_{11}(1+\epsilon)(1-(\zeta/k)); \quad \frac{1}{\tau_2} = kA_{11}(1-\epsilon)(1+(\zeta/k)) \quad (5.18)$$

Here $\epsilon = A_{12}/A_{11} = 3r_{sphere}/(2D)$, and since the sphere spacing D will be somewhat larger than the sphere radius r_{sphere} where $\epsilon < 1$. Furthermore, stability of the optically bound state require the correlation decay times to be positive, which yields the condition $(\zeta/k) < 1$ for stability. Experimental measurement of the correlation decay times can yield the restoring forces of the optical binding of the two particles around the equilibrium. By dividing the two decay times and rearranging, the ratio of the two spring constants can be obtained

$$\frac{\zeta}{k} = \frac{(1+\epsilon)/(1-\epsilon) - \tau_2/\tau_1}{(1+\epsilon)/(1-\epsilon) + \tau_2/\tau_1} \quad (5.19)$$

Since $\epsilon = 3r_{sphere}/(2D)$ is a known parameter, measuring the normal mode decay times $\tau_{1,2}$ is an *in situ* method of measuring the ratio (ζ/k) of the cross and direct force coefficients, where the direct force coefficient k may then be found using Eq. 5.18. Here the direct force constant clearly plays the role of a trap stiffness. The new element is the cross force term which is an inherently multi-particle effect (illustrated in figure 5.13 as a spring between the spheres), and hence this proposal for a new approach based on the particle correlations is required.

5.3.2 Numerical calculation of the restoring forces

The direct and cross force coefficients can also be calculated theoretically for particles in the Mie size regime using the wave optics approach described in the theoretical chapter A. The implementation of the normal modes into the theoretical numerical model is as follows.

Once a stable equilibrium spacing D for the two spheres is found, a similar code to A is used to calculate the restoring forces for the two normal modes. Here the spheres are placed at their equilibrium separation D , where the acting forces on both spheres are equal to zero. From the equilibrium separation the restoring forces act, when one sphere is displaced from equilibrium.

For small displacement of sphere 1 from equilibrium the total force acting F_n ¹³ with $n = 1, 2$ is calculated. The restoring forces for the two normal modes are resolved as follows (see lower picture in figure 5.14):

- k : the direct force (F1) acts on sphere 1, when sphere 1 is displaced from equilibrium.
- ζ : the cross force (F2) acts on sphere 2 which is held stationary at equilibrium, when sphere 1 is displaced.

From the two slopes of the total force acting versus the displacement of sphere 1 the spring constants ζ and k of the two sphere system can be determined (see upper graph of figure 5.14).

Two approximations are made with this method to calculate the spring constants of the two sphere system, which are clearly visible in figure 5.14:

- The calculation of the equilibrium separation D where the forces acting on the spheres are zero has not a high enough accuracy level. This results in an offset of the zero intersection of the two lines fitted to the restoring forces (see graph in figure 5.14).
- Due to the fit of the restoring forces to a line I am assuming a parabolic potential of the normal modes. This is in agreement with the experimental analysis where the autocorrelation decay time is used to determine the spring constants. However in graph 5.14 it is clearly visible that the potential is of more complex shape and the linear fit is only a first order approximation.

¹³Where F_n the force acting on the sphere is composed out of the difference between the forces from the counter-propagating fields ($F_{CP1} - F_{CP2}$).

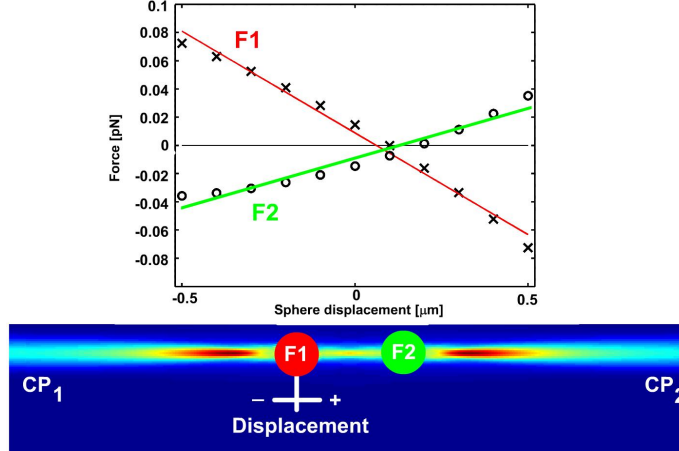


Figure 5.14: The graph shows an example calculation of the direct k and cross ζ spring constants on a two sphere system with a separation $D = 7.65\mu\text{m}$. In the numerical model sphere 1 is getting displaced by $\pm 0.5\mu\text{m}$ and sphere 2 is kept stationary (see bottom graphic). The forces acting on each sphere F_1 on sphere 1 and F_2 on sphere 2 are calculated. The intensity distribution of the two CP fields are shown as an underlaid false colour plot. From the slope of the acting restoring force versus the displacement of sphere 1 the spring constant can be read of.

At the present stage of the numerics, these approximations should however be sufficient to give a first order indication of the restoring forces of the system.

Next I want to extend the equation of motion of one sphere in a potential to an interacting two sphere system.

5.3.3 Equation of motion for a two sphere system

To theoretically simulate the motion of the system due to Brownian fluctuations, I am following the approach described in the previous chapter, based on references [67, 64]. Where the equation of motion for the modes, for simplicity is defined as $Z_I = (z_1 + z_2)$ and $Z_{II} = (z_1 - z_2)$, and can be written (with $k = I, II$) analogous to formula 5.2 as

$$\frac{\partial Z_k(t)}{\partial t} = -\frac{Z_k(t)}{\tau_k} + F_k(t) \quad (5.20)$$

Where initial terms have been neglected as the experiment is in a low Reynolds number regime. The restoring forces on the modes are described

by the autocorrelation decay times which follow from formula 5.18 to,

$$\begin{aligned}\tau_I^{-1} &= (k - \zeta)(A_{11} + A_{12}), \\ \tau_{II}^{-1} &= (k + \zeta)(A_{11} - A_{12})\end{aligned}\quad (5.21)$$

The autocorrelation decay time incorporates in this case the hydrodynamic and optical coupling of the light-sphere system which is immersed in a host liquid.

The response of this coupled system is probed by Brownian noise $F_k(t)$. Due to the choice of the modes the noise sources are independent of each other for each mode. The modes are also coupled via the mobilities¹⁴ λ_k [64], which are consequently dependent on the distance (D) between the two spheres and their viscous drag coefficient via $\lambda_1 = (A_{11} + A_{12})$, $\lambda_2 = (A_{11} - A_{12})$. The Brownian noise sources can then be described as

$$\begin{aligned}\langle F_k(t) \rangle &= 0, \\ \langle F_k(t)F_l(t') \rangle &= 4\delta_{kl}\lambda_k k_b T \delta(t - t')\end{aligned}\quad (5.22)$$

Where $F_k(t)$ is a Gaussian random variable sampled at discrete times Δt [67] with a mean value of zero and variance of

$$\sigma_k^2 = 2k_b T \lambda_k \tau_k \left[1 - \exp\left(-\frac{2\Delta t}{\tau_k}\right) \right] \quad (5.23)$$

From 5.20 the movement of the modes [67] for discrete times can now be described by

$$Z_k(n) = \exp\left(-\frac{\Delta t}{\tau_k}\right) Z_k(n-1) + F_k(t) \quad (5.24)$$

Where n is an integer addressing the discrete sampling points with spacing Δt . With this I am well equipped to numerically calculate Z_I, Z_{II} and hence z_1, z_2 . Furthermore the previously defined normal mode coordinate

¹⁴They describe the hydrodynamic coupling or interaction between the spheres.

$Z_1 = (z_1 + z_2)/2$ for the centre of mass motion, and the normal mode coordinate $Z_2 = (z_1 - z_2)$ can be obtained and directly compared against the experimental results. It is noteworthy that the factor $\frac{1}{2}$ in the centre of mass mode does not play a role for the simulation of the autocorrelation function as it is normalised.

5.4 Experimental and theoretical results in the bistable regime

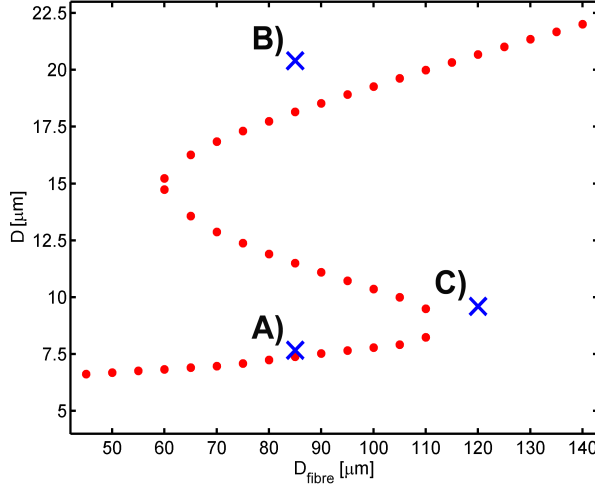


Figure 5.15: In the following section three experimental data points (blue crosses) are discussed marked A) to C). The red dots represent the theoretical simulation of the sphere separation (D) for a varying fibre separation.

The following experiments were carried out using an array of two $3\mu m$ diameter spheres, a fibre separation $D_f = 85 \pm 2\mu m$, and an output power of $110mW$ emerging from each fibre. Here the local viscosity of the monodisperse mixture of $3\mu m$ silica microspheres in DI water was probed as described in the previous section. The sample was heated to $\approx 40^\circ C$ which gives a measured viscosity of $\eta = 0.61$ and from figure 5.9 of $\eta = 0.67$. These values are reasonably close, for the subsequent experimental analysis the experimentally determined viscosity of $\eta = 0.61$ was used.

For this fibre separation the array exhibits bistability, shown in the following

figure 5.15 A) and B). As well I am going to take a look at the pre-transition behaviour past the lower switching point at $D_f = 120 \pm 5\mu m$ marked as C). In the following sections I would like to address each of the measurement points separately:

5.4.1 A) small sphere separation

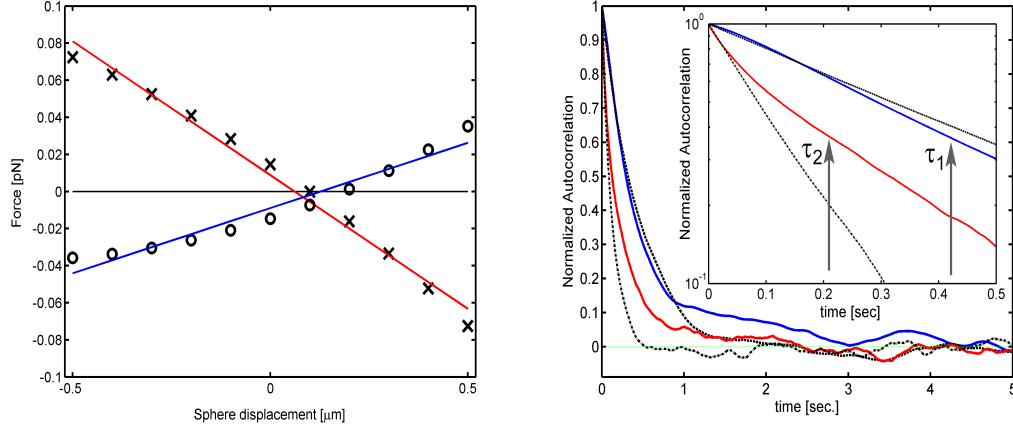


Figure 5.16: Left: theoretical prediction of the direct (crosses) and cross (circles) force from the theoretical model. Right: Experimental autocorrelation measurements for the both normal modes (red, relative motion (Z_1); blue, centre of mass (Z_2)). The inset shows the log plot of the autocorrelation for a smaller time scale, the arrows mark the decay times. The dotted black lines are the theoretical results from the equation of motion model with the experimentally found spring constants.

The experimentally observed value of the averaged centre to centre separation (D) of the array of $7.67\mu m$ is in acceptable agreement with the theoretical value of $7.38\mu m$. By reading the normal mode decay times $\tau_{1,2}$ from the data as the delay times at which the autocorrelations drop to $1/e$, which occurs for delays less than 0.5 seconds, we obtain $\tau_1 = 0.42$ seconds and $\tau_2 = 0.21$ seconds (marked in the right inset figure 5.16 with arrows). Using Eq. 5.19 the experimentally determined ratio of the cross and direct force coefficients $(\zeta/k) = 0.566$, in comparison to the theoretical value of $(\zeta/k) = 0.559$, and using equations 5.19 and 5.18 we find $k = 0.104pN/\mu m$ experimentally, in contrast to the theoretical value of $k = 0.172pN/\mu m$. Utilising the Brownian motion model with the experimentally determined spring constants we can simulate the system response of the two spheres. The autocorrelation for both simulated modes is shown in the above right hand figure 5.16 as black lines, we find a theoretical value for $\tau_1 = 0.47$ seconds and $\tau_2 = 0.13$ seconds. As well as the spring constants to $(\zeta/k) = 0.567$, and $k = 0.132pN/\mu m$ (the respective numerical results are plotted in the above figure 5.16 in black).

In the following two graphs (figure 5.17) the joint probability is plotted for z_1 and z_2 (left: theoretical; right: experimentally false colour plot with bin

sizes of $0.05\mu m$). Figure 5.17 clearly shows that the motion of both spheres

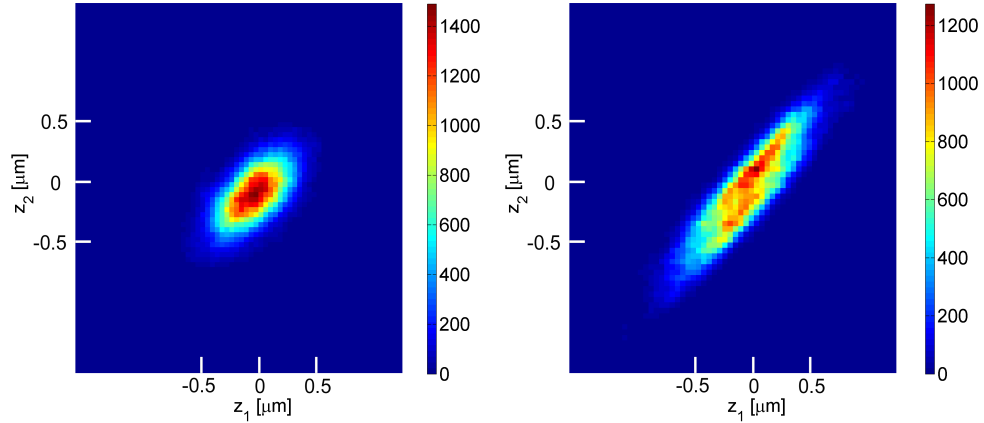


Figure 5.17: Left: Theoretical prediction of the joint probability of z_1 vs. z_2 . Right: Experimentally measured joint probability with a bin size of $0.05\mu m$ and a data set of 20000 measurements for experiment and theory. Both images have a positive sloped bias indicating the direct correlation of the individual sphere positions.

is directly correlated, here the concept of optical binding is validated one sphere moves and the other one slaves the movement due to the coupling of the light fields.

Although the equation of motion model gives a qualitative agreement with the experiment it fails to predict the exact distribution width by a factor of two.

5.4.2 B) large sphere separation

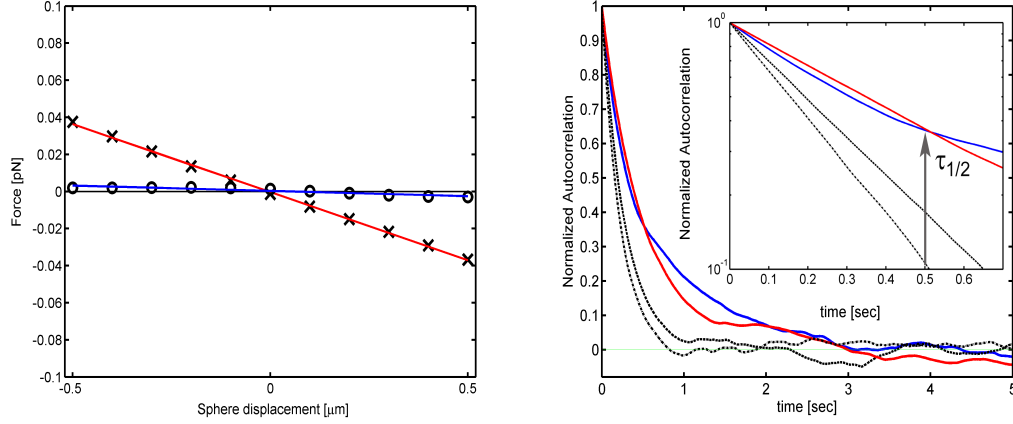


Figure 5.18: Left: theoretical prediction of the direct (crosses) and cross (circles) force from the theoretical model Right: Experimental autocorrelation measurements for the both normal modes (red, relative motion (Z_1); blue, centre of mass (Z_2)). The inset shows the log plot of the autocorrelation for a smaller timescale, the arrows mark the experimental decay times. The dotted black lines are the theoretical predictions from the equation of motion model with the experimentally found spring constants.

Here the experimentally observed value of the averaged center to center separation of the array of $20.54\mu m$ is within 10% agreement with the theoretical value of $18.15\mu m$. Here a higher disagreement is not unexpected if compared to the results of figure 3.5 where a higher fluctuation is observed for the upper branch of the bistable curve. The normal mode decay times are obtained to $\tau_{1,2} = 0.5$ seconds (marked with an arrow in the right hand figure 5 inset). The experimentally determined ratio of the cross and direct force coefficients $(\zeta/k) = 0.093$, in contrast to the theoretical value of $(\zeta/k) = 0.096$, and $k = 0.078 pN/\mu m$ experimentally, in comparison to the theoretical value of $k = 0.074 pN/\mu m$. From the Brownian motion model we find a theoretical value for $\tau_1 = 0.28$ seconds and $\tau_2 = 0.23$ seconds and respectively to cross check the spring constants to $(\zeta/k) = 0.107$, and $k = 0.155$ (the respective numerical results are plotted in the above figure 5.18 in black). In the following two graphs (figure 5.19) the joint probability is plotted for z_1 and z_2 (left: theoretical; right: experimentally false colour plot with bin sizes of $0.05\mu m$).

Interestingly the joint probability plots show a random correlation. Here the physical picture of optical binding does not hold anymore although both spheres influence each others position and keep each other apart their mo-

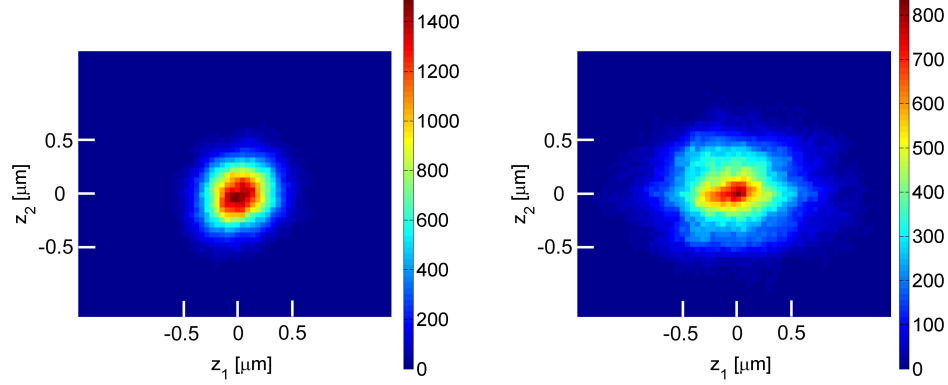


Figure 5.19: Left: Theoretical prediction of the joint probability of z_1 vs. z_2 . Right: Experimentally measured joint probability with a bin size of $0.05\mu m$ and a data set of 20000 measurements for experiment and theory. Both images indicate random correlation between the individual spheres positions, as the distributions are of circular shape.

tion is no longer correlated. With a large separation of $20.5\mu m$ between the spheres hydrodynamic interactions [63, 64] are becoming less prominent. Most importantly the optical fields past each sphere, which correlates the spheres motion for the small separation are divergent again. The focus past the sphere is at $f = r_{sphere}/\Delta n \approx 8.4\mu m$ which means that the second sphere resides now approximately $12\mu m$ past the focus of its neighbour. Contrary to a small sphere separation, with $D = 7.4\mu m$, where the sphere resides slightly before the focus of its neighbour. Now each sphere seems to sit in its own optical potential and the interaction between both spheres has vanished or decreased beyond the level of the experimental measurement accuracy. This however could not be verified with an increased sample set or a higher sampling rate using the numerical random walk model, here simulations indicated a persistent random correlation.

5.4.3 C) transition point

At the transition point no stable position was found utilising the paraxial approximation model, however from figure 3.10 it follows that transitions in a dynamically driven system can occur far past the predicted transition point as the potential map is very shallow. Here I investigate the pre-transition behaviour at $D_f = 120 \pm 5 \mu m$ fibre separation. Theoretically no stable position was found, however experimentally a dwelling time of up to 22 seconds (approx. 9000 data points) at an averaged sphere separation of $9.64 \mu m$ was achieved, before the array expands from a small to a large separation. The joint probability distribution is shown in the following figure 5.20 with a decreased bin size of $0.1 \mu m$, this was necessary as a decreased dwelling time allowed measurements of only 9000 data points.

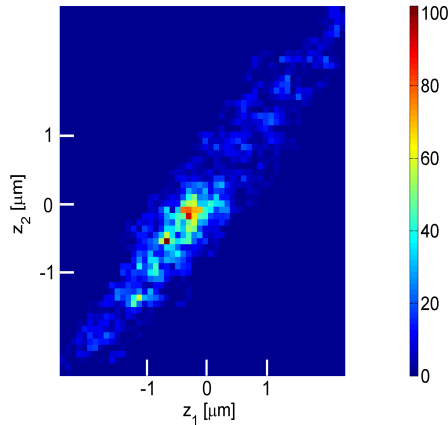


Figure 5.20: Experimentally measured joint probability with a bin size of $0.1 \mu m$ and a data set length of 9000 data points. At the lower transition point the joint probability still indicates a direct correlated sphere motion.

It is observed that the sphere motion is still correlated. Interestingly the standard deviation (STD) of the normal modes has significantly increased $STD_1 = 1.15 \mu m, STD_2 = 1.0 \mu m$ in comparison to a representable data set at point A) with $STD_1 = 0.39 \mu m, STD_2 = 0.17 \mu m$. At the transition points the spheres tend to want to break apart to minimise the free energy by switching to the deeper potential, causing the STD to increase.

5.5 Discussion

In both figures 5.17 and 5.19 the theoretical simulation of the joint probability distribution shows a disagreement of the distribution width for $z_{1,2}$ of about a factor of two. By changing the sampling rate from $400Hz$ to $1kHz$, this discrepancy can be eliminated for both cases. Experimentally a higher sampling rate was not feasible due to the limited frame rate of the camera. The theoretical discrepancy can be also eradicated by increasing the sampling time by a factor of 10. Experimentally these high integration times were not reached as the setup process of the integrated trap did not permit to maintain a clean sample medium. So during long measurement processes dirt accumulated in the array, changing the sphere separation and the system dynamics. A cross check with half the sample set size gave a change of the measured force constants to $< 10\%$ which should suffice a reasonable sampling accuracy. Here no conclusion can be easily drawn to whether the experiment is under sampled.

A work around to this problem is to increase the trap stiffness to shorten the integration time of the experiment, here one can either change the refractive index difference Δn , increase the optical power emerging from the fibers or decrease the fibre separation. In the next section I will move on to describe experiments with a decreased fibre separation D_f ¹⁵.

5.6 Experimental and theoretical results in the linear regime

The following experiments were carried out using an array of two $3\mu m$ diameter spheres, a fibre separation $D_f = 50 \pm 2\mu m$, and an output power of $110mW$ emerging from each fibre. The experimentally observed value of the averaged center to center separation (D) of the array of $6.7\mu m$, is in acceptable agreement with the theoretical value of $6.9\mu m$. The experimentally measured correlation functions are shown in figure 5.21 (right), and show the expected decay with increasing delay time. The non-exponential decay evident for delays larger than 0.5 seconds is due to sampling issues related to the finite size of the data sets and are similar to that reported in [65]. By

¹⁵Higher powers were not feasible with the experimental setup as heating effects of the fibre tip in the coupling setup leads to drift in the coupling efficiency. Increasing Δn was not investigated as the paraxial approximation would not hold for polystyrene spheres.

varying the data set size it was ensured that results for delays less than 0.5 seconds are robust against variations.

By reading the normal mode decay times $\tau_{1,2}$ from the data as the delay times at which the autocorrelations drop to $1/e$, which occurs for delays less than 0.5 seconds, $\tau_1 = 0.26$ seconds and $\tau_2 = 0.14$ seconds is obtained. The experimentally determined ratio of the cross and direct force coefficients $(\zeta/k) = 0.57$, is in contrast to the theoretical value of $(\zeta/k) = 0.77$, $k = 0.29pN/\mu m$ experimentally, in comparison to the theoretical value of $k = 0.31pN/\mu m$. Thus, acceptable agreement between the theory and experiment for the optical forces acting on the two particles in the optically bound array is achieved.

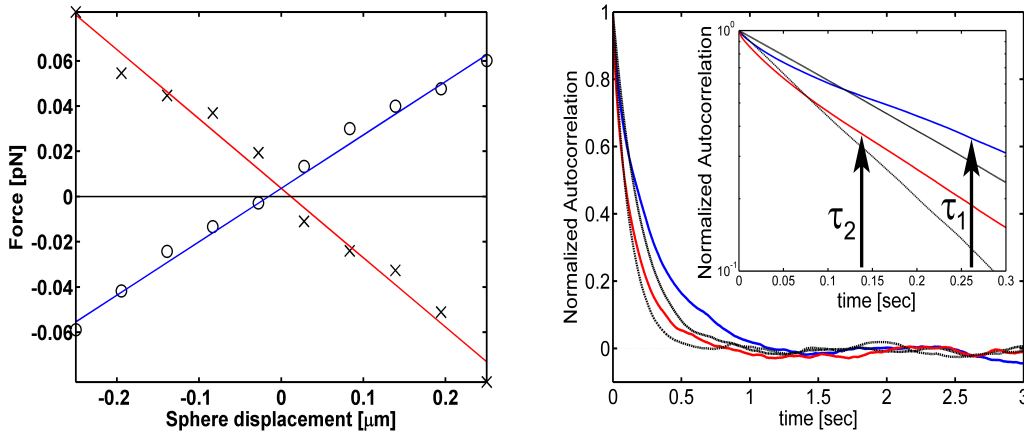


Figure 5.21: $3\mu m$ 2 sphere array with a fibre separation of $50\mu m$. Left: theoretical prediction of the direct (crosses) and cross (circles) force from the theoretical model. From the slope of the linear fit the coefficients for ζ/k can be deduced to $k = 0.31pN/\mu m$ and $\zeta = 0.24pN/\mu m$ respectively. Right: Experimental autocorrelation measurements for the both normal modes (red, relative motion (Z_1); blue, centre of mass (Z_2)). The inset shows the log plot of the autocorrelation for a smaller timescale, the arrows mark the experimental decay times.) Averaging over 25 consecutive data sets for the center of mass normal mode (dashed line) yielding $\tau_1 = 0.26sec$, and relative normal mode (solid line) giving $\tau_2 = 0.14sec$. The dotted black lines are the theoretical predictions from the equation of motion model with the experimentally found spring constants.

5.7 Conclusion and discussion

In conclusion, I have demonstrated the utility of measuring particle correlations as a means of measuring the optical forces acting within an optically

bound array. The agreement between the measured optical forces and numerical simulations for particles in the Mie size regime is adequate considering the approximated nature of the model. Measuring the optical force coefficients means that the full linear response of the optically bound system around its equilibrium, encapsulated in equation 5.16, is now attained so that one may now explore the response of the system to external modulations using e.g. external tweezers. The results are also an important step towards exploring the nonlinear response of optically bound arrays for large amplitude modulations.

Part of the discrepancy between experiment and theory can be due to residual standing wave effects, caused by backreflections of the incident wave from two interfaces. Here two sources of backreflections can be distinguished for one beam a) from the surface of the second sphere and b) when the beam has exited the array from the opposing fibre surface, both are shown in figure 5.22.

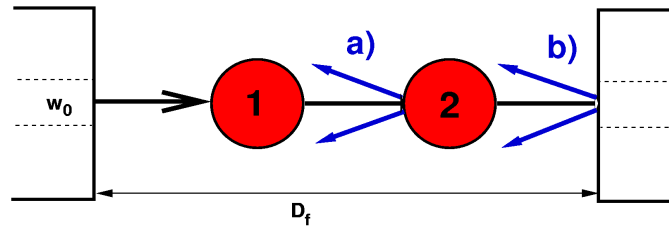


Figure 5.22: Standing wave effects in an optically bound array of two spheres (1 and 2). Two sources of backreflections are highlighted: a) the incident field (black) is getting refocused on the second sphere and reflected (blue). Here the incident field and the backreflected field from the sphere interfere. b) The field that is exiting the array is getting backreflected by the second fibre. Both sources create standing waves of the incident field with itself.

Backreflections from the opposing fibre surface are subtle and come into effect when the fibre separation D_f is small. They can be easily eradicated, by cleaving the fibers at an angle of 8 to 12° degree or antireflection coating the fibre ends. Both of these approaches have been realised in the experiments presented in this chapter.

More troublesome are the backreflections from the spheres themselves, which lead to discrete preferred dwelling positions that are spaced by $\frac{1}{2}\lambda/n = 403nm$ (in DI water) as shown in figure 5.23. These observations go in unison with theoretical findings by [90] for backreflections from a water-glass

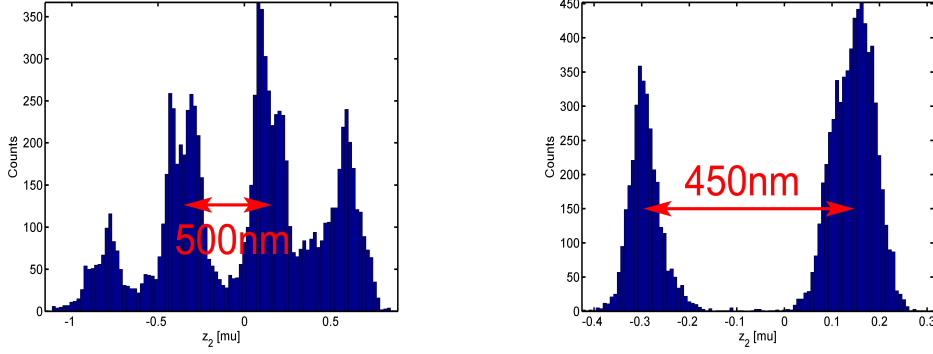


Figure 5.23: Interference effects from the nearest neighbour in an array, affecting the distribution of the sphere positions along the field propagation axis. Left: $3\mu\text{m}$ sphere position distribution (z_2) with a spacing of $\approx 500\text{nm}$ at a fibre separation of $D_f = 80\mu\text{m}$. Right: $5\mu\text{m}$ sphere position distribution (z_2) with a spacing of $\approx 450\text{nm}$ and a fibre separation of $D_f = 50\mu\text{m}$. Both measurements were taken at an optical power of 110mW from each fibre.

interface with reflections as low as 0.4% and in optical binding [91].

Although the backreflected intensity is low in magnitude the exerted force scales with the gradient of the intensity $F \propto \nabla I$, which can be large in interference patterns. Karasek [91] found that the actual potential depth lies at the order of $0.5k_B T$ (where $\Delta U = 0.002\text{pN}/\mu\text{m}$ at room temperature).

Here I want to briefly discuss several trails to dampen the effects of the interference effects on the array, by raising the trap temperature and with a different sphere size.

A raised trap temperature to increase the Brownian motion has little effect on the optical potential itself and would hardly effect the interference effects, which is shown in the following simple calculation, from Boltzmann statistics and formula 5.10. For the different stable positions the probability to find a certain sphere configuration follows to:

$$1 = N * \exp\left[-\frac{U_1}{k_B T}\right] * \exp\left[-\frac{U_2}{k_B T}\right] * \exp\left[-\frac{U_3}{k_B T}\right] \quad U = [Nm] \quad (5.25)$$

where U_N with $N = 1, 2, 3$ donates the different solutions. The optical potential for U_1 (see figure A.7), which follows from formula A.26 to $U_1 \approx -0.6\text{pN}\mu\text{m}^{16}$. From which, with $k_B = 1.38 * 10^{-23}\text{J/K}$, the fraction

¹⁶For $90\mu\text{m}$ fibre separation for the first stable position.

follows to $\frac{0.6 \cdot 10^{-18}}{1.3 \cdot 10^{-23} \cdot T}$. Here the temperature T has to be of the order of 10^5 to influence the optical potential. Hence an ambient temperature change will have hardly any effect on the optical potential. For example a change in temperature $\Delta T = 30^\circ$ raises the potential by only $\Delta U = 0.0004 pN/\mu m$. This was experimentally verified as discrete dwelling places were occasionally observed in the experiment.

One would also expect that a large sphere size possibly of the order of $D_{sphere} = N \times \frac{1}{2} \lambda / n_{host}$ will average over those interference patterns, but spheres with a mean diameter of $3.22 \mu m$ ¹⁷ from BANGS laboratories were found to have a too broad size distribution, which did not allow to obtain meaningful experimental results.

As the above mentioned attempts failed to inhibit the interference effects, experiments which showed discrete sphere dwelling places were not used in the experimental analysis presented here.

The standing wave effects were not captured by the implemented theoretical model as backreflections are neglected in the paraxial approximation and more refined modelling has to be implemented to fully capture them.

At this stage of the experiment and theoretical modelling no solid conclusion can be drawn on the influence of these interference effects on optical binding and could be the focus of future research.

¹⁷Which came closest to fulfill the criterion in DI water.

Chapter 6

Observation and simulation of an optically driven micromotor

6.1 Introduction

Miniaturisation has seen a rapid development since Feynman's talk *There's Plenty of Room at the Bottom* in 1959 [92] and has now spawned into many fields of research ranging from microcomputers to Lab-on-chip (LOC) devices. Such LOC's are used to perform manipulation and analysis of chemical or biological substances. It is envisioned to perform experiments that were traditionally carried out on a macroscopic sample in a laboratory on a minute volume of analyte on a microfluidic chip. A particular interest lies in microfluidic flow channels (where one dimension is of the order of 1 to 100 microns) to transport small amounts of analyte. In the realm of microfluidics one however is challenged with low Reynolds number, laminar flow where no turbulent mixing occurs. One has to rely on diffusion for mixing with the drawback of long time spans for the mixing to take place. Here engineers are challenged with the need to find methods to enhance this diffusion process to mix as well as pump and move minute amounts of analyte by means of micromachines that are mechanically actuated.

Interestingly micro devices performing such actuation can be initiated by means of light-matter interaction. Light induced forces and torques are exerted on such micromachines, that are then driven by the optical gradient or scattering force. Different driving geometries can be realised to harness the light induced force. For example the scattering force enables micromo-

tors to be operated in a tangential setup where the micromotor rotors are in line with an optical waveguide. This operational geometry has the advantage that it reduces the complexity of the driving of such a device in a microfluidic environment by delivering the actuating light by means of a waveguide (as shown in figure 6.1) or fibre optic.

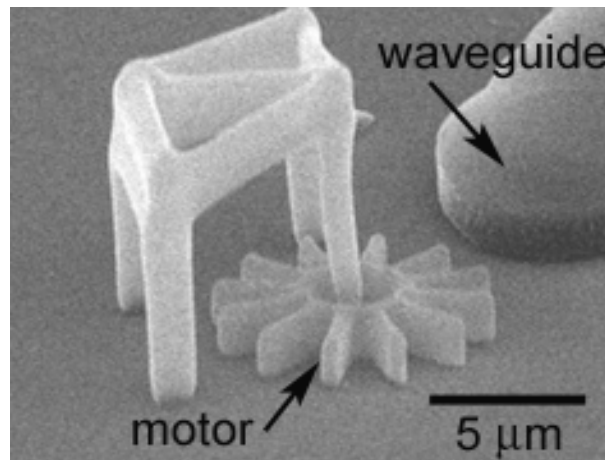


Figure 6.1: Scanning electron micrograph of an integrated optical motor. The driving light is delivered via a waveguide. Picture obtained from Dr. Lorand Kelemen.

In this chapter I want to explore the case of a micromotor, as shown in figure 6.1, being driven by a fibre optically delivered light beam. The aim is to test the possibility of applying the developed paraxial model, used throughout my thesis to calculate the acting forces in an optical bound array, to predict the rotation rate of a micromotor actuated by light-matter interaction. Here the challenge lies in modelling an arbitrarily shaped object interacting with light. An applicable model would further open up means to enhance the performance of such a device through simulations. One key question in applying the paraxial approximation to calculate the forces and subsequent the torque acting on such a device is the direction of scattering, for backscattered light one would expect the paraxial approximation to fail (as discussed in the appendix A.5.2). This issue will be addressed by utilising the two-photon technique developed in the previous chapter to visualise the direction of light scattering by the rotating micromotor.

6.1.1 Actuating micromotors with light

Ever since 1986 when they were first demonstrated by Ashkin [93] optical tweezers have rapidly developed into a research tool, giving physicists and biologists the possibility to control micron sized objects. Importantly they are no longer just used to move particles in three dimensions, optical tweezers have furthermore become a valuable tool to align and rotate microparticles. If sufficient torque is generated such tweezers can be used to create pumps [94, 95] and valves [96, 97] for Lab-on-Chip applications.

Such rotational actuation via light-matter interaction can be achieved in three different ways, distinguished by the harnessed force.

6.1.2 Transfer of angular momentum

The first group of micromotors relies on the transfer of angular momentum, that is intrinsic in the incident light beam. A beam of light can have both Orbital Angular Momentum (OAM) and Spin Angular Momentum (SAM) linked with the phase structure and polarisation respectively. The transfer of OAM was used by Ladavac *et al* [94] to rotate a ring of trapped microparticles and displace colloids in a liquid.

When circularly polarised light is used to trap a birefringent particle the transfer of SAM from the light to the particle can result in a rotation rate of up to a few hundred Hertz [98]. On the other hand a birefringent particle will experience a torque from the transfer of OAM in a circularly or elliptically polarised beam. The operation principle here is the light passing through a birefringent material will experience a change of its polarisation state and the associated SAM. This change in angular momentum results in a torque being exerted on the birefringent particle, making it spin. Such a pump system was realised by Leach *et al* [95] where two birefringent particles were counterrotated by using SAM transfer from two oppositely circularly polarised beams. However not arbitrary shapes such as gears can be realised with birefringent crystals, here Neal *et al* [99] demonstrated that engineered form-birefringent can be harnessed as well to operate a microgear via SAM. Part of such an motor consists out of an 1 dimensional photonic crystal which can be engineered to exhibit birefringence. Importantly such motors can be rotated in a discrete fashion by a stepwise control of the polarisation state of the light. Micromotors harnessing the angular momentum of light are held in place by the optical gradient force of the driving light beam, which can also be used

as a driving mechanism.

6.1.3 Gradient force

An asymmetric particle can be rotated by the optical gradient force with a rotating light pattern [100]. The principle of this idea has been demonstrated [101] but has at the present stage not yet been applied to any specific applications. Here the aim was to create an optically driven micropump. Also Terray *et al* [96] reported peristaltic pumps using time-shared optical traps, in which multiple particles were scanned in a flowchannel by means of a beam steering mirror. Here the peristaltic motion of the particles initiated the fluid flow.

6.1.4 Scattering force

The third group of motors use the scattering of light as an actuation mechanism [102, 103], importantly the rotors need to be of appropriate shape [104]. Light diffraction or scattering by a micro object in the Mie regime on the other hand opens up an alternative solution for exerting a suitable torque on a micromotor as the operating light can be delivered by means of standard waveguides [102] or fibre optics. However this involves the careful design of such micromotors and layout of the driving light geometry to gain maximum performance of such systems. In this context it is of great importance to study the light diffraction from such a motor to investigate and understand its driving mechanism.

Here I investigate the diffraction from an optical micromotor and its rotation due to optical scattering. Experimentally by utilising two-photon imaging it is possible to visualise the diffracted light from the micromotor. Previously two-photon imaging has been used as a method to visualise the reformation of Bessel light beams [51, 52]. The numerical model developed to calculate the diffraction of a beam by a sphere in the previous chapter is modified to theoretically predict the observed diffraction pattern from the micromotor. This demonstrates a simple but powerful method to predict diffraction patterns of arbitrarily shaped micro objects within the constraints of the paraxial approximation. I shall present experimental and theoretical results for a micromotor being driven by the scattering force of light delivered by an optical fibre, as illustrated in figure 6.2.

The theoretical model predicts the torques on such a system and enables to

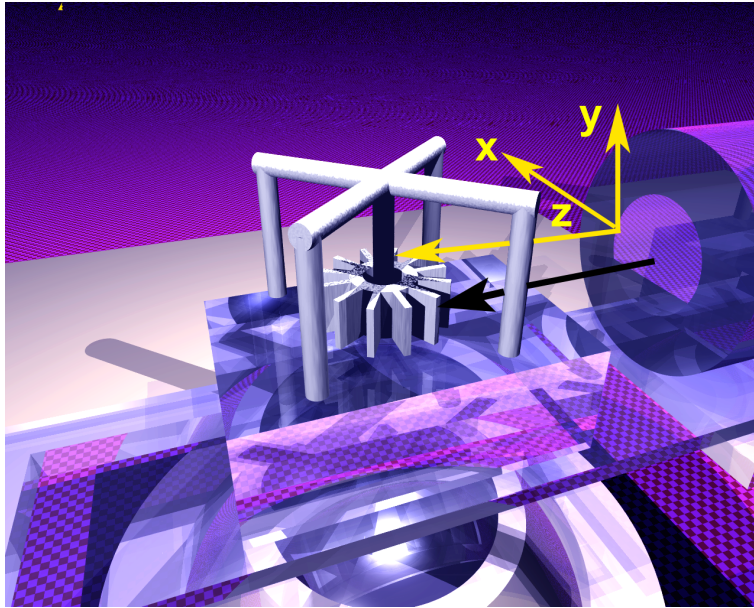


Figure 6.2: 3D image of the micromotor setup. The $10\mu m$ micromotor is held in place by a pole structure. The operating light is delivered via fibre optics (shown on the right hand side). The operation principle is similar to a water wheel, where an off center water-stream interacts with the spokes of the wheel.

carry out a theoretical performance analysis of the gear design, the layout of the light source-motor system and indeed even perform optimisation of the micromotor geometry. Firstly I want to describe the theoretical model used and then progress to discuss the experiment and data acquired.

6.2 Theoretical model

The theoretical model comprises of a monochromatic laser field of wavelength λ propagating along z and originating from a single mode fibre, shown in figure 6.3.

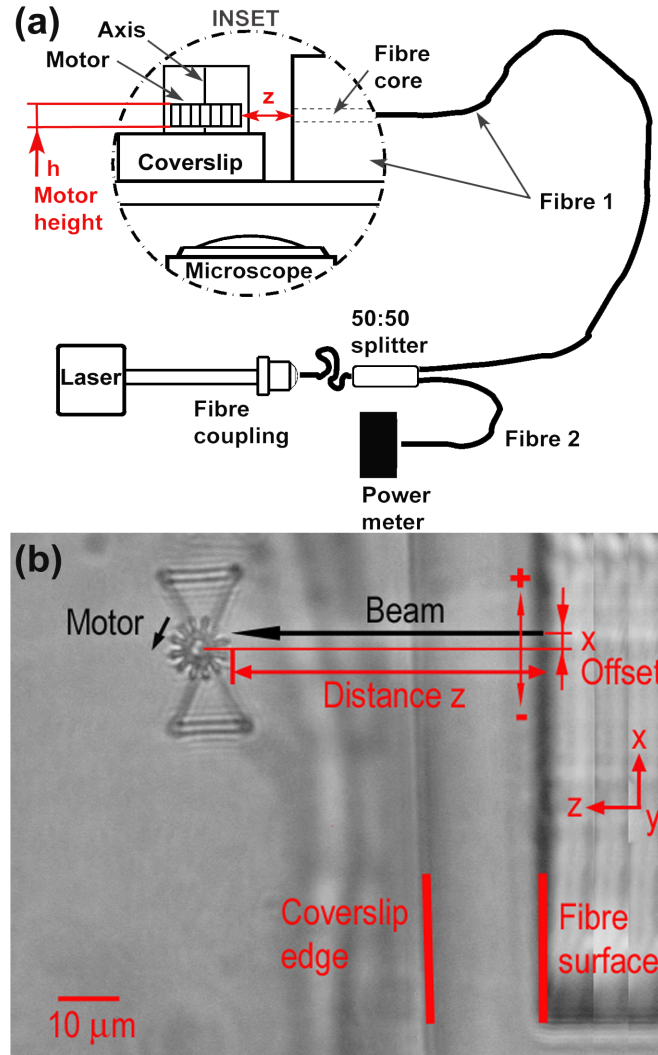


Figure 6.3: (a) The set-up consisted either out of a femtosecond Ti:Sa laser for the visualisation of the light field distribution or an Ytterbium laser for the motor rotation rate experiments. The light of either laser was coupled into a fibre and split via a 50:50 splitter into equal parts (for the Ti:Sa visualisation experiment no splitter was used as the power was left constant). The light in fibre 1 was used to drive the motor whereas the light in fibre 2 was monitored via a power meter. The inset shows a not to scale side view of the experiment which was observed from underneath with a microscope and a CCD camera (see, (b)). The motor is levitated by a coverslip to be inline with the core of the fibre and hence with the emerging light field. The propagation distance z of the field emerging from the fibre is marked. For the theoretical calculations I assume the motor of $2\mu\text{m}$ height (h) to be centred in the beam emerging from the fibre. (b) Topview brightfield image of the experimental setup. The micromotor with supporting pole structure is shown in the upper left side of the image. The motor is fabricated on top of a microscope coverslip slide (the edge of which is shown in the picture) to compensate for the $60\mu\text{m}$ thick fibre cladding. On the right the fibre end facet is shown from which the laser field emerges in the positive z -direction with z being the distance from the fibre surface to the motor. The fibre is offset from the micromotor centre (the axis of revolution) by x to allow the field to interact with the motor spokes. The beam direction is shown in the image. The positive offset in x would make the motor turn counter clockwise as indicated.

The beam waist is located at the end facet of the fibre and separated by a distance z from the outer rim of the micromotor. To give an uneven momentum distribution the centre of the beam is offset by x from the axis of rotation of the motor, where the sign of x denotes from which side the motor is driven causing either an anticlockwise (+) or clockwise (-) rotation of the motor (see figure 6.3 (b)). The field is modelled as a Gaussian beam emerging from the fibre facet with spotsize w_0 and power P . It interacts with a micromotor of refractive index $n_c = 1.62$ (material SU8, approximated to a wavelength of $1070nm$) immersed in a host medium (de-ionised (DI) water) of refractive index $n_h = 1.33$. The micromotor is assumed to be centred vertically in the beam (with $y=0$) and to have a height h . Notably, this method allows for simple and fast micromotor geometry evaluations as any geometry can be realised. Applying the paraxial wave theory [18] and equation A.10 it is possible to calculate the evolution of the optical field $\mathcal{E}(x, y, z)$ distorted by the refractive index variation represented by a binary image of the motor¹. Where the colour white refers to n_c , the pixel determine the grid resolution of the propagation in z and x and can be scaled accordingly with the binary picture of the micromotor. An example is shown in figure 6.4.

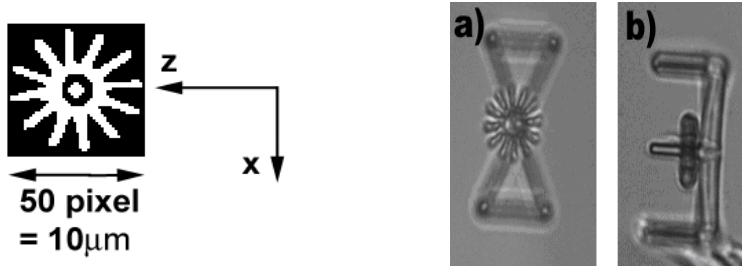


Figure 6.4: Left: Binary image of the motor in the model, the pixel size of the image was normalised to represent the actual motor size. In the model the motor was located at a position z from the beam waist (located at $z=0$) and could be offset from the central beam propagation axis (in the figure the beam is entering the motor from the right hand side) by x . Where $x=0$ would donate the beam is aimed at the middle of the binary image. Right a) top view of the pole structure with motor and b) side-view.

Previous studies have used the ray optics model [105, 106, 107], with different driving geometries. Both ray optics and paraxial wave theory are approximated approaches which can give sufficient accurate results when used in the appropriate circumstance. In this chapter I want to focus on the paraxial approximation as I assume that the main driving mechanism for the micromotor

¹Here a real microscope image of the micromotor was used for the simulations.

investigated is forward scattering of light. Here I utilise my experience in optical binding where the paraxial approximation has been successfully applied to model light matter interaction in the Mie regime (where the wavelength is magnitudes smaller than the object).

In contrast to the ray optics approach the paraxial approximation does not take polarisation effects into account, which are averaged in the calculations and considering that the fibre used is not polarisation maintaining I believe this as a valid approximation. Additionally the paraxial approximation used in this work is well tailored for a waveguide or fibre optics driving geometry where (in contrast to [107]) weak diverging fields are harnessed to operate the motor.

I calculate the intensity distribution by modelling the field as pill-boxes for the experimentally determined motor position (x, z) . The camera observed fluorescence signal $S_{two-photon}(x, y)$ is then proportional to the intensity $I_{field}(x, y, z)$ of the optical field [108]:

$$S_{two-photon}(x, y) \propto \int I_{field}^2(x, y, z) dy \quad (6.1)$$

The calculated fluorescence intensity distribution is shown as a greyscale image where white corresponds to maximum signal strength. In a next step the simulated evolution of the field within the micromotor is used to calculate the optical force F_z acting on each pillbox² $I(x, y, z)$ within the motor along the propagation axis in z . This force arises due to the refractive index difference between host medium n_h and motor n_c . From the force the optically induced torque τ was calculated with respect to the centre of the micromotor for each individual pillbox as:

$$\vec{\tau}(i) = \vec{r}_i \times \vec{F}_i \quad (6.2)$$

and for the whole motor:

$$\vec{\tau}_{motor} = \sum \vec{\tau}(i) \quad (6.3)$$

Where \vec{r}_i are the individual position vectors for the i^{th} pillbox with respect to the micromotor centre and \vec{F}_i being the acting force vectors. By summing

²Each pillbox is in xz normalised to the pixel length and width of the binary image. The height y of the pillbox is set by the normalisation of the grid in x , as both grids are equally spaced.

over all the pillboxes within the motor the overall acting torque on the motor was calculated. To account for different motor positions in the steady state model the torque was calculated for four 90-degree rotations of the micromotor and the average value was used in the following results for varying light field displacements in x . The negative displacement in x changes the sign of the torque acting on the motor leading to a change in rotation direction.

As is typical for optical micromanipulation studies in a liquid environment we have an over damped system. The optically induced torque matches the rotational Stokes drag resulting in a terminal angular velocity for the driven micromotor. To compare theoretically predicted torque with the measured rotation rate, I am following standard approaches [102, 107] to estimate the viscous drag of a rotating motor by approximating it as a disc. A viscous drag of $19 \times 10^{-18} Nm \pm 20\%$, at a constant rotation rate of $2Hz$ was estimated by [102] for the same micromotor design as used in the experiment. To put this in context, for the motor to spin at a constant rotation rate the optically induced torque has to equal the viscous drag of the motor. Due to the linear relation between rotation rate and viscous drag one can easily estimate the rotation rate from any given torque and vice versa. This caveat allowed to theoretically estimate the rotation rate of the micromotor within a limit of $\pm 20\%$ (which is due to the wobbling of the motor around the axle) for any calculated torque value. Regarding the approximated nature of this value, reasonable agreement between the experiment and model is achieved.

6.3 Experimental micromotor fabrication and experimental setup

The micromotor structures were fabricated by two-photon polymerisation³ [104] to be optically illuminated without hindrance by a bare, $125\mu m$ diameter single mode optical fibre perpendicular to the axis of the micromotor. The motor consists out of a 12-spoke motor, which has a diameter of $10\mu m$ and is $2\mu m$ tall, being held in place by a $10\mu m$ tall fixed axle, and a supporting structure, that holds the axle in place. The supporting structure is made such that it provides a free opening to the light that drives the gear. The whole structure is made on the surface of a microscope cover slide using

³The micromotors were fabricated by Dr. Lorand Kelemen from the BRC in Hungary under the envelope of the ATOM-3D collaboration.

a two-photon polymerisation method [102, 104]. Several micromotors were made at approximately $20\mu m$ distance from the edge of the microscope cover slide, which was placed upon a second cover slip. This is to form a $170\mu m$ step from which the motors could be illuminated by a single mode fibre, which has a radial cladding thickness of approximately $60\mu m$ (see figure 6.3). The fibre was mounted on a xyz-micro translation stage and could be aligned relative to the fixed micromotor to give a variable x offset from the central axis as well as a variable distance from the fibre end to the micromotor in z, which is limited by the coverslip edge on which the motor is levitated (the fibre can only be moved as close as the coverslip edge to the motor).

Two different laser sources were used to illuminate the fibre via a standard fibre coupling system. A continuous-wave (cw) ytterbium fibre laser (IPG Photonics) operating at $1070nm$ was used to investigate the rotation rate in dependence of the fibre distance and power. A 50:50 fibre beamsplitter was incorporated in the fibre system to *in situ* measure the power emerging at the fibre end (with an error of better than 3%) while operating the motor (see figure 6.3 (a)).

In a second experiment a Titanium-Sapphire (Ti:Sa) femtosecond laser, at a central wavelength of $\lambda = 800nm$ with $95fs$ output pulses, was used to visualise the light field distribution during operation of the motor via two-photon fluorescence excitation of the sample medium, here the same procedure for the sample preparation was used as described in the visualisation chapter. The imaging system consisted out of a $60\times$ microscope and a CCD camera, which was connected to a computer with a frame grabber card to capture the images. From these the geometry of the experiment (offset and distance of the fibre to the micromotor in x and z respectively with an absolute error of better than $\pm 0.5\mu m$) was determined using a LabView program.

This is the first direct visualisation of the light-micromotor interaction by utilising two-photon excitation within the sample medium. With this technique it is possible to visualise *in situ* the intensity profile of the beam at various stages in its propagation after interaction with the motor, driven by the beam. When the mode-locked emission from the Ti:Sa laser described above passes through the host medium, which contains a fluorescein dye and DI water mixture, a streak of two-photon absorption induced fluorescence corresponding to the laser beam intensity is observed. Upon interaction with the micromotor rotors the beam is diffracted and can be visualised in real time within the host medium. The fluorescein dye diluted in the host medium has a broad absorption band centred on $480nm$ with an emission band en-

tered on $530nm$ which can be easily registered with a CCD camera and an appropriate filter that blocks out the excitation wavelength at $800nm$. In the following section the experimental and theoretical results are shown.

6.4 Experimental and theoretical comparison

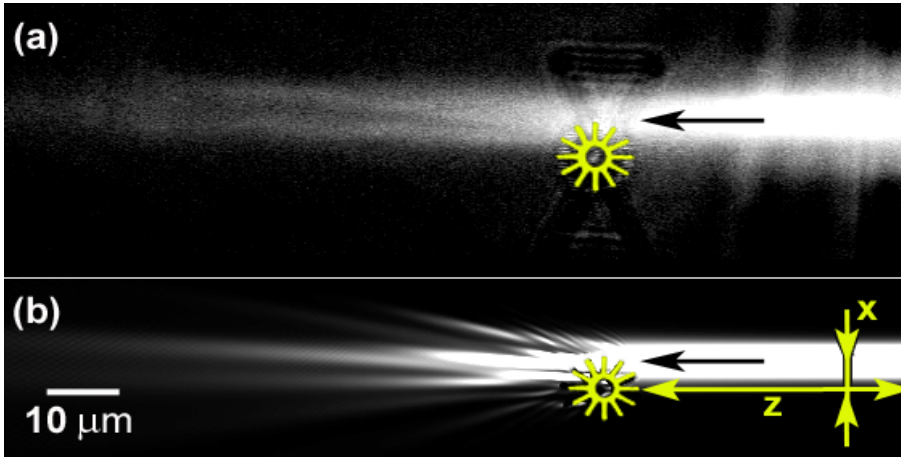


Figure 6.5: (a) Greyscale image of the experimentally observed two-photon fluorescence signal of the diffraction pattern of a spinning micromotor at approximately $50mW$ driving laser power. The laser beam driving the motor (overlaid image) is propagating from right hand side of the image and indicated by the overlaid arrows. Due to the limited response of dye and the doubled layer microscope slides only the two main diffraction streaks could be resolved. The image shows that diffraction occurs mainly in the forward direction. (b) Theoretical simulation with the motor being overlaid at the same orientation as in the experiment. Similarly to the experimental image two main diffraction streaks in the z direction can be observed. In both images, white corresponds to maximum signal intensity.

First I want to present the observed diffraction pattern of the beam upon interaction with the micromotor. In figure 6.5 (a) and (b) the experimental and theoretical predictions from equation 6.1 are shown respectively with x and z being the offset and the motor-fibre distance, respectively (axis labelling is concurrent with figure 6.5 (b)). In this particular arrangement the z distance is $45\mu m$ and the x offset is $4.8\mu m$.

Both in the experimentally and theoretically obtained images two main diffraction streaks can be observed, separated by an area of low diffracted light intensity. This shadowing effect is comparable to diffractive effects of an off-centred sphere in a beam, see figure 4.3, due to the circular outline of the motor. Finer diffraction effects of the rotors indicated in the simulations could not be resolved in the experiment due to the threshold-limited response

of the dye and the decreased image quality due to aberrations through the dual layer coverslip. However it can be readily observed that the main direction of scattering is along the light propagation axis. It supports that the approximation of calculating of the force F_z in propagation direction is an applicable approximation. And therefore our paraxial approach to simulate the light-motor system validated.

Next I investigated the rotation rate of the micromotor when driven by cw laser light at $1070nm$. Experimentally the rotation rate ($f_{rotation}[Hz]$) is averaged over 12 full rotations of the motor. The associated standard deviation in the rotation speed was estimated to 20% and is indicated in the vertical errorbars in figure 6.6. Two sets of experiments were conducted to determine the rotation rate with a fixed offset of $5.5\mu m$ along the x-axis. The first experiment shown in figure 6.6 a) was carried out at a distance $z=30\mu m$ to the fibre. The rotation rate of the motor was investigated as a function of the optical power emerging from the fibre.

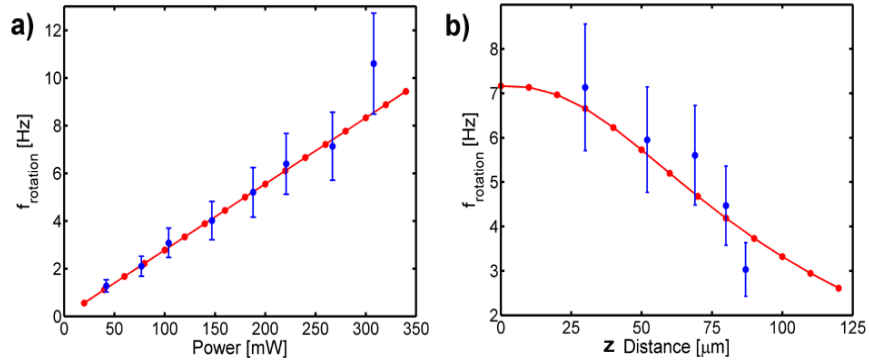


Figure 6.6: Comparison of experimental and theoretical rotation rates. Blue dots represent the average experiment values over 12 rotations; the error bars indicate the standard deviation of the measurements. Red line indicates the theoretical prediction. The offset x was $5.5\mu m$ in both cases. a) Motor rotation rate dependence on the optical power; b) Motor rotation rate dependence on the fibre distance to the motor with a constant power of $270mW$.

As expected, the rotation rate increases linearly with the power (see figure 6.6 a)). In figure 6.6 b) the power was left constant at $270mW$ and the rotation rate was investigated as a function of the distance between the fibre and the micromotor. A decrease in rotation rate is noticeable with increasing fibre distance. This is expected as the Rayleigh range of the output beam from the fibre is at approximately $30\mu m$ so the light intensity decreases more strongly along z beyond this distance. Due to the finite height of the motor the lower

light intensity interacts with the rotors with increasing separation causing the rotation rate to decay off. Again good agreement between experiment (blue dots) and theory (red line) is observed.

6.5 Optimisation of system and motor design

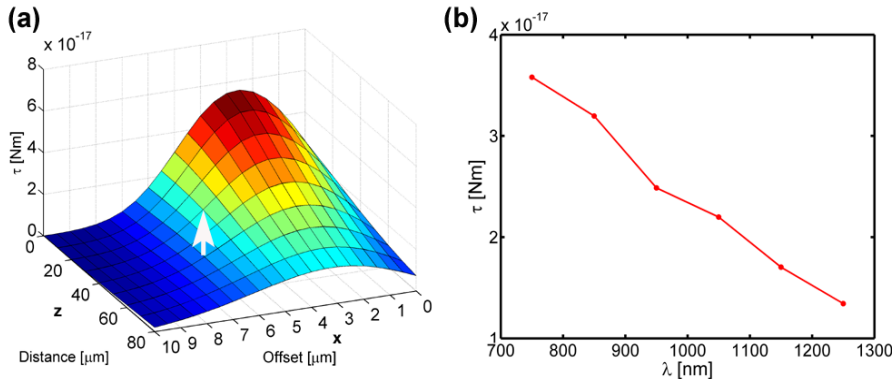


Figure 6.7: Torque in dependence of fibre or waveguide position. The white arrow marks the fibre position at which the results shown in figure 3(a) were taken. (b) Evaluation of torque acting on the motor in dependence of operating wavelength with an offset $x = 5.5\mu\text{m}$ and distance $z = 30\mu\text{m}$. For both simulations the optical power was fixed at 100mW .

The benefit of the model is that existing micromotor systems can be simply evaluated, their performance improved and new systems can be designed by systematically testing several key geometric and photonic parameters. In this system for example the optimum fibre offset position and operating wavelength can be determined. Such an analysis was performed and the data may be seen in figure 6.7.

The optimum position of the waveguide to apply the maximum torque on the motor would be at $x = 3\mu\text{m}$ offset and at $z < 10\mu\text{m}$ distance. This was not accessible in our experiment due to the coverslip edge on which the cogs were fabricated and a limited resolution of the positioning stage. The precise initial determination of these parameters is very important when the waveguide is integrated with the micromotor itself [102] and no successive realignment can be done. The performance of the system is enhanced with decreasing wavelength (shown in figure 6.7 (b)) over a popular range of IR wavelengths. Most importantly I am well placed here to evaluate different motor designs, as shown in figure 6.8. The symmetric nature of the dependence shows that

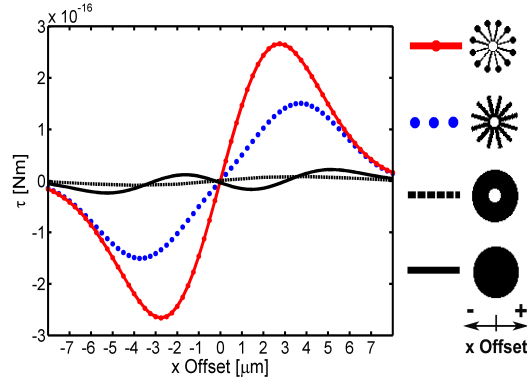


Figure 6.8: Torque in dependence of a varying offset in x evaluated for four different motor designs with constant diameter $10\mu m$ and height of $2\mu m$. Optical field parameters are kept constant to give comparative results. Four different designs are shown (from top to bottom) a snowflake, regular motor design, a cylinder with hole and a full cylinder to evaluate the error. Torques shown are for an optical power of $100mW$ and distance $z=10\mu m$.

the absolute value of the torque is the same on either side of the axis as long as the laser beam is at the same distance from the centre. The performance of the snowflake shaped motor shows relatively the highest efficiency with constant light field parameters for all simulations. The geometrical layout of the motors is constant in height ($2\mu m$) and diameter ($10\mu m$). The middle hole to accommodate the axle is $2\mu m$ in diameter, the individual fan thickness being $0.6\mu m$ and $1\mu m$ for the snowflake and regular motor respectively. To obtain additional torque, cylinders are added at the end of each rotor blade for the snowflake design with a diameter of $1.6\mu m$.

To investigate the error of the modelled motors I simulated the torque on a cylinder with the same height as the investigated motors with and without middle hole, which should have zero torque [109, 110, 111] when perfectly rotational symmetric. From our simulations we find an applied torque (see figure 6.8), which gives a maximum absolute error of $\pm 15\%$. This error is due to the limited resolution of the modelling via the binary image of the cylinder and the motor. Considering inaccuracies in the fabrication process of the motor these errors can still give a relative indication of the torque acting on a motor layout. Here more refined modelling like [112] needs to be applied. In contrast we find adding a hole to a cylinder should give an applied torque although perfectly symmetric.

6.6 Conclusion

This international project was conducted in collaboration with the Dr. Lorand Kelemen from the Biological Research Centre in Hungary who under the envelope of the ATOM-3D collaboration fabricated the micromotors investigated in this chapter. Importantly this research project allowed me to combine and put to work several key skills I have adapted throughout the previous chapters in optical binding to evaluate an engineering problem in the realm of optical micro motors.

I have demonstrated that two-photon excitation may be used to visualise the diffraction pattern of light around an arbitrarily shaped object, in our case a rotating micromotor. Although no backscattering was evident, it should be noted that a more in depth analysis of the cut off response of the dye should be undertaken to quantify the error of this analysis method.

The theoretical model developed for optical binding has been extended, to allow predicting the diffracted light intensity by utilising a modelling technique where a binary image is used to define different refractive index areas. Furthermore building on the optical field distribution I utilised the model to approximately predict the rotation rate of a micromotor. Here the same force calculation used in optical binding was ported to the problem of a rotating micro motor and this compared well to observed experimental rotation rates. Furthermore this additional gives confidence in the numerical model used for optical binding.

Building on the agreement between experiment and theory I showed that the model could be used to enhance the efficiency of the system by evaluating the optical driving geometry as well as light field parameters. Also I explore the efficiency of the motor, for which I have shown data for two designs and also evaluated the error. The developed model, which utilises a simple binary image of the rotor, made this evaluation possible, here one can envision an adaptive algorithm which self consistently optimises for the most efficient design.

In general the model provides a useful and versatile tool to optimise such micromachines before the fabrication process. The work presented here could be readily used to model even a fully integrated micromotor system where the laser diodes are integrated onto a lab on a chip device [7], so no external driving light source is needed.

Although I have shown how to enhance the rotation rate of the micromotor, there is still plenty of room to achieve higher efficiencies. To even further

enhance the rotation rate of the micromotor one can envision a multipass system where micro mirrors force the diffracted beam back onto the rotors again. Another method of realising such a system would be a second fibre counter-propagating to the first one. Here the offset in x from the central axis has to be for both fibres of different sign, so the induced torques act in the same direction.

Due to the strong divergence of the beam exiting the fibre a great fraction of the emitted light intensity is not even incident on the rotors of the micromotor. Here applying a lensed or a fibre with an axicon tip could be a possibility to deliver higher light intensities onto the rotors and further enhance the overall system performance. Furthermore this would change the gradient of the incident light and could alter significantly the force acting on the rotors.

Chapter 7

Conclusion

In this thesis I presented a detailed analysis of optical binding of two microspheres in one-dimension. The presented work relies on the diffractive refocusing of the trapping light field to create a self-mediated trapping geometry where the coupled light-matter interaction creates the trapping positions. The originality of the work is in the coupled nature of the system, which leads to the investigation of interesting nonlinear phenomena.

The thesis began with the introduction of the experimental setup a counter-propagating dual-beam fibre trap. Furthermore a particle tracking software, specifically tailored for optical binding was developed, one key feature of the program is the accurate tracking of the fibre separation of the CP fibre trap. Via initial experiments I elucidated the importance of the refractive index difference in the formation of an optically bound array. Importantly the chapter laid the basis for the theoretical model as physical key parameters of the light field and the bound matter were determined and used as input parameters for the model.

In the second chapter I focused on the simplest case of optical binding with two spheres. The centre separation between the two optically bound spheres was investigated in dependence on the sphere size, refractive index difference and the fibre separation. I presented that the coupled nature of the light sphere system allows to observe the nonlinear phenomena of bistability and hysteresis. Furthermore the theoretical model described in the appendix was used to numerically predict the sphere separation.

Optical binding can be qualitatively explained by the diffractive refocusing of the incident light field by one sphere onto its nearest neighbour. The third chapter focused on this inherent physical principle of the creation of optically

bound matter in the Lorentz-Mie regime. By developing a femtosecond fibre optical trap I was able to visualise the light field distribution via two-photon excitation in the host medium, thus making it possible to observe the light field distribution past one sphere as well as in an optically bound array. Here the number of spheres in a bound state was investigated in dependence of the refractive index difference and the experimentally observed intensity distributions compared to theoretical predictions. Two-photon induced imaging is widely used in many scientific disciplines to visualise complex fluid flow or soliton propagation for example, here I anticipate the work at hand to impact in the realm of redistributed light field trapping, where the light in multidimensional colloidal crystal can be mapped out.

Although diffractive refocusing can give an intuitive picture of the underlying principle that creates optically bound matter as discussed in chapters two and three it cannot paint a complete picture of the exact physics. It already fails to sufficiently explain the bistable behaviour of the two bound states for a varying refractive index difference. Here a more careful and detailed investigation, taking also the field gradient into account, needs to be realised. The fifth chapter continues with the coupling mechanism between the spheres via the light field. The correlated behaviour of the particles in the bistable regime was investigated and showed correlated and random correlated movement of the spheres. Furthermore the optical restoring forces acting in such a system were determined and compared to theoretical predictions. At this point of the work the paraxial approximation fails to predict the interference effects due to backreflections from the spheres surfaces. Although the experiment was tailored to inhibit those effects and keep to the paraxial approximation used for the theoretical predictions, they could never fully be eradicated.

In the final chapter I successfully ported my acquired knowledge in optical binding to an engineering problem in microfluidics. I investigated the diffraction pattern from a rotating micromotor showing that diffraction predominantly occurs in the forward direction. Although the limits for the paraxial approximation are surpassed for the relative high refractive index mismatch between motor and host medium, it was possible to approximately predict the micromotor rotation rate with the theoretical model used throughout my thesis. The reasonable agreement between experimental and theoretical investigations set the basis for theoretical optimisation studies of the driving light geometry and motor layout.

7.1 Outlook

Optical binding even in the simplest case of two spheres offers a wealth of opportunities, here the extension to smaller spheres into the Rayleigh regime can be explored. However certain limitations of the incident light field need to be overcome, as feasibility studies with Rayleigh spheres showed that the gradient perpendicular to the propagation direction does not provide sufficient confinement of the spheres.

An interesting prospective would be offered by photonic crystal fibres where the modefield diameter can be engineered to investigate array formation for different w_0 , here I would expect that the binding regime could be extended to bigger spheres. More importantly this could provide a better understanding of the influence of the initial field gradient in the creation of the array (especially in the bistable regime). A rapidly advancing fibre technology field is offering numerous possibilities to study optical binding for more exotic beam profiles, such as square beam profiles or via oval mode profile fibre with a sheet of light.

The extension of longitudinal binding to possibly two dimensions lies at hand, here one can explore the possibility of adding two additional CP fields into the trap area, so all fields are at 90° angles to each other. Such a geometry could even be realised in an integrated trap setup where four stripe emitter laser diodes are facing each other.

One can envision utilising the bistability of the optically bound array as a switching device in the field of photonic crystals, here however one major drawback is the subtle refractive index difference between host medium and sphere. Trapping of particles in air could provide here a interesting prospect to port optical binding to the arena of light guiding and switching within the field of photonic crystals.

Biophotonics has experienced a lot of excitement and drawn lots of interest in the optical trapping community. Whether optical binding will have an impact in this field by offering the possibility to store multiple cells in a line for collective handling is debatable. However the investigation presented showed that scattering from cells and the resulting array formation is very subtle and dependent on the parameters of the individual cell. The spread in inherent markers of such cells (refractive index and size) is wide spread so only qualitative conclusions on their behaviour in a light field can be made. Importantly this sensitivity indicates that using these markers for cell sorting might not be feasible.

The potential of optical binding in two counter-propagating fields still offers a wealth of exciting applications, as even the basic physical principle is presently still not fully understood.

7.2 List of Publications

The work at hand has resulted in the following publications:

Journal publications

- **Construction and calibration of an optical trap on a fluorescence optical microscope**, W.M. Lee, P. Reece, R.F. Marchington, N.K. Metzger, K. Dholakia, *Nature Protocols* (*accepted 2007*).
- **Observation and simulation of an optically driven micromotor**, N.K. Metzger, L. Kelemen, P. Ormos, A.A. Lagatsky and K Dholakia, (*JOPA accepted 2007, under revision*).
- **Erratum: Measurement of the Restoring Forces Acting on Two Optically Bound Particles from Normal Mode Correlations**, *Physical Review Letters* **98**, 068102 (2007), N.K. Metzger, R.F. Marchington, M. Mazilu, R.L. Smith, K. Dholakia, E.M. Wright, *Physical Review Letters*, 98, 219901(E), (25.May.2007).
- **Measurement of the restoring forces acting on two optically bound particles from normal mode correlations**, N.K. Metzger, R.F. Marchington, M. Mazilu, R.L. Smith, K. Dholakia, E.M. Wright, *Physical Review Letters*, 98, 068102, (9.February.2007). This publication was selected for the February 15, 2007 issue of Virtual Journal of Biological Physics Research.
- **Theory and simulation of the bistable behavior of optically bound particles in the Mie size regime**, N.K. Metzger, E.M. Wright and K. Dholakia, *New Journal of Physics*, 8, 139, (18.August.2006).
- **Visualization of optical binding of microparticles using a femtosecond fiber optical trap**, N.K. Metzger, E.M. Wright, W. Sibbett and K. Dholakia, *Optics Express*, 14, 3677-3687, (17.April.2006).

- **Observation of bistability and hysteresis in optical binding of two dielectric spheres**, N.K. Metzger, K. Dholakia and E.M. Wright, *Physical Review Letters*, 96, 068102, (16.February.2006). This article was featured in the Journal club in Nature Research Highlights.

Conference Papers

- **Optical binding (Presentation)**. N.K. Metzger, P.J. Reece, E.M. Wright, and K. Dholakia, Progress in electromagnetics research symposium 2007 (PIERS 2007), Beijing (CN), 26-30 March (2007).
- **Observation and simulation of the optical diffraction pattern generated by a rotating micro gear (Poster)**, L. Kelemen, P. Ormos, N.K. Metzger and K. Dholakia, SPIE Proceedings, Optical Trapping and Optical Micromanipulation III, San Diego, (OTOM'06), 6326-91 (2006).
- **Visualization of optical binding (Poster)**, N.K. Metzger, E.M. Wright, W. Sibbett and K. Dholakia, SPIE Proceedings, Optical Trapping and Optical Micromanipulation III, San Diego, (OTOM'06), 6326-101 (2006).
- **Optical binding of Chinese hamster ovary cells**, N.K. Metzger, P. Jess, L. Paterson, E.M. Wright and K. Dholakia, SPIE Annual Meeting, Proceedings of SPIE Vol. 5930 , 136-146, Optical Trapping and Micromanipulation II Conference, San Diego, 31 July-4 August (2005).

Appendix A

Theoretical model

A.1 Introduction

The force exerted on a dielectric sphere or object from an optical field can be calculated by either evaluating the Maxwell stress tensor, see for example [113, 114, 115, 116], or the Lorentz force [117, 118]. A comparison of the two approaches can be found in [119].

Classically two different approaches of approximation are used when calculating light forces in the realm of optical tweezers, dependent on the size of the particle relative to the wavelength of the field, one applies the Rayleigh or the ray optics approximation. The ray optics theory [120, 121, 33, 34] calculates the forces arising due to momentum transfer when a ray is reflected or refracted by the spheres using Snell's law and is valid in a regime where $\lambda \ll$ sphere radius.

In the Rayleigh approximation [122, 123, 124] (where $\lambda \gg$ sphere radius) a dielectric sphere is treated as a dipole in an electromagnetic field and the forces are calculated with reference to gradient¹ and scattering² forces. Where the particle interacts with the electromagnetic field only as an electric dipole (dipole approximation within the the Rayleigh theory). Here interesting resonance effects in dipole chains have been observed [125].

Here the imposed approximations limit the applications to either regime, however gave in previous work sufficient accurate results. More thor-

¹The dipole experiences a force proportional to the gradient of the inhomogeneous intensity.

²Dipoles that scatter absorbed light will experience a force in the direction of that light.

ough and exact approaches on modelling the electromagnetic field distribution in and around a dielectric sphere utilise for example the finite-difference time-domain technique [118] or the coupled dipole method (CDM) [126, 116, 127, 91] also known as discrete dipole approximation where the sphere is divided into individual dipoles which are smaller than the wavelength of the incident field, hence Rayleigh scattering is dominant. This method is very flexible and can be adapted to different scattering geometries, however it is computationally limited by the size of the scatterer.

Also several methods utilise the generalised Lorentz-Mie or Lorentz-Mie-Debye theory which describes the interaction of an arbitrary shaped beam with a homogeneous sphere³, for example [128, 129] or [130] where effects of the aberrations were taken into the field calculation, or the T-matrix approach which is as the CDM not limited to spherical objects [131, 132, 133] and is essentially an extension to the Lorentz-Mie theory. Another example is the finite element method (FEM) [134] to model the field distribution.

The above examples are usually used to model the field distribution in and around objects in a single beam optical tweezers with a strong field gradient and are computation intensive.

To-date only a few models have been developed to simulate optical binding in counter-propagating fields, such as [11] where the spheres are treated as scatterers and the array acts like a grating. The spheres position are defined by the maximum intensity of both scattered fields and gave good agreement with their experimental findings, when the sphere size is smaller than the field wavelength. Another approach by [91] uses the coupled dipole method combined with the Maxwell stress tensor and gave good agreement with the experimental findings presented in this work.

Importantly for a counter-propagating trapping geometry, where weak diverging beams are harnessed a paraxial approach can be implemented [18], which is commonly used in photonics to simulate field propagation within waveguides for example. This approach formed the basis for the theoretical simulations presented in this work and will be discussed, with a new force calculation based on the work of [118], in this chapter.

The main theoretical challenge in modelling optically binding lies in the accurate prediction of the trap sites of the individual spheres, which is in contrast to most common optical tweezers, with predefined trap sites e.g. [24, 47] and standing wave traps [30] where the spheres are spaced by $\lambda/2$.

³Often simply referred to as Mie theory.

For an optically bound array (shown in figure 3.1) the interplay between light and matter creates trapping positions self-consistently where the net force on each sphere is zero.

Here already several prerequisites to a theoretical approach can be highlighted:

It is clear that the redistributed field before and past the spheres needs to be accurately modelled. Due to the elongated geometry of the system in one dimension (the propagation axis) a paraxial beam propagation model lends itself to be a good approach to calculate the field distribution in and around the spheres [18]. Furthermore as the system can be extended to multiple spheres the calculation of the fields needs to be reasonably fast and makes a often time consuming rigorous field calculation less favourable.

From the fields the acting forces need to be calculated, in previous work [18] an expression was employed for the force on each sphere as the spatial gradient of the interaction energy between the sphere and field. Although this formalism gave qualitative agreement with the experiments a new approach based on the Lorentz force [117, 118] will be used in this work as it was found to increase the accuracy of the simulations.

The program consists of three main parts: the free space propagation, the propagation in an inhomogeneous refractive index distribution (sphere) and the force calculation. In this section I will describe the numerical model developed by Prof. Ewan M. Wright and its implementation in Matlab [18].

A.2 Beam propagation

Two counter-propagating (CP) monochromatic laser beams, separated by a distance D_f and propagating along z in a host medium of refractive index n_h are incident in the paraxial regime on spheres of radius r_{sphere} and refractive index n_s .

Each electric field evolves according to the wave equation in a medium [35] to:

$$\nabla^2 \vec{E} - \frac{1}{c^2} * \frac{\partial^2 \vec{E}}{\partial t^2} = \underbrace{\mu_0 * \frac{\partial^2 \vec{P}}{\partial t^2}}_{=0(vacuum)} \quad (A.1)$$

$\frac{1}{c^2} = \epsilon_0 \mu_0$
 $\mu_0 =$ magnetic permeability
 $\epsilon_0 =$ electric permittivity
 $\vec{P} = \epsilon_0 * \chi * \vec{E} =$ electric dipole moment density (medium dependent)
 $\chi = n^2 - 1$

The medium with the spheres represents an inhomogeneous refractive index distribution that the field encounters lateral to the propagation direction which makes it necessary, to specify the polarisation \vec{P} or dipole moment density⁴ in the medium. A nonzero dipole moment density arises from the electron oscillator model. When a field is incident on the atoms (N = number of atoms) of an medium each electron is getting displaced, the polarisation density is N times the individual dipolmoment of each atom. The combined oscillator characteristic of an material is described by the electric susceptibility $\chi(\omega)$ which is dependent on the frequency of the incident field. The response of an dielectric⁵ material follows to:

$$\vec{P} = \epsilon_0 \chi \vec{E} \quad (\text{A.2})$$

$$n^2(\omega) = 1 + \chi(\omega) \quad (\text{A.3})$$

\vec{E} = Incident field
 $\chi(\omega)$ = electric susceptibility

We consider that N transparent dielectric spheres of mass m , refractive index n_s and radius r_{sphere} are in a fixed configuration at time t specified by $\vec{r}_j(t), j = 1, 2, \dots, N$. The spheres are immersed in a host liquid with a refractive index n_h , to define the refractive index dependent on the position vector $\vec{r} = (x, y)$ we utilise the Heaviside step function to define the refractive index variation to:

$$\begin{aligned} n^2(\vec{r}) &= n_h^2 + (n_s^2 - n_h^2) \sum_{j=1}^N \theta(r_{sphere} - |\vec{r} - \vec{r}_j(t)|) \\ &= n_h^2 + \Delta n^2(\vec{r}) \\ &= n_h^2 + (n^2(\vec{r}) - n_h^2) \end{aligned} \quad (\text{A.4})$$

$\theta(r_{sphere} - |\vec{r} - \vec{r}_j(t)|)$ =
Heaviside step function
Inside sphere = 1
Outside sphere = 0

The Heaviside step function is unity within the sphere, centred on $\vec{r} = \vec{r}_j(t)$, and zero outside.

Considering a monochromatic field the position dependent dipole density \vec{P} becomes:

$$\vec{P}(\vec{r}) = \epsilon_0 \underbrace{(n_h^2 + \Delta n^2(\vec{r}) - 1)}_{n^2(\vec{r})} \vec{E} \quad (\text{A.5})$$

⁴Electric dipole moment per unit volume of medium.

⁵Not conducting no free electrons (= no free charges).

which gives (put into A.1) and some modifications:

$$\begin{aligned} \nabla^2 \vec{E} - \frac{1}{c^2} * \frac{\partial^2 \vec{E}}{\partial t^2} &= \mu_0 * \frac{\partial^2}{\partial t^2} \left[\epsilon_0 \left((n_h^2 + \Delta n^2(\vec{r})) - 1 \right) \right] \\ &\quad \begin{array}{l} \Delta n^2(\vec{r}) = \text{perturbation} \\ \text{space dependent} \\ \frac{1}{c^2} = \epsilon_0 \mu_0 \end{array} \\ 0 &= \nabla^2 \vec{E} - \frac{\overbrace{(n_h^2 + \Delta n^2(\vec{r}))}^{n^2(\vec{r})}}{c^2} * \frac{\partial^2 \vec{E}}{\partial t^2} \end{aligned} \quad (\text{A.6})$$

Which is the wave equation for a position dependent refractive index variation of Δn . For which we seek solutions for a single frequency field.

$$\vec{E}(\vec{r}, t) = \frac{1}{2} \left[\underbrace{\vec{E}(\vec{r}, \omega)}_{\text{space}} \underbrace{e^{-i\omega t}}_{\text{time}} + c.c. \right] \quad (\text{A.7})$$

in A.6

$$\begin{aligned} 0 &= \frac{1}{2} \left[e^{-i\omega t} \nabla^2 + c.c. \right] - \frac{1}{2} \frac{n^2(\vec{r})}{c^2} \vec{E}(\vec{r}, \omega) \frac{\partial^2}{\partial t^2} e^{-i\omega t} + c.c. \\ 0 &= \frac{1}{2} e^{-i\omega t} \left[\underbrace{\nabla^2 \vec{E}(\vec{r}, \omega) + \vec{E}(\vec{r}, \omega) \frac{\omega^2 n^2(\vec{r})}{c^2}}_{\text{must}=0} \right] + c.c. \\ 0 &= \nabla^2 \vec{E}(\vec{r}, \omega) + \frac{\omega^2 n^2(\vec{r})}{c^2} \vec{E}(\vec{r}, \omega) \end{aligned} \quad (\text{A.8})$$

Which is the Helmholtz equation in vector form to proceed we will utilise the simpler scalar form. The scalar approach keeps the polarisation vector (\hat{x}) at 90° fixed to the z-axis not allowing for coupling effects between the field components where \vec{E} decomposed in $(\hat{x} \cdot \vec{E}, \hat{y} \cdot \vec{E}, \hat{z} \cdot \vec{E})$. These coupling effects are small and the approximation is correct for small angle changes with Δn being small [49], as shown in figure A.1. Also for small apertures or spheres, where $r_{\text{aperture/sphere}} \ll \lambda$ (Rayleigh regime) or $w_0/\lambda \gg 1$, here coupling effects between the electric and magnetic field components become significant and the scalar theory fails [49].

More specifically, the focal length for a sphere in the small-angle approximation neglecting aberrations is $f = r_{\text{sphere}}/(2\Delta n)$ [68], and since the sphere only focuses rays that pass through it within the sphere radius away from the axis an effective numerical aperture acts. For the sphere

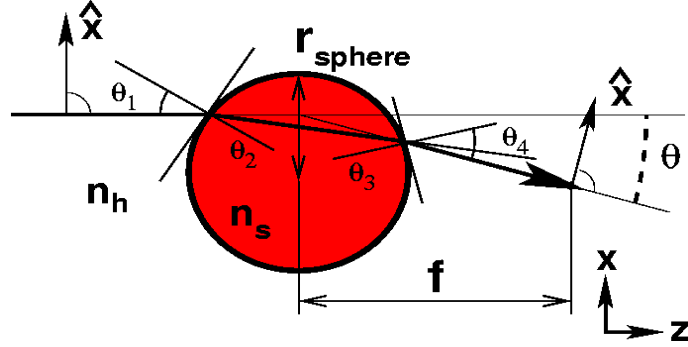


Figure A.1: Approximated ray optics picture of a sphere refracting an incident ray. With the polarisation vector \hat{x} being fixed to the propagation axis in z . From Snell's law we get $\frac{\sin\theta_1}{\sin\theta_2} = \frac{v_1}{v_2} = \frac{n_h}{n_s}$ for the ray entering the spheres and $\frac{\sin\theta_3}{\sin\theta_4} = \frac{n_s}{n_h}$ for the ray exiting the sphere. The backreflected ray is not shown, as they are neglected due the low refractive index difference (Back reflections $R = (\frac{n_h - n_s}{n_h + n_s})^2 \approx 0.1$). The ray is getting focused by the sphere leading to the small angle approximation. Where the maximum deflection angle $\theta_{max} = 1$ due to the sphere follows from $\sin(\theta_{max}) = r_{sphere}/f$.

$NA = \sin(\theta_{max}) = r_{sphere}/f = 2\Delta n$, with θ_{max} the maximum ray deflection angle due to the sphere, see figure A.1. Since $\Delta n < 0.1$ for the experiments and simulations presented here, the spheres act as low $NA < 0.2$ focusing elements that can be well treated using scalar paraxial theory. The maximum deflection angle $\theta_{max} = 1$ due to the sphere being small, so that initial paraxial rays will remain paraxial and the incident polarisation state of the field will be mainly unchanged. However the paraxial approximation well captures diffraction and interference (due to the preserved phase information) in contrast to a ray optics approach. Accordingly from this analysis we see that our approach improves with decreasing Δn as it is implied in the experiments, but it is expected to fail for higher refractive index differences. To proceed we approximate $\vec{E}(\vec{r}, \omega)$ to seek a monochromatic and scalar⁶ solution to the Helmholtz equation⁷ where the field is treated as being purely x-polarised perpendicular to the propagation axis in z :

$$\vec{E}(\vec{r}, \omega) = \hat{x} \mathcal{E}_{\pm} \underbrace{e^{\pm i(n_h \frac{\omega}{c})z}}_{\text{carrierwave}} \quad (\text{A.9}) \quad \begin{matrix} k = \frac{\omega n_h}{c} = \frac{2\pi}{\lambda} \\ \nu_{\text{phase}} = \frac{\omega n_h}{|k|} = n * c = \\ \frac{1}{\sqrt{\mu_0 \epsilon_0}} \end{matrix}$$

⁶Which signifies that the polarisation state is unaltered in contrast to a full vectorial treatment.

⁷Hence a monochromatic solution to the wave equation.

where \hat{x} is the unit polarisation vector of the field, \mathcal{E}_\pm the slowly varying electric field amplitude⁸ and $k = \pm n_h \omega / c = n_h k_0$ is the wavevector of the field in the host medium. Where \pm indicates the propagation direction of the field in z, for a counter-propagating beam geometry, where (+) is the left hand or forward propagating field and (-) signifies the right hand or backward propagating field. Following standard approaches [135] the field evolves accordingly by solving A.8 with A.9 and A.4

$$\begin{aligned}
0 &= \left(\underbrace{\frac{\partial^2}{\partial^2 x} + \frac{\partial^2}{\partial^2 y} + \frac{\partial^2}{\partial^2 z}}_{\nabla_T^2} \right) \hat{x} \mathcal{E}_\pm e^{\pm i(n_h \frac{\omega}{c})z} + \frac{\omega^2 n^2(\vec{r})}{c^2} \hat{x} \mathcal{E}_\pm e^{\pm i(n_h \frac{\omega}{c})z} \\
0 &= \hat{x} \mathcal{E}_\pm e^{\pm i(n_h \frac{\omega}{c})z} \left[\nabla_T^2 \mathcal{E} + \underbrace{\frac{\partial^2 \mathcal{E}_\pm}{\partial z^2}}_{drop} + 2i \left(n_h \frac{\omega}{c} \right) \frac{\partial \mathcal{E}_\pm}{\partial z} - \left(n_h \frac{\omega}{c} \right)^2 \mathcal{E}_\pm \right] \\
\dots &+ \hat{x} \mathcal{E}_\pm e^{\pm i(n_h \frac{\omega}{c})z} \left[\frac{\omega^2 n_h^2}{c^2} \mathcal{E}_\pm + \frac{\omega^2 n_h^2}{\omega^2 \Delta n^2(\vec{r})} \mathcal{E}_\pm \right] \\
\pm \frac{\partial \mathcal{E}_\pm}{\partial z} &= \underbrace{\frac{i}{2k} \nabla_T \mathcal{E}_\pm}_{diffraction-host} + \underbrace{ik_0 \frac{\Delta n^2(\vec{r})}{2n_h} \mathcal{E}_\pm}_{phaseshift-sphere} \tag{A.10}
\end{aligned}$$

$$\begin{aligned}
\nabla_T^2 &= \text{Transverse Laplacian} \\
n^2(\vec{r}) &= n_h^2 + \Delta n^2(\vec{r}) \\
k &= \frac{\omega n_h}{c} \\
k_0 &= \frac{\omega}{c}
\end{aligned}$$

In the derivation the position vector (\vec{r}) dependence of \mathcal{E}_\pm has been omitted. Where $\frac{\partial^2 \mathcal{E}_\pm}{\partial z^2}$ gets neglected due to the slow varying envelope approximation⁹ which follows from this assumption [136]. Thus the the exact wave equation A.8 is reduced and we obtain the paraxial wave equation with a $\vec{r} = (x, y, z)$ space dependent refractive index variation of Δn for two counter-propagating fields. The paraxial approximation is based on the notation that the propagation distance for an optical wave along the z-axis is much greater than the transverse spreading of the wave. With the cancellation of the second or-

⁸Which is the scalar wave amplitude describing the transverse beam profile (Gaussian shape).

⁹Paraxial approximation: The z dependence of the wave amplitude \mathcal{E}_\pm is due to diffraction effects and will be slow compared to one wavelength as in e^{-ikz} and the transverse variation is approximated much higher than in propagation direction z due to the finite width of the beam, with $\frac{w_0}{\lambda} \gg 1$.

der derivative term we obtain a first order differential equation (the paraxial wave equation) for which we seek Gaussian solutions in the next section.

A.3 Gaussian beam solution of paraxial wave equation

Following [35, 136] the lowest-order Gaussian beam characterised by its spot size w_0 and a planar wavefront $R_0 = \infty$ in the transverse plane (x,y) has a normalised field at a plane z of the form:

$$\mathcal{E}(x, y, z) = \sqrt{\frac{2}{\pi}} \frac{1}{\omega(z)} e^{-ikz + \tan^{-1}\left(\frac{z}{z_R}\right)} e^{\frac{ik(x^2+y^2)}{2R(z)}} e^{-\frac{(x^2+y^2)}{\omega^2(z)}} \quad z_R = \frac{\pi w_0^2}{\lambda} \quad (\text{A.11})$$

By defining the total power in an optical beam as $P = \iint |\mathcal{E}|^2 dA$ (where dA is cross section area integral) we obtain from the radial intensity distribution [136]:

$$I = \frac{1}{2} \epsilon_0 n_h c |\mathcal{E}(x, y, z)|^2 = \frac{2P}{\pi w_0^2} e^{-\frac{2(x^2+y^2)}{w_0^2}} \quad (x^2 + y^2) = r^2$$

$$\mathcal{E}(x, y, z) = \sqrt{\frac{4P}{\epsilon_0 \pi n_h c w_0^2}} e^{-\frac{2r^2}{w_0^2}} \quad (\text{A.12})$$

Where the intensity is averaged over one optical cycle.

A.4 Field propagation numerical model

Now we are well placed to numerically simulate the beam propagation in our light-matter system. Here two different beam propagation sections are to be distinguished, parts where the field experiences diffraction only due to free space propagation in the host medium (a distance z_0 from the beam waist w_0 to the first sphere with diameter d_s and a distance z_1 from the end of the first sphere to the second sphere) and parts where the field encounters the varying refractive index distribution due to the spheres (in the first sphere

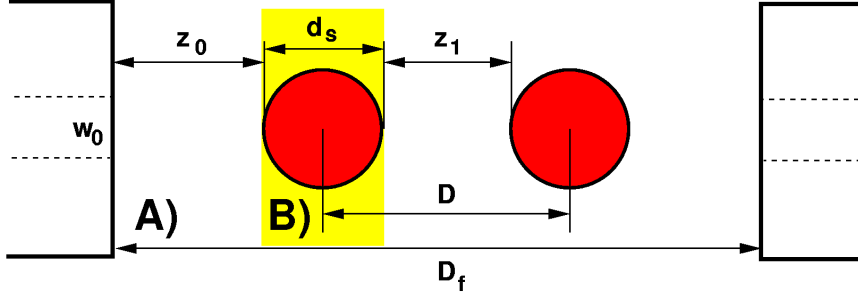


Figure A.2: Geometrical layout of the beam propagation algorithm: Distance z_0 from the beam waist w_0 to the first sphere with diameter d_s and distance z_1 from the end of the first sphere to the second sphere. The waists are separated by D_f assuming mirror symmetry around $D_f/2$ for the center of the array with D the centre separation. A) signifies the homogeneous and B) the inhomogeneous part in which the field propagates.

and the second sphere), see figure A.2.

The propagation of the field can therefore be split in A) homogeneous parts (refractive index is constant to n_h) and B) inhomogeneous parts (refractive index can be n_h or n_s dependent on the position of the field \vec{r}). Both beam propagation parts will be dealt with in the following section, for simplicity I will solely focus on the forward propagating field (+)¹⁰.

A.4.1 A) propagation in homogeneous medium n_h

To numerically propagate a paraxial field amplitude $\mathcal{E}_+(x, y)$ in the z -direction from one plane ($z = z_i = 0$ at w_0) to the next ($z = z_0$). Solutions have to be found to the wave equation, from A.10 where $\Delta n^2 = n_h^2 - n_h^2 = 0$ so the wave equation becomes for the forward propagating field:

$$\frac{\partial \mathcal{E}_+}{\partial z} = \underbrace{\frac{i}{2k} \nabla_T^2 \mathcal{E}_+}_{\text{diffraction}} + 0 \quad (\text{A.13})$$

with $\Delta n = 0$

An algorithm is used that decomposes the field into plane waves, where each component travels at a different angle in k -space¹¹ or wave vector space. Each component is propagated individually by adding a phase shift due to

¹⁰As will be shown later due to the symmetry of the system only one beam propagating past two spheres is calculated.

¹¹Engineering terminology: frequency space.

the beam diffraction and then transformed back to give the new spatial wave function. The algorithm consist out of the following steps [137, 118, 138] ¹²:

- The electric field is Fourier transformed and thereby decomposed into individual plane waves at the start plane $z = z_i = 0$.

$$\tilde{\mathcal{E}}(k_x, k_y, z = 0) = \frac{1}{(2\pi)^2} \int \int \mathcal{E}(x, y, z = 0) e^{i(k_x x + k_y y)} dk_x dk_y \quad (\text{A.14})$$

$\tilde{\mathcal{E}}(k_x, k_y, z) = \text{spectrum}$

$\tilde{\mathcal{E}}(k_x, k_y, z)$ is the transverse spectrum of the electric field and can be seen as the field amplitude of a plane wave with wave vectors in the transverse plane k_x and k_y .

- The component in the z-direction k_z for each of these plane waves can be simply calculated by:

$$k_z = \sqrt{k^2 - k_x^2 - k_y^2} \quad (\text{A.15}) \quad \begin{matrix} k = \frac{2\pi n_h}{\lambda} \\ k_z^2 + k_x^2 + k_y^2 = \frac{n^2 \omega^2}{c^2} = k^2 \end{matrix}$$

Here we do not apply the Fresnel approximation¹³ which assumes that the field does not change much in the transverse plane $|k_{x,y}| \ll k$ (or plane wave approximation) for enhanced accuracy of the model. Assuming a monochromatic field with wavenumber k in a medium of refractive index n_h .

- When the field is propagated a distance $\Delta z = z_0$ in the positive z-direction each of the plane wave components experiences a phase shift $\Delta\phi = k_z \Delta z$. The amplitudes of the individual components in the transverse plane $z = z_0 = \Delta z$ are related to the initial plane through:

$$\tilde{\mathcal{E}}(k_x, k_y, z = z_i + \Delta z) = \tilde{\mathcal{E}}(k_x, k_y, z = z_i) e^{(-i\sqrt{k^2 - k_x^2 - k_y^2} \Delta z)} \quad (\text{A.16})$$

$\Delta z = \text{propagated distance}$
 $\tilde{\mathcal{E}}(k_x, k_y, z) = \text{spectrum}$

¹²This algorithm was first proposed by [139].

¹³Or paraxial approximation which is a binomial expansion of the root coefficient.

- By taking the inverse Fourier transform the electric field distribution, after a propagated distance $\Delta z = z_0$, is obtained. This represents an exact solution to the wave equation.

$$\mathcal{E}(x, y, z = z_i + \Delta z) = \frac{1}{(2\pi)^2} \int \int \tilde{\mathcal{E}}(k_x, k_y, z = z_i) e^{-i(k_x x + k_y y)} e^{-i\sqrt{k^2 - k_x^2 - k_y^2} \Delta z} dx dy \quad (A.17)$$

The Fourier Transformation is carried out by using a discrete fast Fourier Transform algorithm (FFT) which is readily obtained in MATLAB¹⁴. Here A.17 simply reduces to:

$$\mathcal{E}(x, y, z = z_i + \Delta z) = iFFT \left[FFT [\mathcal{E}(x, y, z = z_i)] * \underbrace{e^{-i\sqrt{k^2 - k_x^2 - k_y^2} \Delta z}}_{\text{frequency transfer function}} \right] \quad (A.18)$$

However care has to be taken to choose the right sampling parameters, e.g. grid size and resolution. The grid size has to be big enough so the transformed electric field is not cropped by the boundaries¹⁵.

A.4.2 B) propagation in inhomogeneous medium

$$n(\vec{r}) = n_s + \Delta n$$

To propagate the field within the sphere the split-step Fourier method is used to account for phase shift and diffraction within the sphere for a inhomogeneous or varying refractive index distribution due to the sphere. By segmenting the sphere into individual cylindrical slabs j , see figure A.3.

The field distribution is calculated at the beginning (1) and at the end (2) of each slab (j) of radius r , see figure A.3. The algorithm for the split-step method follows from [137] to:

¹⁴©MathWorks.

¹⁵If the field is cropped, reflections of the field at the boundaries occurs.

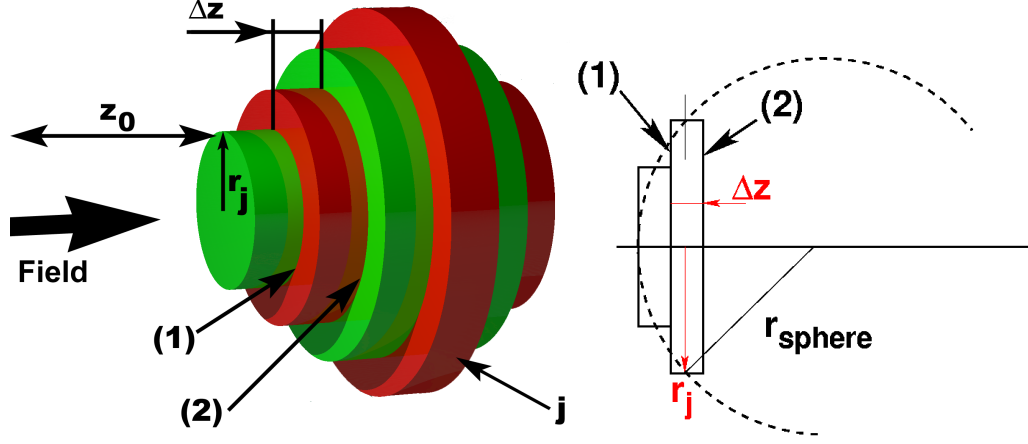


Figure A.3: Resolution of the sphere within the split-step beam propagation method. Left: 3D view of the sphere approximated by cylindrical slabs. The field is propagated a distance z_0 to the beginning of the first slab. Right: j indicates the number of each slab which has got an individual radius of r_j and a width of Δz the actual sphere radius intersects each slab j at $\Delta z/2$ to obtain a volume approximation of the sphere.

$$\begin{aligned}
 \mathcal{E}(x, y, z_{j+1}) &= (\hat{A} + \hat{B}) \mathcal{E}(x, y, z_j) \\
 \mathcal{E}(x, y, z + \Delta z) &= e^{(\hat{A} + \hat{B}) * \Delta z} \mathcal{E}(x, y, z_j) \\
 \mathcal{E}(x, y, z_j + \Delta z) &\approx e^{\hat{A} * \Delta z} e^{\hat{B} * \Delta z} \mathcal{E}(x, y, z_j)
 \end{aligned}
 \tag{A.19}$$

\hat{A} = diffraction operator
 \hat{B} = inhomogeneous operator

Where (from A.10) $\hat{A} = \frac{i}{2k} \nabla_T \mathcal{E}_+$ is the linear differential operator that accounts for beam diffraction and $\hat{B} = ik_0 \frac{\Delta n^2(\vec{r})}{2n_h} \mathcal{E}_+$ is the space dependent or inhomogeneous operator. Here the inhomogeneous operator adds an additional phase shift to the diffraction operator of $\Delta n(\vec{r})$ where the beam encounters the sphere. This additional phase change is applied at the beginning of each cylindrical slab (marked (1) in figure A.3) in MATLAB to:

$$\mathcal{E}(x, y, z) = \mathcal{E}(x, y, z) e^{\left(ik_0 \frac{n_s^2 - n_h^2}{2n_h} \theta_{r_j} \right) \Delta z} \tag{A.20}$$

$k_0 = \frac{2\pi}{\lambda}$
 $k = \frac{2\pi n_h}{\lambda}$

where θ_{r_j} is a Heaviside step function which is zero outside each slab j and unity within the slab of radius r_j ¹⁶. The field is then propagate with A.20 a

¹⁶Outside the sphere $\mathcal{E}(x, y, z) = \mathcal{E}(x, y, z)$ the field remains the same.

step length Δz to plane (2) see figure A.3.

Here two constraints apply to the step length Δz and the sampling grid in x,y for the scalar field, with step size Δx and Δy :

- The sphere should be accurately sampled so the first and the last slab is resolved within the sampling grid in x and y. The radius of the first slab is $r_1^2 = r_{sphere}^2 - (r_{sphere} - \Delta z/2)^2$ where the radius of the Sphere intersects with the slabs at $\Delta z/2$ (see figure A.3(right)). Using $r_{sphere} \gg \Delta z$ we obtain a minimum stepsize of:

$$\Delta z > \frac{1}{r_{sphere}} \Delta x^2.$$

- Given a grid spacing $\Delta x = (x_{max}/n_x)$ with x_{max} the grid size and n_x the number of points. We want the phase change to be small to capture the outline of the sphere with the optical field distribution. Hence the step size needs to be sufficiently small to resolve the refocusing effect of the sphere. From A.13 we obtain $k_T^2 \Delta z / 2k = k_{max}^2 \Delta z / 2k < 1$ with $k_{max} = (\pi/\Delta x)$ is the maximum transverse wavevector and $k = 2\pi n_h/\lambda$. The constraint for the stepsize Δz is:

$$\Delta z < \frac{4n_h \Delta x^2}{\pi \lambda}$$

Next I continue with the calculation of the forces that act on the spheres.

A.5 Force calculation

To proceed we need equations of motion for how the sphere centres move in reaction to the fields which requires calculation of the forces acting on the spheres. Assuming over-damped motion of the spheres with viscous damping coefficient γ , the equations of motion for the sphere centres can be written without the presence of Brownian noise as:

$$m\gamma \frac{d\vec{r}_j}{dt} = \vec{F}_j \quad (A.21) \quad \begin{array}{l} j = 1, 2, \dots, N \\ j = \text{sphere number} \end{array}$$

Here the full three-dimensional simulations with modeling of the electromagnetic propagation in the presence of the spheres is a formidable challenge. To simplify the calculations involved we take advantage of the symmetry of the system, see figure A.4 to reduce the calculations involved.

First, for the cylindrically symmetric Gaussian input beams used here we

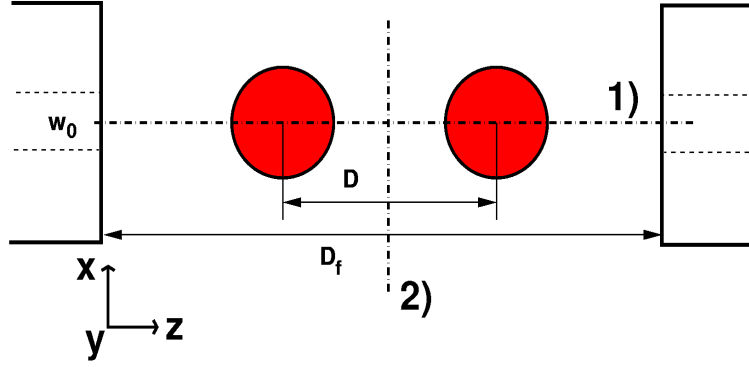


Figure A.4: Assuming the spheres being well confined in the center of the counter-propagating fields (in the xy -plane) and symmetric around the center between the two fibres at $D_f/2$ and $D/2$. Two symmetry axis can then be distinguished (marked 1) and 2)): 1) rotational symmetry around the z -axis, the beam center. 2) mirror symmetry in the y -plane located at $D_f/2$.

assume that the applied laser fields supply strong enough transverse confinement in the xy -plane that the sphere motion remains directed along the z -axis. This means that the positions of the sphere centres are located along the z -axis $\vec{r}_j(t) = \hat{z}z_j(t)$, and that we may also concentrate on the component of the forces along the z -axis $\vec{F}_j = \hat{z}F_j$ and neglect forces confining the spheres in the xy -plane. To calculate the forces acting on the spheres we follow the approach of Zakharian *et al.* [118] where the force on the j^{th} sphere from two Gaussian fields A.12 within the slow varying envelope approximation can be expressed (from [61] by Prof. E.M. Wright) as:

$$\begin{aligned}
 F_j(t) &= \frac{\epsilon_0(n_s^2 - n_h^2)}{4} \int_{V_j} d^3\vec{r}' \left(\frac{\delta|\mathcal{E}|_+^2}{\delta z'} + \frac{\delta|\mathcal{E}|_-^2}{\delta z'} \right) \\
 &= \frac{\epsilon_0(n_s^2 - n_h^2)}{4k} \int_{V_j} d^3\vec{r}' \text{Im} \left(-\mathcal{E}_+^* \nabla_T^2 \mathcal{E}_+ + \mathcal{E}_-^* \nabla_T^2 \mathcal{E}_- \right)
 \end{aligned}
 \tag{A.22}$$

which is the volume integral over the sphere, where the force is proportional to the gradient of the beam intensity ($F \propto \nabla I$). Here we assume that the forward (+) and backward (-) propagating fields are mutually incoherent so no standing wave trap [30] is formed. This allows us to unfold the mirror symmetry in A.4 so numerically we propagate solely the forward field through sphere 1 and then through sphere 2. To proceed I would like to give an

example of one single beam interacting with one sphere and then move on to a two sphere array.

A.5.1 One sphere one beam

Numerically the forces arising on one sphere (F_{sphere}) is obtained by summing up the forces acting on each individual cylindrical slab of the sphere j (as shown in figure A.3) to:

$$F_{sphere} = \sum_j \frac{\epsilon_0(n_s^2 - n_h^2)}{4k} \int_{V_{slab}} d^3\vec{r} Im \left(-\mathcal{E}_+^* \nabla_T^2 \mathcal{E}_+ \right) \quad j = \text{sphere slabs} \quad (\text{A.23})$$

In the following graph A.5 the evolution of the force of one beam propagating through one sphere consistent out of j slabs is show. To elucidate the effects of the xy-sampling grid resolution two graphs are plotted for as grid size of 256 and 512 points (nx). Where nx is the number of sampling points in the propagation plane.

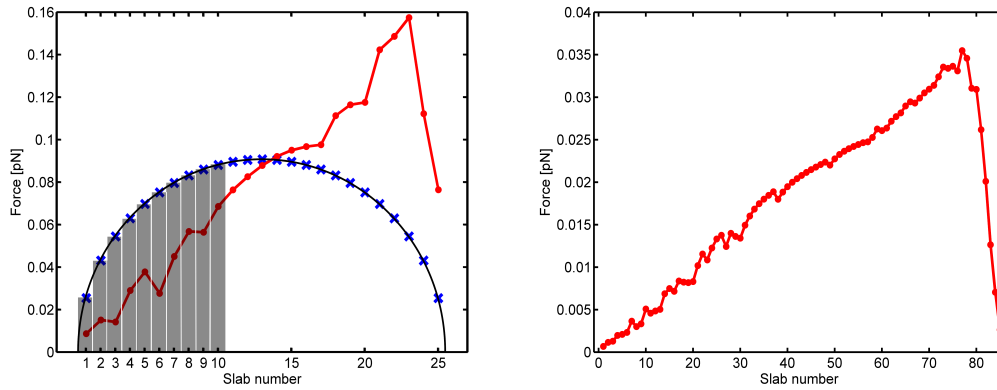


Figure A.5: Evolution of the force within a $3\mu\text{m}$ sphere $40\mu\text{m}$ away from the beam waist, for different slab numbers. Left: red shows the evolution of the Force per slab with the sphere for 256×256 grid points and a Δz of 120nm where 25 slabs reassemble the whole sphere. The total force acting in the propagation direction of the field is 1.47pN . Additionally the first few slabs are overlaid to aid the eye. Right: for 512×512 grid points the sphere is reassembled by 85 slabs and a total force of 1.54pN is acting. For both grids the numerical constraints apply.

Figure A.5 shows clearly how the grid size and hence the resolution of the sphere affects the force profile where a coarser resolution makes the force graph jiggle. Although the difference in total force is negligible I will in

more detail investigate the influence of the resolution on the simulated array formation later in the experiment section.

A.5.2 Error evaluation

For the one sphere case described in the previous section, I want to evaluate the error associated with the paraxial approximation and see where this approximation breaks down. From the slow-varying envelop approximation we specialise our numerical model to small refractive index differences and fields with low NA. The Helmholtz equation for a single field from A.10 can be rewritten with the second order derivative of the field to give the ratio of the error (Dr. M. Mazilu):

$$\begin{aligned} \frac{\partial \mathcal{E}_{\pm}}{\partial z} &= \frac{i}{2k} \nabla_T \mathcal{E} + ik_0 \frac{\Delta n^2(\vec{r})}{2n_h} \mathcal{E} + \frac{\partial^2 \mathcal{E}}{\partial z^2} \\ \text{Error} &= \frac{\frac{\partial^2 \mathcal{E}}{\partial z^2}}{\frac{i}{2k} \nabla_T \mathcal{E} + ik_0 \frac{\Delta n^2(\vec{r})}{2n_h} \mathcal{E}} \end{aligned} \quad (\text{A.24})$$

The associated error of the paraxial approximation by dropping the carrier wave can then be numerically evaluated for each slab j in the sphere to:

$$\frac{\frac{\mathcal{E}_{j+1} + \mathcal{E}_{j-1} - 2\mathcal{E}_j}{z_j^2}}{\left[\frac{i}{2k} \nabla_T \mathcal{E} + ik_0 \frac{\Delta n^2(\vec{r})}{2n_h} \mathcal{E} + \frac{\mathcal{E}_{j+1} - \mathcal{E}_{j-1}}{2z_j} \right]} \quad (\text{A.25})$$

$z_j =$ propagation distance to j^{th} slab

The error can be numerically¹⁷ evaluated for each sphere slab, for the two approximation contained within the paraxial approximation: small angles and low refractive index difference (hence no backreflections). In the following figure A.6 two different refractive index differences and the associated error from the paraxial approximation are compared. The error in the second slab increases with increasing Δn , here the paraxial approximation starts to fail. For the spheres in our experiment a maximum refractive index difference of 0.09 was used, therefore we are well within the paraxial regime with negligible error.

¹⁷ $\nabla_T \mathcal{E} = \text{IFFT}(\text{FFT}(\mathcal{E}) * k^2)$

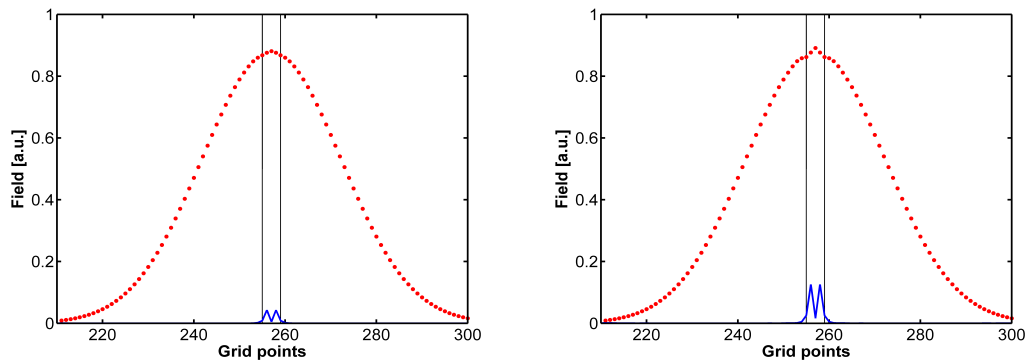


Figure A.6: Evaluation of the error for the same simulation parameters described in figure A.5(right). Both plots show the absolute field in the propagation direction (red) the error (blue) and the size of the second sphere slab for which the error is evaluated. In the left picture $\Delta n = 0.09$ with an relative error of 5.3% and the right picture shows the error and field for $\Delta n = 0.18$ with an relative error of 13.6%.

A.5.3 Two sphere array

At this point I continue with the case of two spheres ($N = 2$) to illustrate the full numerical approach. By virtue of the symmetry of the applied laser fields we assume the spheres are symmetrically placed around $z = D_f/2$ with a separation D , and label the sphere at $z = (D_f - D)/2$ as sphere 1, and that at $z = (D_f + D)/2$ as sphere 2. Then for a given sphere separation D we calculate the counter-propagating fields between $z = [0, D_f]$ using the beam propagation method and from the fields we numerically calculate the force $F_1 = -F_2$ for each sphere, where $F_1 = F_{CP1} - F_{CP2}$. By calculating the CP fields for a variety of sphere separations we can numerically find the sphere separations where the force on each sphere is zero. By plotting the force $F_2(D)$ acting on the sphere at $z = (D_f + D)/2$ versus sphere separation D we can determine the stability of the solution, stable equilibria having a negative slope $\partial F_2/\partial D < 0$, indicating a restoring force. From the calculated forces we may also numerically determine the effective potential for the sphere motion

$$U(D) = - \int^D \delta z F_2(D) \quad (\text{A.26})$$

An example of the force calculation is shown in figure A.7(left) for a wavelength of $\lambda = 1070nm$ and parameters values $n_h = 1.32$, $\Delta n = (n_s - n_h) = 0.09$, $r_{sphere} = 1.5\mu m$ and $D_f = 90\mu m$. For the parameter values chosen the system is observed to have more then one stable equilibrium separation for

the two spheres, namely the solutions marked 1) for $D \approx 6\mu\text{m}$, and 3) for $D \approx 18\mu\text{m}$. The equilibrium solution 2) for $D \approx 11\mu\text{m}$ is by virtue of the positive slope of the force curve unstable. On the right hand side the effective calculated potential for the same parameters is shown, the analogous numbers indicate the approximate position of the equilibrium separations within the potential to aid the eye.

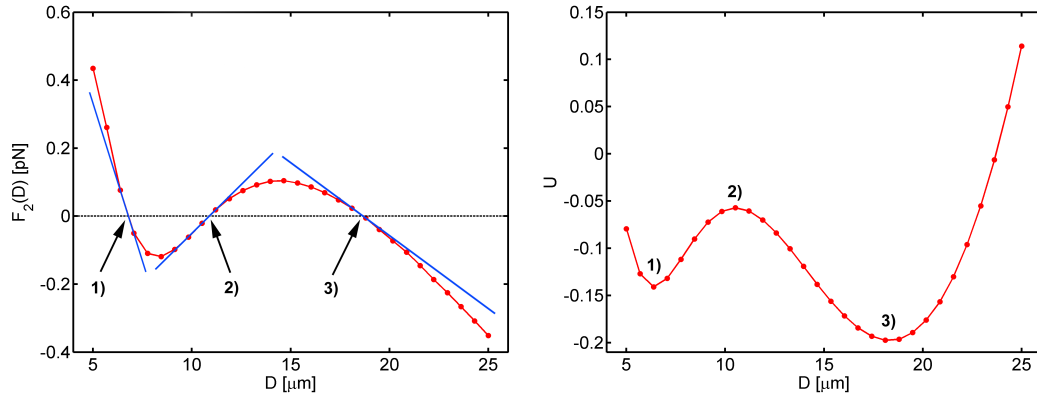


Figure A.7: Left: Plot of the computed force $F_2(D)$ acting on sphere 2 versus sphere separation D . Equilibrium separations of the two spheres are found when the force is zero. Depending on the sign of the slope (represented by blue lines) through the equilibria they are either stable (negative slope) or unstable (positive slope). Right: Calculated effective potential of the system. The numbers correspond to the stable (1,3) and unstable (2) solutions in both pictures.

A.6 Conclusion

In this chapter I have given a description of the theoretical model used to simulate optical binding, the results from this numerical theory are used throughout my thesis and compared to experimental findings.

I gave a brief overview of several methods used to simulate optical tweezers and to the choice of applying the paraxial approximation to model optical binding. The simplest case of one sphere in one beam was used to built upon and describe how to numerically setup an array of two spheres in two counter-propagating fields.

Throughout the description of the model I pointed out the approximations and limitations of this numerical approach. Which governed the experiments conducted, specifically it limited the work present to low refractive index differences and sphere sizes at the order of the optical wavelength of the

fields. Sensitivities in the numerics will be detailed in the experimental section where they are used to qualitatively explain the experimental findings. Two main parts stand out in this chapter, the field propagation and the force calculation from which the equilibrium separation of the spheres was calculated. Additionally the model allows to predict the optical potential landscape for the two sphere system.

A previous model [18] gave qualitative agreement with the experimental findings in this thesis, with a new force calculation described in this chapter form [117, 118] a better agreement between experiment and theory could be achieved. Future work on the model would include higher order arrays (with number of spheres $N = 3, 4, 5...$ here the symmetry of the system can only be exploited with three spheres where the centre sphere is located at $D_f/2$. For higher order arrays the numerics are becoming quite computational intensive. For a 4 sphere array an intriguing question is whether the spacings are all equidistant. Also the approximation of a symmetric solution around $D_f/2$ might not capture all theoretical possible stable configurations, here particularly it is of interest to carry out a full simulation, where all spheres are permitted to obtain various positions, this would however involve an extensive amount of calculations.

Optical binding is an intriguing phenomenon and presently not fully understood and has captured the attention of several research groups in the field. Currently there is a comparison between different modeling methods in progress, it involves V. Karasek and P. Zemanek [91] which utilise the coupled dipole method, M. Mazilu developed a code based on the Finite Element Method and P. Jacobsen. Here it is interesting to see how the paraxial approach compares to these more sophisticated methods.

For future modelling one could possibly extend to the paraxial theory to incorporate back reflections by the spheres, by utilising the calculated error as a source and feeding it back into the propagation algorithm.

Bibliography

- [1] Wikipedia, 2007.
<http://en.wikipedia.org>.
- [2] A. Ashkin. Acceleration and trapping of particles by radiation pressure. *Physical Review Letters*, 24:156, 1970.
- [3] M.J. Lang and S.M Block. Resource letter: Lbot-1: Laser-based optical tweezers. *Am. J. Phys.*, 71:201, 2002.
- [4] D.G. Grier. A revolution in optical manipulation. *Nature*, 424:810, 2003.
- [5] K.T. McDonald. Laser tweezers. *Am. J. Phys.*, 68:486, 2000.
- [6] N. Malagnino, G. Pesce, A. Sasso, and E. Arimondo. Measurements of trapping efficiency and stiffness in optical tweezers. *Opt. Communications*, 15:214, 2002.
- [7] S. Cran-McGreehin, T.F. Krauss, and K. Dholakia. Monolithic integration of microfluidic channels and semiconductor lasers. *Lab Chip*, 6:1122, 2006.
- [8] A. Constbale, J. Kim, J. Mervis, F. Zarinetchi, and M. Prentiss. Demonstration of a fiber-optical light-force trap. *Opt. Lett.*, 18:1867, 1993.
- [9] J. Guck, S. Schinkinger, B. Lincoln, F. Wottawah, S. Ebert, M. Romeyke, D. Lenz, H.M. Erickson, R. Ananthakrishnan, D. Mitchell, J. Kaes, S. Ulvick, and C. Bilby. Optical deformability as an inherent cell marker for testing malignant transformation and metastatic competence. *J. Opt. Soc Am. B*, 20-7:1568, July 2003.

- [10] P.R.T. Jess, V. Garces-Chavez, D. Smith, M. Mazilu, L. Paterson, A. Riches, C.S. Herrington, W. Sibbett, and K. Dholakia. Dual beam fiber trap for raman micro-spectroscopy of single cells. *Opt. Express*, 14:5779, 2006.
- [11] W. Singer, M. Frick, S. Bernet, and M. Ritsch-Marte. Self-organized array of regularly spaced microbeads in a fiber-optical trap. *J. Opt. Soc Am. B*, 20-7:1568, July 2003.
- [12] M.M. Burns, J.-M. Fournier, and J.A. Golovchenko. Optical binding. *Phys. Rev. Lett.*, 63:1233, 1989.
- [13] F. Depasse and J.M. Vigoureux. Optical binding force between two rayleigh particles. *J. Phys. D: Appl. Phys.*, 27:914, 1994.
- [14] P.C. Chaumet and M. Nieto-Vesperinas. Optical binding of particles with or without the presence of a flat dielectric surface. *Phys. Rev. B*, 64:035422 1, 2001.
- [15] S.K. Mohanty, J.T. Andrews, and P.K. Gupta. Optical binding between dielectric particles. *Optics Express*, 12:2749, 2004.
- [16] M.M. Burns, J.-M. Fournier, and J.A. Golovchenko. Optical matter: Crystalization and binding in intense optical fields. *Science*, 749:750, 1990.
- [17] S.A. Tatarkova, A.E. Carruthers, and K. Dholakia. One-dimensional optically bound arrays of microscopic particles. *Phys. Rev. Lett.*, 89:283901, 2002.
- [18] D. McGloin, A.E. Carruthers, K. Dholakia, and E.M. Wright. Optically bound microscopic particles in one dimension. *Phys. Rev. E*, 69:021403-1, 2004.
- [19] M. Guillon. Field enhancement in a chain of optically bound dipoles. *Optics Express*, 14:3045, 2006.
- [20] M. Guillon and O. Moine and B. Stout. Longitudinal optical binding of high optical contrast microdroplets in air. *Phys. Rev. Lett.*, 96:143902, 2006.

-
- [21] M.D. Summers, J.P. Reid, and D. McGloin. Optical guiding of aerosol droplets. *Opt. Express*, 14:6373, 2006.
- [22] V. Garces-Chavez, D. Roskey, M.D. Summers, H. Melville, D. McGloin, E.M. Wright, and K. Dholakia. Optical levitation in a bessel light beam. *Appl. Phys. Lett.*, 85:4001, 2004.
- [23] K. Visscher, S.P. Gross, and S.M. Block. Construction of multiple-beam optical traps with nanometer-resolution position sensing. *IEEE J. Sel Top. Quantum Electron.*, 2:1066, 1996.
- [24] E.R. Dufresne, G.C. Spalding, M.T. Dearing, S.A. Sheets, and D.G. Grier. Computer-generated holographic optical tweezer arrays. *Rev. Sci. Instrum.*, 72:1810, 2001.
- [25] R.L. Eriksen, P.C. Mogensen, and J. Glueckstad. Multi-beam optical tweezers generated by the generalized phase-contrast method. *Opt. Lett.*, 27:267, 2002.
- [26] M.P. McDonald, L. Paterson, K. Volke-Sepulveda, J. Arlt, W Sibbett, and K. Dholakia. Creation and manipulation of three-dimensional optically trapped structures. *Science*, 296:1101, 2002.
- [27] M.P. McDonald, G.C. Spalding, and K. Dholakia. Microfluidic sorting in an optical lattice. *Nature*, 426:421, 2003.
- [28] V. Garces-Chavez, G.C. Spalding, and K. Dholakia. Extended-area optically induced organization of microparticles on a surface. *Appl. Phys. Lett.*, 86:031106, 2005.
- [29] Y. Roichman, B. Sun, Y. Roichman, J. Amto-Grill, and D. Grier. Optical forces arising from phase gradients. *arXiv.org.>cond-mat>arXiv:cond-mat/0703543*, website, 2007.
- [30] T. Cizmar, V. Garces-Chavez, K. Dholakia, and P. Zemanek. Optical conveyor belt for delivery of submicron objects. *Appl. Phys. Lett.*, 86:174101, 2005.
- [31] W.M. Lee, V. Garces-Chavez, and K. Dholakia. Interference from multiple trapped colloids in an optical vortex beam. *Opt. Express*, 14:7436, 2006.

- [32] J.-M. Fournier, J. Rohner, P. Jacquot, R. Johann, S. Mieas, and R.-P. Salathe. Assembling mesoscopic particles by various optical schemes. In *Optical Trapping and Micromanipulation 2: Proceedings of SPIE*, volume 5930, pages 59300Y–1, 2005.
- [33] G. Roosen and C. Imbert. Optical levitation by means of two horizontal laser beams: A theoretical and experimental study. *Phys. Lett.*, 59A:6, 1976.
- [34] G. Roosen. A theoretical and experimental study of the stable equilibrium positions of spheres levitated by two horizontal laser beams. *Opt. Communications*, 21:189, 1977.
- [35] P.W. Milonni and J.H. Eberly. *Lasers*. John Wiley Sons, 1988.
- [36] A. Dunn. *Light Scattering Properties of Cells*. PhD thesis, Biomedical Engineering University of Texas at Austin, 1997.
- [37] X. Ma, J.Q. Lu, R.S. Brock, K.M. Jacobs, P. Yang, and X.H. Hu. Determination of complex refractive index of polystyrene microspheres from 370 to 1610 nm. *Phys. Med. Biol.*, 48:4165, 2003.
- [38] G.C. Spalding, 2005. privat communication.
- [39] F. Garcia-Santamaria, H. Miguez, M. Ibisate, F. Meseguer, and C. Lopez. Refractive index properties of calcined silica submicron spheres. *Langmuir*, 18:1942, 2002.
- [40] Quanzhou zhongyou op. inst., 2005.
<http://wilgin.ebigchina.com/sdp/149202/4/cp-942408>.
- [41] F. Bates, F.P. Phelps, and C.F. Snyder. *Saccharimetry, the properties of commercial sugars and their solutions*. Internatinal Critical Tables, unknown.
- [42] The International Association for the Properties of Water and Steam. Release on the refractive index of ordinary water substance as a function of wavelength, temperature and pressure, 1997. www.iapws.org.
- [43] Bernold Richerzhagen. Interferometer for measuring the absolute refractive index of liquid water as a function of temperature at 1.064micron. *Appl. Opt.*, 35-10:1650, 1996.

-
- [44] P. Schiebner, J. Straub, J.M.H. Levelt-Sengers, and J.S. Gallagher. Refractive index of water and stem as function of wavelength, temperature and density. *J. Phys. Chem. Ref. Data*, 19:677, 1990.
- [45] J.D. Stranathan. *The particles of modern physics*. Blakiston Co., 1942. Table 729 in Smithsonian Physical Tables.
- [46] R.A. Flynn, B. Shao, M. Chachisvilis, M. Ozkan, and S.C. Esener. Counter-propagating optical trapping system for size and refractive index measurements of microparticles. *Biosensors and Bioelectronics*, 21:1029, 2004.
- [47] E.R. Dufresne and D.G. Grier. Optical tweezer arrays and optical substrates created with diffractive optics. *Rev. Sci. Instrum.*, 69:1974, 1998.
- [48] E.R. Lyons and G.J. Sonek. Confinement and bistability in a tapered hemispherically lensed optical fiber trap. *Appl. Phys. Lett.*, 66:1584, 1995.
- [49] J.W. Goodman. *Introduction to Fourier Optics*. McGraw-Hill Singapore, 1996.
- [50] L.I. Mc Canna, M. Dykman, and B. Golding. Thermally activated transitions in a bistable three-dimensional optical trap. *Nature*, 402:785, 1999.
- [51] H. Little, C.T.A. Brown, V. Garces-Chavez, W. Sibbett, and K. Dholakia. Optical guiding of microscopic particles in femtosecond and continuous wave bessel light beams. *Opt. Express*, 12:2560, 2004.
- [52] K. Dholakia, H. Little, C.T.A. Brown, B. Agate, D. McGloin, and W. Sibbett. Imaging in optical micromanipulation using two-photon excitation. *New J. Phys.*, 6:136, 2004.
- [53] J. Liu, H. Schroeder, S.L. Chin, R. Li, and Z. Xu. Nonlinear propagation of fs laser pulses in liquids and evolution of supercontinuum generation. *Opt. Express*, 13:10248–10259, 2005.
- [54] B. Agate, C.T.A. Brown, W. Sibbett, and K. Dholakia. Femtosecond optical tweezers for in-situ control of two-photon fluorescence. *Opt. Express*, 12:3011–3017, 2004.

- [55] G.P. Agrawal. *Nonlinear Fiber Optics*. Academic Press, London, UK, 1995.
- [56] W.J. Tomlinson, R.H. Stolen, and C. V. Shank. Compression of optical pulses chirped by self-phase modulation in fibers. *J. Opt. Soc. Am. B*, 1:139–149, 1984.
- [57] J.B. Kelman, D.A. Greenhalgh, E. Ramsay, D. Xiao, and D.T. Reid. Flow imaging by use of femtosecond-laser induced two-photon fluorescence. *Opt. Lett.*, 29:1873–1875, 2004.
- [58] W. Kaiser and C.G.B. Garret. Two-photon excitation in $\text{CaF}_2:\text{Eu}^{2+}$. *Phys. Rev. Lett.*, 7:229–331, 1961.
- [59] A. Fischer, C. Cremer, and E.H.K. Stelzer. Fluorescence of coumarins and xanthenes after two-photon absorption with a pulsed titan-sapphire laser. *Appl. Opt.*, 7:1989–2003, 1995.
- [60] P. Domachuk, M. Cronin-Golomb, B. Eggleton, S. Mutzenich, G. Rosengarten, and A. Mitchell. Application of optical trapping to beam manipulation in optofluidics. *Opt. Express*, 13:7265–7275, 2005.
- [61] N.K. Metzger, E.M. Wright, and K. Dholakia. Theory and simulation of the bistable behavior of optically bound particles in the mie size regime. *New J. Phys.*, 8:139, 2006.
- [62] B.C. Kuo. *Automatic Control Systems*. Prentice-Hall, 1987.
- [63] J.C. Meiners and S.R. Quake. Direct measurement of hydrodynamic cross correlations between two particles in an external potential. *Phys. Rev. Lett.*, 82:2211, 1999.
- [64] P. Bartlett, S.I. Henderson, and S.J. Mitchell. Measurement of the hydrodynamic forces between two polymer-coated spheres. *Phil. Trans. R. Soc. Lond.*, 359:883, 2001.
- [65] M. Polin, D.G. Grier, and S.R. Quake. Anomalous vibrational dispersion in holographically trapped colloidal arrays. *Phys. Rev. Lett.*, 96:088101, 2006.
- [66] B. Lincoln. *The Microfluidic Optical Stretcher*. PhD thesis, Der Fakultät fuer Physik und Geowissenschaften der Universitaet Leipzig, 2006.

-
- [67] M. Polin, K. Ladavac, S. Lee, Y. Roichmann, and D.G. Grier. Optimized holographic optical traps. *Opt. Express*, 13:5831, 2005.
- [68] M. Born and E. Wolf. *Principles of Optics*. Cambridge University Press, UK, 2003. pp 759-789.
- [69] J.C. Crocker and D.G. Grier. Methods of digital video microscopy for colloidal studies. *J. Colloid. Interface Sci.*, 14:3677, 1996.
- [70] H. Risken. *The Fokker-Planck Equation*. Springer-Verlag, Berlin, 1989. 2nd ed.
- [71] A. Pralle, E.L. Florin, E.H.K. Stelzer, and J.K.H. Hoerber. Local viscosity probed by photonic force microscopy. *Appl. Phys. A*, 66:71, 1997.
- [72] E.L. Florin, A. Pralle, E.H.K. Stelzer, and J.K.H. Hoerber. Photonic force microscope calibration by thermal noise analysis. *Appl. Phys. A*, 66:75, 1997.
- [73] K.C. Neuman and S.M. Block. Optical trapping. *Rev. Sci. Instrum.*, 75:2787, 2004.
- [74] A.R. Clapp, A.G. Ruta, and R.B. Dickinson. Three-dimensional optical trapping and evanescent wave light scattering for direct measurement of long range forces between a colloidal particle and a surface. *Rev. Sci. Instrum.*, 70:2627, 1999.
- [75] R. Bar-Ziv, A. Meller, T. Tlusty, E. Moses, J. Stavans, and S.A. Safran. Localized dynamic light scattering: Probing single particle dynamics at the nanoscale. *Phys. Rev. Lett.*, 78:154, 1997.
- [76] Roberto Gilli, 1997.
<http://www.seas.upenn.edu/courses/belab/be309/SucroseCalculator.html>.
- [77] M. Mathlouthi and J. Genotelle. *SUCROSE Properties and Applications*. Blackie Academic and Professional, 1995.
- [78] C.D. Hodgman, R.C. Weast, and S.M. Selby. *Handbook of Chemistry and Physics*. Chemical Rubber Publishing Co., 1959.

- [79] Universitaet Graz, 2007.
<http://physchem.kfunigraz.ac.at/sm/Service/Water/D2Ovisc.htm>.
- [80] E.J.G. Peterman, F. Gittes, and C. Schmidt. Laser-induced heating in optical traps. *Biophys. J.*, 84:1308, 2003.
- [81] P. Nakroshis, M. Amoroson, J. Legere, and C. Smith. Measuring boltzmann's constant using video microsopy. *Am. J. Phys.*, 71:568, 2003.
- [82] J.S. Park, C.K. Choi, and K.D. Kihm. Temperature measurement for a nanoparticle suspension by detecting the brownian motion using optical serial sectioning microscopy (ossm). *Meas. Sci. Technol.*, 16:1418, 2005.
- [83] Eric Weeks, 2006.
<http://www.physics.emory.edu/weeks/lab/interface.html>.
- [84] T.G. Mason and D.A. Weitz. Optical measurements of frequency-dependent linear viscoelastic moduli of complex fluids. *Phys. Rev. Lett.*, 74:1250, 1995.
- [85] UCCS Refractive index website, 1996.
<http://web.uccs.edu/bgaddis/chem337/expts/nD/nD.htm>.
- [86] Y. Liu, G.J. Sonek, M.W. Berns, and B.J. Tromberg. Physiological monitoring of optically trapped cells. *Biophys. J.*, 71:2158, 1996.
- [87] D.C. Appleyard, K.Y. Vandermeulen, H. Lee, and M.J. Lang. Optical trapping for undergraduates. *Am. J. Phys.*, 75:5, 2007.
- [88] K. Berg-Sorensen and H. Flyvbjerg. Power spectrum analysis for optical tweezers. *Rev. Sci. Inst.*, 75:594, 2004.
- [89] M. Wei, K. Yang, A. Katmenyan, and A. Chiou. Three-dimensional optical force field on a chinese hamster ovary cell in a fiber-optical dual-beam trap. *Opt. Express*, 14:3056, 2006.
- [90] A. Jonas, P. Zemanek, and E.L. Florin. Single-beam trapping in front of reflective surface. *Optics Letters*, 26:1466, 2001.
- [91] V. Karasek, K. Dholakia, and P. Zemanek. Analysis of optical binding in one dimension. *Appl. Phys. B*, 84:149, 2006.

- [92] R.P Feynman, 1959. Talk at the annual meeting of the American Physical Society.
- [93] A.Ashkin, J.M. Dziedzic, J.E. Bjorkholm, and S. Chu. Observation of a single-beam gradient force optical trap for dielectric particles. *Opt. Lett.*, 11:288, 1986.
- [94] K. Ladavac and D. Grier. Microoptomechanical pump assembled and driven by holographic optical vortex arrays. *Opt. Express*, 12:1144, 2004.
- [95] J. Leach, H. Mushfique, R. di Leonardo, and M. Padgett. An optically driven pump for microfluidics. *Lab on a Chip*, 6:735, 2006.
- [96] A. Terray, J. Oakey, and D.W.M. Marr. Microfluidic control using colloidal devices. *Science*, 296:1841, 2002.
- [97] P.J. Rodrigo, R.L. Eriksen, V.R. Daria, and J. Glueckstad. Interactive light-driven and parallel manipulation of inhomogeneous particles. *Lab on a Chip*, 6:735, 2006.
- [98] M.E.J. Friese, H. Rubinsztein-Dunlop, P. Hagberg J. Gold, and D. Hanstrop. Optically driven micromachine elements. *Appl. Phys. Lett.*, 78:547, 2001.
- [99] S. Neale, M. MacDonald, K. Dholakia, and T. Krauss. All-optical control of microfluidic components using form birefringence. *Nat. Mater.*, 4:533, 2003.
- [100] S.L. Neale. *Optically controlled microfluidics*. PhD thesis, University of St Andrews School of Physics and Astronomy, 2006.
- [101] S. Maruo, K. Ikuta, and H. Korogi. Optically driven micromanipulation tools fabricated by two-photon microstereolithography. *J. Microelectromech. Syst.*, 12:533, 2003.
- [102] L. Kelemen, S. Valkai, and P. Ormos. Integrated optical motor. *Appl. Opt.*, 45:2777, 2006.
- [103] R.C. Gauthier, R.N. Tait, and M. Ubriaco. Activation of microcomponents with light for microelectro-mechanical systems and micro-optical-electro-mechanical systems applications. *Appl. Opt.*, 41:2361, 2002.

- [104] P. Galajda and P. Ormos. Complex micromachines produced and driven by light. *Appl. Phys. Lett.*, 78:249, 2001.
- [105] R.C. Gauthier. Theoretical model for an improved radiation pressure micromotor. *Appl. Phys. Lett.*, 67:2269, 1995.
- [106] R.C. Gauthier and M. Ashman. Simulated dynamic behavior of single and multiple spheres in the trap region of focused laser beams. *Appl. Opt.*, 37:6421, 1998.
- [107] R.C. Gauthier, R.N. Tait, and M. Ubriaco. Activation of microcomponents with light for microelectro-mechanical systems and micro-optical-electro-mechanical systems applications. *Appl. Opt.*, 4:2361, 2002.
- [108] J. Liu, H. Schroeder, S.L. Chin, R. Li, and Z. Xu. Nonlinear propagation of fs laser pulses in liquids and evolution of supercontinuum generation. *Opt. Express*, 13:10248, 2005.
- [109] P.C. Waterman. Symmetry, unitarity and geometry in electromagnetic scattering. *Phys. Rev. D*, 3:825, 1971.
- [110] T.A. Nieminen. Comment: Geometric absorption of electromagnetic angular momentum. *Opt. Commun.*, 235:227, 2004.
- [111] T.A. Nieminen, S.J. Simon, N.R. Heckenberg, and H. Rubinsztein-Dunlop. Optical torque and symmetry. In *SPIE*, volume 5514, page 254, 2004.
- [112] P.C. Chaumet and C. Billaudeau. Coupled dipole method to compute optical torque: Application to a micropropeller. *J. of Appl. Phys.*, 101:023106, 2007.
- [113] J.D. Jackson. *Classical Electrodynamics*. John Wiley and Sons, Inc., 1999. pp 261.
- [114] J. Stratton. *Electromagnetic Theory*. Mc-Graw Hill, 1941.
- [115] J.A. Kong. *Electromagnetic Wave Theory*. EMW, 2005.
- [116] P.C. Chaumet and M. Nieto-Vesperinas. Coupled dipole method determination of the electromagnetic force on a particle over a flat dielectric substrate. *Phys. Rev. B*, 61:14119, 2000.

-
- [117] M. Mansuripur. Radiation pressure and the linear momentum of the electromagnetic field. *Opt. Express*, 12:5375, 2004.
- [118] A.R. Zakharian, M. Mansuripur, and J. V. Moloney. Radiation pressure and the distribution of electromagnetic force in dielectric media. *Opt. Express*, 13/7:2321, 2005.
- [119] B.A. Kemp, T.M. Grzegorzczuk, and J.A. Kong. Ab initio study of the radiation pressure on dielectric and magnetic media. *Opt. Express*, 13:9280, 2005.
- [120] A. Ashkin. Forces of a single-beam gradient trap on a dielectric sphere in the ray optics regime. *Biophys. J.*, 61:569, 1992.
- [121] A. Mazolli, P.A. Maia Neto, and H.M. Nussenzveig. Theory of trapping forces in optical tweezers. *Proc. R. Soc. Lond. A*, 459:3021, 2003.
- [122] J.P. Gordon. Radiation forces and momenta in dielectric media. *Phys. Rev. A*, 8:14, 1973.
- [123] Y. Harada and T. Asakura. Radiation forces on a dielectric sphere in the rayleigh scattering regime. *Opt. Commun.*, 124:529, 1996.
- [124] P. Zemanek, A. Jonas, L. Sramek, and M. Liska. Optical trapping of rayleigh particles using a gaussian standing wave. *Opt. Commun.*, 151:273, 1998.
- [125] V. A. Markel. Divergence of dipole sums and the nature of non-lorentzian exponentially narrow resonances in one-dimensional periodic arrays of nanospheres. *J. Phys. B.*, 38:115, 2005.
- [126] E.M. Purcell and C.R. Pennypacker. Scattering and absorption of light by nonspherical dielectric grains. *Astrophys. J.*, 186:705, 1973.
- [127] B.T. Draine and P.J. Flatau. The discrete-dipole approximation for scattering calculations. *J. Opt. Soc. Am. A*, 11:1491, 1994.
- [128] T. Thusty, A. Meller, and R. Bar-Ziv. Optical gradient forces of strongly localized fields. *Phys. Rev. Lett.*, 81:1738, 1998.

- [129] A. Rohrbach. Stiffness of optical traps: Quantitative agreement between experiment and electromagnetic theory. *Phys. Rev. Lett.*, 95:168102, 2005.
- [130] N.B. Viana, M.S. Rocha, O.N. Mesquita, A. Mazolli, P.A. Maia Neto, and H.M. Nussenzveig. Towards absolute calibration of optical tweezers. *Phys. Rev. E*, 75:021914, 2007.
- [131] T.A. Nieminen, H. Rubinsztein-Dunlop, N.R. Heckenberg, and A.I. Bishop. Numerical modelling of optical trapping. *Opt. Express*, 13/7:2321, 2005.
- [132] S. Bayoudh, T.A. Nieminen, N.R. Heckenberg, and H. Rubinsztein-Dunlop. Orientation of biological cells using plane-polarized gaussian beam optical tweezers. *Journal of Modern Optics*, 50:1581, 2003.
- [133] M. Neviere B. Stout and E. Popov. T matrix of the homogeneous anisotropic sphere: applications to orientation-averaged resonant scattering. *J. Opt. Soc. Am. A.*, 24:1120, 2007.
- [134] D.A. White. Vector finite element modeling of optical tweezers. *Computer Physics Communications*, 128:558, 2000.
- [135] M.D. Feit and J.A. Fleck. Computation of mode properties in optical fiber waveguides by propagation beam method. *Appl. Opt.*, 19:1154, 1980.
- [136] A.E. Siegman. *Lasers*. University Science Books, 1986.
- [137] T.-C. Poon and T. Kim. *Engineering Optics with Matlab*. World Scientific Publishing, 2006.
- [138] J. Arlt. *Applicationns of Laguerre-Gaussian beams and Bessel beams to both nonlinear and atom optics*. PhD thesis, University of St Andrews, School of Physics and Astronomy, 1999.
- [139] E.A. Sziklas and A.E. Siegman. Mode calculations in unstable resonators with flowing saturable gain. 2: Fast fourier transform method. *Appl. Opt.*, 14:1874, 1975.